SYNTHESIS OF METAL MODIFIED MESOPOROUS ZEOLITES CATALYSTS: APPLICATION IN CONVERSION OF OLEFINS TO VALUABLE LIQUID PRODUCTS

LONDIWE YVONNE MTHETHWA

STUDENT NUMBER: 3474672

Dissertation submitted in fulfilment of the requirement for the degree of Master of Science in Chemistry at the University of the Western Cape

Cape Town

2016

Declaration

ORIGINAL WORK

I, Londiwe Yvonne Mthethwa, hereby declare that this study represents original, unaided work that was done by the author under the supervision of Professor M. Masikana. It has not been submitted in any form for any degree or diploma to another tertiary institution. The research described in this dissertation was carried out in the SAIMAC Department, School of Chemistry, Faculty of Natural Science, University of the Western Cape, from February 2014 to December 2015 for a Degree of Master of Science.

References

The use of work by others has been duly acknowledged and referenced in the text. I understand that copywriting or plagiarism could lead to my degree being disqualified.

Declaration 1 – plagiarism

I Londiwe Yvonne Mthethwa., declare that

1. The research reported in this thesis, except where otherwise indicated is my original research.

2. This thesis has not been submitted for any degree or examination at any other university.

3. This thesis does not contain other persons' data, pictures, graphs or other information, unless specifically acknowledged as being sourced from other persons.

4. This thesis does not contain other persons' writing, unless specifically acknowledged as being sourced from other researchers. Where other written sources have been quoted, then:

    a. Their words have been re-written but the general information attributed to them has been referenced

    b. Where their exact words have been used, then their writing has been placed in italics and inside quotation marks, and referenced.

5. This thesis does not contain text, graphics or tables copied and pasted from the Internet, unless specifically acknowledged, and the source being detailed in the thesis and in the References sections.

Signed ……

Abstract

The effects of temperature, synthesis duration and silica source were studied to obtain suitable conditions for our laboratory experiment concerned with the synthesis of MCM-41 catalyst. The transformation of 1-hexene was studied using modified mesoporous MCM-41as a catalyst. Catalysts were synthesised by co-precipitation and wet impregnation methods doped with aluminium, chromium and iron. Tetraethylorthosilane (TEOS) was used as silica source due to its ability to show improved results than sodium silicate sources. Catalysts were synthesised with single metal doping for the production of Al-MCM-41, Cr-MCM-41 and Fe-MCM-41. Double doped metal catalysts were also synthesised for the production of Cr/Al-MCM-41 and Fe/Al-MCM-41. Catalysts were hydrothermally synthesised at 150 ˚C for 72 h then calcined at 560 ˚C after drying. XRD, SEM, FTIR spectroscopy, BET surface area measurents, ammonia-TPD and NMR spectroscopy were used for characterisation of synthesised materials to understand the structural frame and interior as well as exterior surface.

Synthesised materials were tested for catalytic activity in the oligomerisation of 1-hexene to fuel products and the products were analysed using gas chromatography. Reactions were carried out at atmospheric pressure using a conventional fixed-bed quartz tube reactor at 350 ˚C. High content Silica/Aluminium catalyst showed higher conversion of 1-hexene while selectivity was in favour of C_6 linear isomers. MCM-41 modified with iron and chromium showed well-defined MCM-41 XRD patterns with a reduced intensity of reflections. These catalysts showed activity towards isomerisation reaction selective to linear C_6 isomers with 80% conversion of 1-hexene. Wet impregnation with these metals led to highly reduced crystallinity of MCM-41with dominant hydrocarbon cracking reaction. Al-MCM-41 showed a consistency on the entire samples at a conversion around 80%. Catalyst impregnated with 3% Cr showed a conversion below 10% while 3% Fe impregnated catalyst maintained conversion in the range 75% to 80%.

The double-doped metal samples showed much more reduced surface area and pore volumes compared to the single metal samples and silica MCM-41. These showed a reduced crystallinity and distracted lattice structure of MCM-41. These materials retained about 90% conversion for Cr/Al-MCM-41 and 80% for Fe/Al-MCM-41 as a result of acid sites introduced by aluminium. Isomerisations with combination of cracking and recombination reaction were the dominant reaction for these catalysts.

Acknowledgements

First and foremost, I would like to thank God for the strength and opportunity to do this study. I would like to express my gratitude to the following:

- Prof. Mdleleni and Prof Key for their advice, committed guidance and constructive criticism towards this research project.
- Themba Tshabalala for his time and dedication as well as guidance throughout this project.
- Ebrahim Moihuideen and Anelisa Notini for lending a hand when I needed it.
- PSFIC and SAIAMC department for its funding to pursue this research project
- iThemba labs and Physics department for their technical analysis
- PSFIC analytical lab staff for their analytic help.
- My colleagues for their guidance, co-operation and assistance in the laboratory. Also, to all the students in my research group for their assistance in the laboratory.

Lastly I would like to thank my wonderful, supportive family, especially my sister N.G. Mthethwa who believed in me more than anyone, my late father for his outstanding work of raising the woman I am today, and my brothers L.S. Mthethwa and T.I. Mthethwa. My good friends for providing moral support and prayers T.P. Dladla and put a smile on my face with her wise words when thing became stressful and seem impossible.

Presentation

Londiwe Mthethwa**,** Themba Tshabalala, Masikana Mdleleni, **Synthesis of Al-MCM-41 Zeolites for Conversion of 1-Hexene to Valuable Hydrocarbons** in CATSA catalysis Conference at St George hotel, Pretoria, 9-12 November 2014

Table of Contents

List of tables

Chapter 2

Chapter 3

Chapter 4

Chapter 5

Chapter 6

LIST OF FIGURES

Chapter 1

Chapter 3

Chapter 4

Chapter 5

Chapter 6

CHAPTER 1: Introduction

1. 1 Motivation and aims of this work

Petrochemical refining industries produce a variety of raw materials consisting of short-chain olefins, which are produced from petroleum. Their solubility and high octane content makes them desirable gasoline additives. Oligomerisation provides an alternative pathway to convert short-chain hydrocarbons into valuable liquid products. The use of alumina and silica catalysts show a promising method for reduction of organic solvents being used in the reaction medium [1]. Conversion of olefins to distillates (COD) produces special fuels and solvents that are low in aromatic content, and are used as indoor fuels and biodegradable drilling fluids. Because of their environmentally friendly qualities, these products are among the cleanest on the market which reduces the destruction of the ozone layer. The end product and cracking rate depends on the temperature and the catalyst used [2]. The aim of this project is to study conversion of olefins into distillates carbon number range 10 to 18 over different mesoporous MCM-41 zeolite catalysts.

Specific objectives are as follows:

(i) Synthesising different types of MCM-41 for the catalytic conversion of olefin containing feeds to fuel range hydrocarbons.

(ii) Comparing the metal-modified MCM-41 with MCM-41 as catalysts for oligomerisation of olefins.

(iii) Studying the effects of various synthesis parameters such as Si/Al ratio, temperature, time and pH on the structure of MCM-41.

(iv) Characterise and test the catalysts for olefin oligomerisation for increase selectivity to heavy olefins.

1. 2 Background on zeolites

The first natural zeolite was discovered in 1756 by a Swedish mineralogist Cronstedt. In 1845 Schafhautle reported attempts to synthesize silicates under hydrothermal conditions by heating the silicate gel in an autoclave reactor [3,4]. The successfully adopted hydrothermal

synthesis method for zeolites was reported in 1862 by St. Claire Deville. Due to a lack of essential data for identification further studies resulted in Barrer synthesising a zeolite with no natural counterparts by 1945 [3] . Use of soluble reactants in a basic solution resulted in a highly reactive gel. A large pore zeolite X was synthesised in 1949 by Milton by heating a gel at mild temperature [4, 5]. This resulted in use the of this porous material as a catalyst in industries for fluid catalytic cracking of heavy petrochemical distillates [5].

Zeolites are hydrated aluminosilicates built from three-dimensional network of $[SiO_4]^{4-}$ and $[AlO_4]^{5-}$ tetrahedra linked by oxygen atoms (Figure 1.1). These crystalline microporous materials can also be considered as inorganic and their structural formula is based on the crystallographic unit cell:

$$\mathbf{M_{x/n}[(AlO_2)_x(SiO_2)_y].wH_2O} \qquad \mathbf{1}$$

where **M** is an alkali or alkaline earth cation e.g. Na^+, Ca^{2+}, K^+, or H^+, **n** is the valence of the cation, **w** is the number of water molecules per unit cell, while **x** and **y** are the total numbers of tetrahedral atoms per unit cell [5]. Water within the channels allows mobility of cations for ion-exchange at lower temperatures. The zeolite framework structure is composed of the tetrahedral primary building units and secondary building units, which are geometric arrangements of tetrahedra. These secondary building units may be polyhedra such as cubes, hexagonal or cubo-octahedral [6].

The framework type is used to classify the properties of zeolites. Connectivity of tetrahedral atoms defines the size and shape of pore openings, dimensions of channel system, and the arrangement of cages as well as availability of cation sites. Chemical composition, species within the channels and type of post-synthesis modification determine specific properties of the particular zeolite. Pore openings are characterised by size of the ring, determined by tetrahedral atoms in the ring [7].

The pores and channel are the most important property of zeolites that are associated with molecular sieves. Figure 1.1 below show the formation of different pore sizes of zeolites.

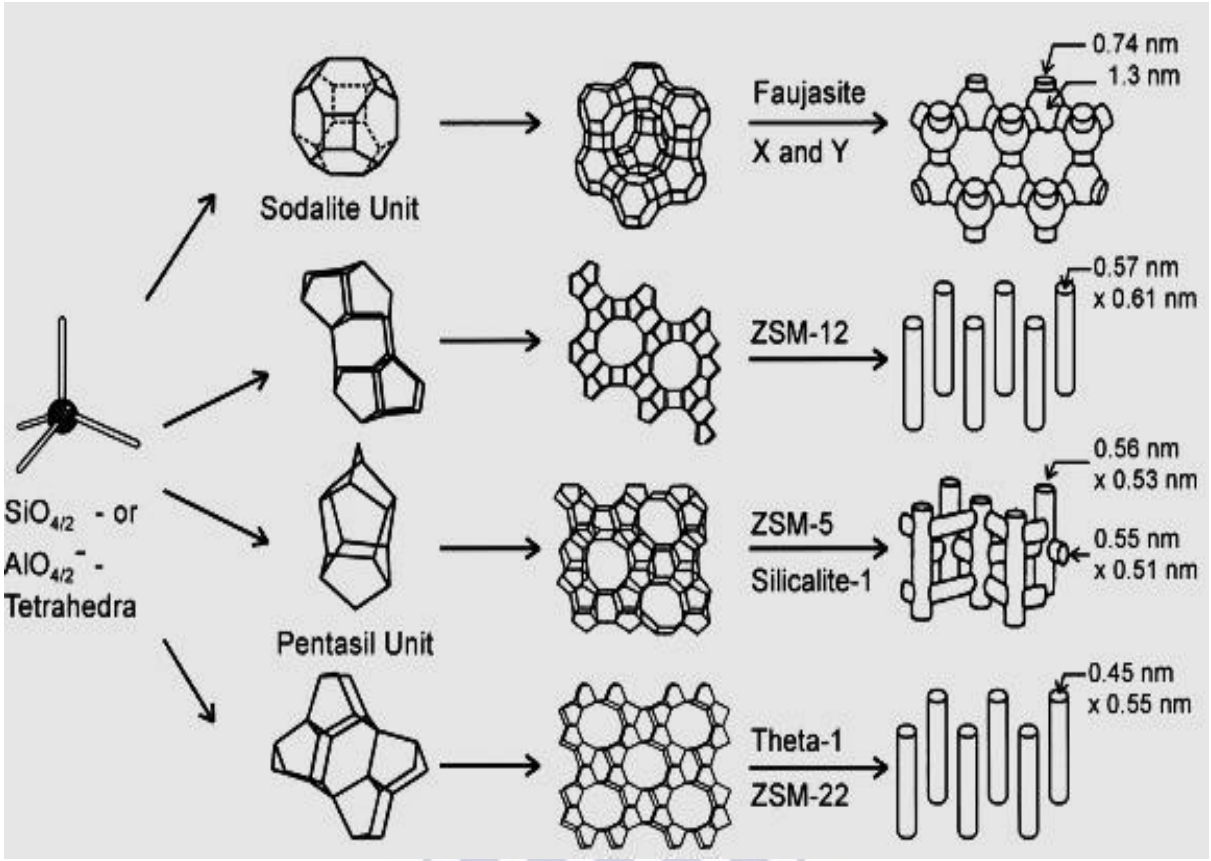

Figure 1. 1: Dimensions and micropore systems on different zeolites [5].

Tetrahedral atoms bridged by oxygen atoms lead to the formation of channels and cavities of specific molecular dimensions. The channels and cavity dimensions are governed by the number of tetrahedra forming the ring. These restrict molecules of certain sizes within intracrystalline pores. Intracrystalline size is determined by the zeolite structure which lies within the range of 0.3 to 1 nm. Secondary building units such as sodalite and pentasil units are composed of 24 tetrahedra linked together, which results in the zeolite structure. Faujasites, e.g. X and Y zeolites, are made up of sodalite units, linked through their hexagonal faces.

A three-dimensional zeolite Y is constituted by spherical cages with 1.3 nm diameter formed by 12 tetrahedral units, therefore zeolite Y is used in fluid catalytic cracking. ZSM-5 zeolite and their silica analogues are built from pentasil units with intersecting systems of ten-membered–ring pores, one being straight and the other sinusoidal [5].

Heterogeneous acid zeolite catalysts used in oil refining have noticeable drawbacks, i.e., the small size of the cavities imposed limitations to intracrystalline diffusion during reactions, hence bulky molecules could not be processed. This led to the focus on the synthesis of mesoporous zeolites to increase the active site accessibility, which could be achieved by post-synthesis routes involving acid or basic chemical treatment and incorporating the hard template in the zeolite structure [8]. Mobil researchers proposed liquid-crystal templating (LCT) mechanism, where in a surfactant liquid crystal structure serves as an organic template. The highly mesoporous MCM-41 from the M41S family was discovered in 1992 by with pore sizes ranging from 2 nm to 10 nm using the surfactants of different chain lengths as templates [1, 9, 10].

Zeolite-like materials of the microporous class have been extensively used in acid-catalysed reactions for the petrochemical and fine chemicals production because of their hydrothermal stability [11]. Structural limitation of microporous resulted to investigation of mesoporous. These materials are reported as highly uniform mesoporous from M41S family namely MCM-41 which has a hexagonal shape, MCM-48 which is cubic and MCM-50 which is a lamellar. Hexagonal MCM-41 has been mostly attractive as a catalyst and a catalyst support because of its properties, including a highly ordered pore system with the pore diameter ranging between 2 and 10 nm, large pore volume, greater hydrocarbon sorption capacities and higher surface area (1000 m^2g^{-1}) as well as thermal stability [12, 13].

These materials are produced from the close-packed silica coated micelles of surfactant template. The use of templates such as alkyltrimethylammonium with varying carbon chain length for the synthesis of MCM-41 enables the alteration of pore size and wall properties [13]. Pure silica MCM-41 contains no Brönsted acid sites; therefore, the substitution of Si with trivalent cations such as Al creates moderate acidic sites [16]. Al substituted Si-MCM-41 has been a success in catalytic cracking, hydrogenation and hydrocracking as well as alkylation and isomerization reaction. These materials have lower acidity than zeolite catalyst such as ZSM-5 and HY. Therefore, their acidity has been increased by increasing the Al content [13, 14].

Due to the lack of acid sites in pure siliceous hexagonal MCM-41, metallosilicate molecular sieves have been used, due to their catalytic activity in selective oxidation reaction [16]. Metal ions such as zinc (Zn), manganese (Mn), Fe, and many more have been incorporated into Al-MCM-41 framework and thermal stability, acid strength and hydrothermal stability increases by introducing zinc in the mesoporous Zn-Al-MCM-41 catalyst [15]. The study of MCM-41 synthesis showed that the addition of promoter oxyanions like bromate, chlorate, sulphate, etc., to the synthesis reaction of zeolites and silica-based microporous materials reduces crystallization time [16].

Al-substituted Si-MCM-41 dealuminates during calcination (removal of surfactant), resulting in the hydrolysis of Al structure due to steam generated in surfactant combustion. High calcination temperatures lead to disruptions in the framework and to the subsequent collapse of pores and channels in the molecular sieve when too much Al is incorporated. Upon substitution with cations, the structures collapse on removal of the template because of their decreased mechanical stability [16]. For the synthesis of this mesoporous material, an organic structure directing agent is used mostly cetyltrimethylammonium bromide. The template gets trapped in the pores during synthesis and needs to be removed to generate the void pores for any application. This can be removed by calcination at higher temperatures (500 -700 °C). Higher temperature may cause partial structural collapse. The template can also be removed by solvent extraction and various modifications. But this requires long extraction time and higher solvent consumption. Sonication-aided modification by use of ultrasound waves has been reported as a possible option for removal of template from mesopores [17].

Figure 1.2 below illustrate the formation of cylindrical pores via two possible mechanistic pathways

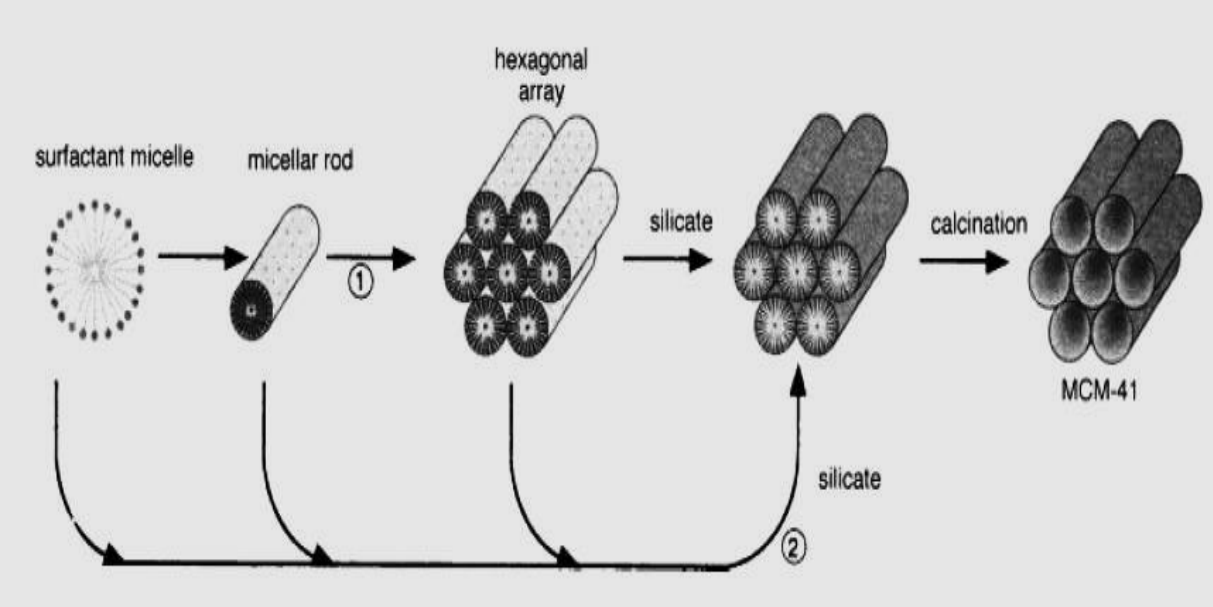

Figure 1. 2: LCT mechanistic pathways for MCM-41 formation [18].

Inorganic anions interact with ammonium head groups of surfactants and form a solid. The newly formed organic-inorganic mesostructure appears as a hexagonal array of micellar rods in silica matrix. Removal of surfactant results in hexagonal mesoporous MCM-41 framework. For the reaction (1) to occur, the surfactant concentration should be enough for the critical micelle concentration (CMC) to form hexagonal framework [19]. The product can be recovered by filtration after the reaction. These mesoporous materials are characterised by high surface area, well-defined pores and high biocompatibility [20].

Surface acidity can be either enhanced by modification of framework, and this can be achieved by incorporation of foreign ions into a silica framework. Strong acid groups which as known as surface grafting can be introduced to the framework[21]. The structural properties that ensure improved catalytic performance are generally determined by the distribution of Al in the silicon molecular sieves (SMS) framework. Brönsted acid sites are distracted by cations attached to Al atoms as well as the Brönsted protons, which are also affected by local geometry of the rings containing Al atoms. Metal-oxygen cluster stabilization requires two proximate Al atoms and it is affected by Al distribution [22].

1. 3 Modified MCM-41

Pure MCM-41 has limited activity as a catalyst. Therefore, its catalytic activity is improved by isomorphous substitution of silicon with metal. Metal-containing catalysts are use as templates for silica synthesis of carbon nanotubes, which show direct correlation between tube diameter and metal nanoparticle size. Transition metals have been used widely in catalyst modification as oxides or metallic forms because of their properties which allow the synthesis of carbon nanotubes. These properties include solubility of carbons; carbon diffusion rate and equilibrium vapor pressure in the metal [23, 24].

Catalyst polymerization activity is improved by depositing homogenous species on the support for an active catalyst. Chromium oxides have been investigated for lower alkene dehydrogenation. Chromium species were used because of their redox and dispersion properties. Cr-containing molecular sieves were found to exhibit high photocatalytic reactivity in ethylene polymerization.

1. 4 Synthesis of zeolites

Zeolites are synthesised by hydrothermal synthesis techniques, which are defined as a reaction that occurs in a closed system at high temperature and high pressure conditions in an aqueous solution [25]. Zeolites are synthesised from a gel of aluminium and silicon sources, an organic template as well as alkaline metal base from room temperature up to 200 °C. Different types of zeolites are produced under these conditions which differ in the nature of starting material, nucleation process and length of reaction time [26].

Zeolites are formed by nucleation and crystal growth reactions which are influenced by parameters such as pH, temperature, reaction time, alkaline cations and template agent. Recent studies showed that the addition of promoter oxyanions in the synthesis of zeolites and silica microporous materials results in reduction of crystallization period [27].

1.4. 1 Alkaline metal base

Zeolites' alkalinity is defined as OH^-/Si ratio or H_2O/Na_2O ratio which determines the crystallinity and nucleation of the catalyst. Higher alkalinity increases Si and Al source solubility while it decreases the polymerization of silicate and aluminate anions. Alkalinity shortens induction and nucleation periods, hence an increased crystallinity of zeolites. Smaller size particles with a narrow distribution are obtained at high alkalinity for pH ranging at 10 to 12 [3].

1.4. 2 Templating reagents

A template is an organic cation which allows the production zeolites with higher Si/Al ratio initiating advances of zeolite production. Tetramethylammonium (TMA) cation provides structure-direction for specific building units in zeolite synthesis. Quaternary ammonium cations are used for composition extension to higher Si/Al ratios and in the synthesis of new siliceous zeolites. Templating occurs in gelation or nucleation stage where it organizes the oxide tetrahedral units into a certain geometric topology, thus providing an initial frame for a particular zeolite structure [3].

For organic molecules to be established as a template, they should have the following characteristics:

- Stable under synthesis conditions and fit in the desired cage.
- Engage in van der Waals interaction with the inner surface and do not complex with the solvent.
- To form clathrasils, molecule must be rigid.
- Formation of clathrasil is favoured by the increase in basicity or polarisability.

Substances used as template must not be degradable at high synthesis temperature and pressure within the autoclave. It should not degrade in highly alkaline conditions which are employed during synthesis via Hofmann elimination. The template should have strong non-bonding interaction with the catalyst framework for non-disrupted framework during the removal [28].

1.4. 3Synthesis temperature and time

Synthesis temperature is a crucial factor for zeolite synthesis as it determines the extent of catalyst crystallisation. Crystallisation temperature also affects the nucleation as well as crystal growth steps, which increases with increase in temperature. Growth rate of zeolite is obtained by

$$0.5\ \Delta l/\ \Delta t \qquad 2$$

Δl is the crystal dimension increase at time Δt accelerated as crystallisation temperature increases. Crystal size and morphology is however not affected by the temperature. The duration of crystallisation is also an important parameter as crystallinity increases with time [25].

1.4. 4Formation of acid sites

Tetrahedral SiO_2 zeolite is an electrically neutral material with no acid sites. Replacement of Si^{4+} by trivalent metal cations such as Al^{3+} creates a pool of negative charges within zeolite pore structure which are compensated by metal cations. Hydrogen bonds to neighboring oxygen atom resulting to hydroxide bridge which is associated with Brönsted acidity of zeolites shown in figure 1.3 below. The concentration of Al affects the acid site distribution on zeolite.

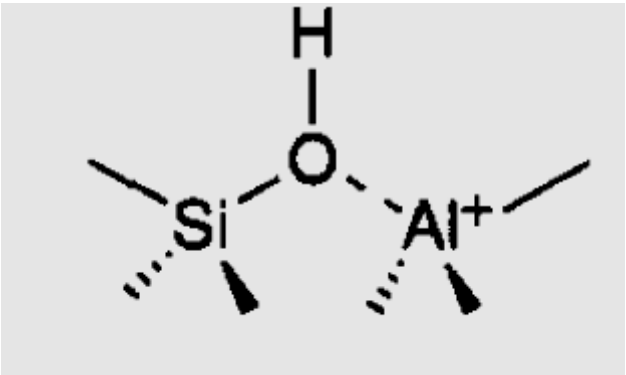

Figure 1. 3: Formation of Brönsted acid sites in zeolite[29].

Due to the presence of Brönsted acid sites a decrease in wavenumber obtained by FTIR technique of bridged OH on the terminal silicon was explained by interaction with Al^{3+} ions. The increase of length of OH bond is also associated with strong acidity of the OH group while an increase in electronegativity around OH influences the electronic density transfers from less to more electronegative. Nearest bond length to donor-acceptor interaction site increases as the interaction strength increases hence increased iconicity. [29].

1.4. 5 Nucleation and crystal growth

Crystal formation from a solution starts with nucleation, where atoms of reactant phase rearrange into a cluster of the product phase with the ability to grow irreversibly to a macroscopically larger size. This is known as primary nucleation, which undergoes further nucleation to form secondary nucleation. The chemical potential between the molecules in the solution known as super-saturation is the driving force for nucleation and crystal growth. The nucleation rate can be determined by the Arrhenius-type equation

$$J = A \exp\left(\frac{-\Delta G*}{kT}\right) \qquad 3$$

The ΔG, the energy required to achieve nucleation, *k* is the Boltzmann constant, T is the absolute temperature ***J*** as a function of super-saturation, ***A*** depending on super-saturation. The nucleation rate is zero until the super-saturation critical value is reached. Surface free energy, σ, determines the energy required to achieve nucleation with a nucleation radius. Therefore the presence of foreign substances in the solution decreases the surface energy hence decrease ΔG^* and r* at constant super-saturation favoring nucleation. A reduction in surface free energy(σ) results in a decreases critical super-saturation value which favors the heterogeneous nucleation at low super-saturation conditions [30].

The incorporation of atoms to the surface of the crystal results in a size increase known as the crystal growth. This is associated with different processes such as transportation of atoms through solution, movement of atoms to the surface and attachment of atoms to the surface, edges and kinks. Figure 1.4 above shows the crystallisation curve for zeolites synthesis; nucleation rate and evolution of crystallinity are plotted as function of time [19, 30].

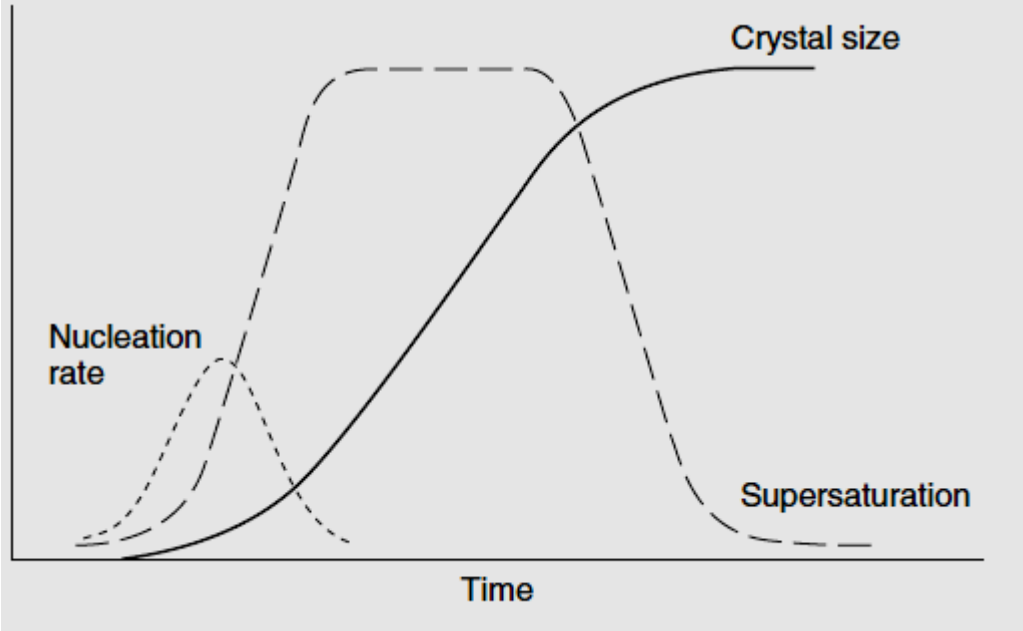

Figure 1. 4: Evolution of nucleation and growth rate during zeolite synthesis [31].

Crystallization of zeolites and zeotype synthesis depends on the parameters such as temperature, stirring, seeding and gel aging. The solution of amorphous reactants with structure forming ions results in a partly reacted heterogeneous mixture referred to as primary amorphous phase. The mixture is allowed to age and heated at a certain temperature which leads to the formation of secondary amorphous phase. After this period, known as the induction period nucleation takes place and the growing zeolites from an amorphous solid. The nucleation increases rapidly and then decrease to zero. As nucleation forms the crystal sizes grow as well. At a certain number of nuclei formed crystal growth initiates which increases until it reaches a steady state as nucleation decline to super-saturation [31].

1.4. 6 Effect of template on zeolite crystal growth

As crystal growth is affected by synthesis conditions which determine its topology, the template also plays a role in crystal morphology. It alters the growth rate of crystal surface therefore certain surfaces may grow more rapidly [32, 33]. Previous studies have shown that the use of triethanolamine as a template increased the crystal size of zeolites A and X. Not only did the nature of the template affect the crystal growth, but the concentration as well. When

the concentration of tetrapropylammonium, TPA, was increased in the synthesis of ZSM-5, larger crystals were obtained due to the formation of clathrates. The formation of clathrates speeds up the rate of crystallisation and increases their size [33].

The use of diquat of tetrapropylammonium, di-TPA, as template resulted in crystal growth rate reduction. Further study showed that position of the template determines if it is a growth inhibitor or promoter. So the template can be adsorbed to the surface and promote growth by condensation or it can inhibit growth by hindering surface condensation [19].

1. 5 Applications of zeolites

In catalysis, zeolites are used for a wide range of applications as catalysts, catalyst supports, and molecular sieves. Changing the framework topology of zeolites by modifying their chemical composition has broadened the scope of their applications. Structural modification of these materials allows the tuning of their acidic sites, which are an important feature of heterogeneous catalysts. Discrete pore size and ordered pore diameter have given zeolites unique properties which allow them to be used as molecular sieves. Zeolites have been widely recognised in catalytic processes because of their shape-selectivity through mass transfer or transition state [5]. Figure 1.5 below illustrated the selectivity of the catalyst to the product formed.

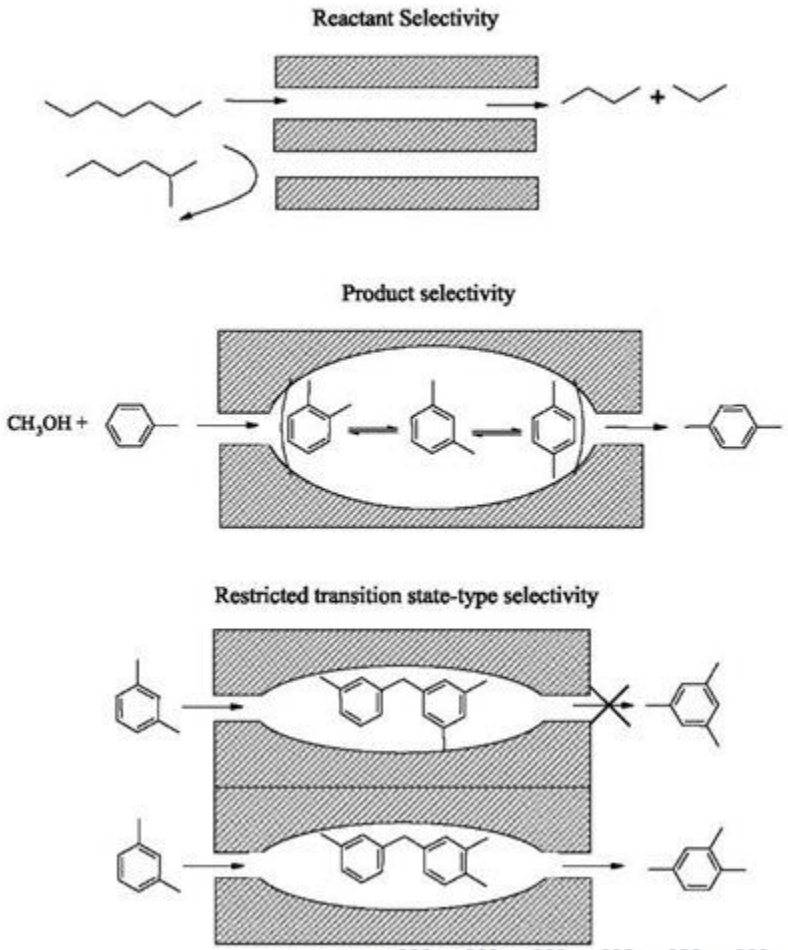

Figure 1. 5: Schematic representation of the three types of shape-selectivity [34].

- *Reactant shape Selectivity* separates reactants in the mixture according to their sizes. Some molecules are restricted by catalyst because their structure cannot diffuse through the catalyst pore size.

- *Product shape Selectivity* occurs when the product formed is bulky to diffuse out of the pore as a product, and will consequently undergo cracking processes to allow passing through or they block the pores and deactivate the catalyst.

- *Restricted Transition-State shape Selectivity* describes the situation where certain reactions are inhibited because their corresponding transition states require more space than extra space than pore cavities [34].

1.5. 1 Ion-exchange

Silicon isomorphous substitution by aluminium creates a negative charge on the framework which can be balanced by framework incorporating inorganic cations such as sodium, potassium and lithium. These are loosely bonded and therefore can be exchanged with other ions in solution. Metal ion mobility allows ion exchange in zeolite cages. Exchange is preferable in aqueous solution as the loosely bound sodium exchange with calcium, reducing the hardness of water. Hence zeolites have found applications in the washing powder industry [19, 28].

Zeolites have been used in drying of gas streams because of their high affinity for water. Clinoptilolite zeolite is used in the water industry for sewage and agricultural effluents treatment because of its selectivity to ammonium ion exchange. Municipal water supplies are processed through zeolites to reduce ammonium concentration as well as metallic cations [28].

1.5. 2 Catalytic applications of zeolites

In petroleum refineries zeolite catalysts have been used in Fluid Catalytic Cracking (FCC) where gasoline is produced from crude oil. This process has been considered as a clean route for fuel production from light olefins such as butene or propylene, which do not inhibit the functioning of catalytic converters for engine exhaust. Olefins are regarded as building blocks of clean fuel production due to their reactivity and they are easily oligomerised. High demand of clean fuel production has force the increase in olefins supply by addition of solid catalyst such as zeolite Y, ZSM-5, etc. to catalytic crackers [35].

ZSM-5 shape selectivity favors formation of linear hydrocarbons which is a good quality for distillate fuels. In the FCC process ZSM-5 is used to improve the octane number of FCC naphtha and in the methanol-to-gasoline (MTG) and methanol-to-olefins (MTO) [36]. The use of ZSM-5 in Mobil olefin to gasoline and distillate was proposed in the 1980s to replace phosphoric acid impregnated catalyst and has been widely used to reduce oxygenate additives in gasoline formulation [37].

1.5. 3 Oligomerisation process

Oligomerisation process has been used in petrochemical industries for production of gasoline and diesel from short chain olefins [38, 39]. An increase in diesel-powered vehicles in Europe has resulted in an increased demand of diesel [36]. To meet the demand and improve quality of diesel, the focus has been on the use of light olefins for production of middle distillates through oligomerisation. Diesel production can be achieved by oligomerisation of light olefins which can be obtained from naphtha cracking. Although the preferred feedstock consists mainly of C_5-C_6 alkenes, C_2-C_4 are also used but rarely [36].

Oligomerisation products generally range from C_3 to C_{17} and these are distilled into various fractions of different chain lengths (namely petrol. diesel, kerosene, jet fuel). Distillates produced by oligomerisation contain a mixture of linear and branched alkanes and alkenes. The latter are subsequently hydrogenated to corresponding paraffin's. Low level of aromatics and low concentration of naphtha in these fuels render these fuels environmental friendly [36, 40].

Mobil olefin to gasoline and distillates (MOGD) and conversion of olefins to distillates (COD) have been the most successful processes due to the nature of their end-products [41, 42]. Oligomerised light olefins in refinery streams into C_6 iso-olefins with high octane content are used as gasoline stock and jet fuel. Mesoporous silica-alumina catalysts are used for olefin oligomerisation to gasoline and kerosene. The conversion process occurs at high pressure, 10-50 bar, and low temperature, 200-280 °C. The product contains a low aromatic and iso-olefin content[43],[41].

The two competing reactions (i.e. oligomerisation and cracking reactions) are influenced by pressure, temperature and molecular weight as well as the concentration of the hydrocarbon feedstock. Since these two competing processes are thermodynamically controlled, they tend to lead to an equilibrium mixture that is governed by thermodynamics. Temperature, concentration and nature of acid catalytic site influence oligomerised olefin to undertake either lesser or greater extent of side reaction such as coking and hydrogen transfer resulting in coke formation and aromatisation [40].

ZSM-5 has been primarily used in the petrochemical industry for petrol production from light olefins. Heavier olefins such as 1-hexene are also oligomerised for production of diesel and lubricating oils. Acid-catalysed olefin oligomerisation involves a number of competing reaction steps such as isomerisation of C_4 and longer chains, hydrogen exchange, cracking and dimerisation. ZSM-5 was found to isomerise 1-hexene to a number of different isomers [36]. Generally, the selectivity and reactivity towards dimerisation of isomer varies with carbocation substitution. Therefore gasoline quality varies according to different isomer distribution [44].

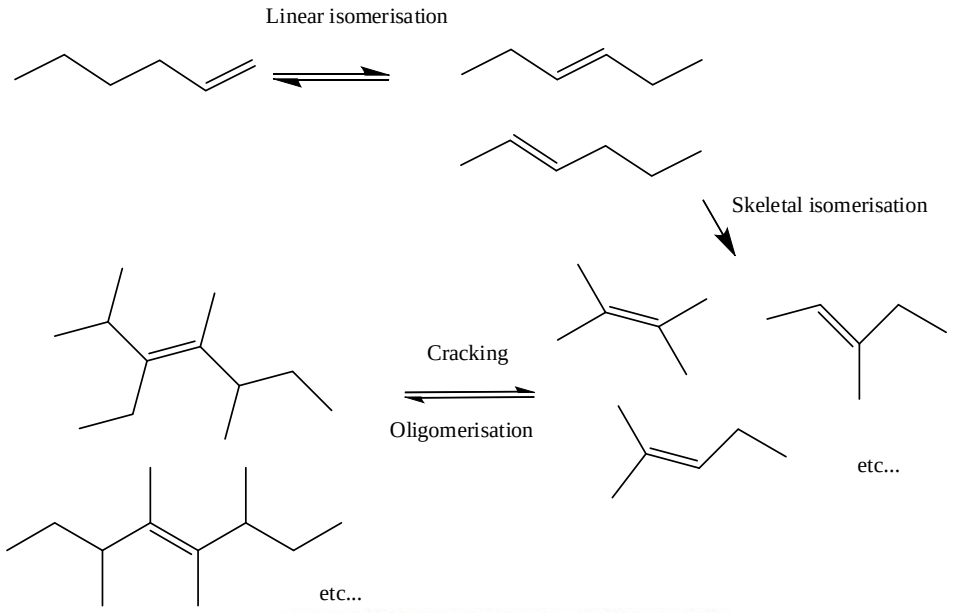

Figure 1. 6: Suggested pathway reactions during dimerisation of 1-hexene over ZSM-5 catalyst[44].

Previous studies have shown that olefin oligomerisation over acid catalyst occurs via carbocation mechanisms. Operation conditions during the reaction such as thermodynamic, kinetic, diffusional limitation and shape selectivity effects determine catalyst selectivity and activity [36]. The mechanism is initiated by a series of oligomerisation steps where primary olefinic products are formed before undergoing secondary reactions which include isomerisation, cracking and aromatisation forming a range of hydrocarbons. Produced oligomers may react with each other to form random molecular weights. The reaction pathway is affected by the acidity of the catalyst which tends to vary with aluminium content [37].

Oligomerisation occurs inside the catalyst pores and over the external surface. Mesoporous Al-MCM-41 zeolite catalysts were tested in a light olefin oligomerisation process and results showed 80% conversion and 70% selectivity towards oligomers. This catalyst showed no deactivation in the presence of nitrogen and sulphur poisons. Heavy oligomers are better moved from mesopores framework hence catalyst has a long lifetime [41].

CHAPTER 2: Experimental

2. 1 Reagents

The chemicals used in the present study were obtained from various suppliers. Table 2.1 below shows the summary of chemicals used and their purity.

Table 2. 1: Reagents used in the catalysts preparation and catalytic reactions are shown below.

Reagents	Supplier	Purity
Sodium silicate solution	Aldrich	Reagent grade
Aluminium nitrate (Al $(NO_3)_3.9H_2O$)	Fluka	98.5%
Tetraethylorthosilane(TEOS)	Fluka	98%
Cetyltrimethylammonium bromide (CTAB)	Aldrich	98%
Silver nitrate	Saarchem	99.2%
Sulphuric acid	Aldrich	95-98%
n-Hexene	Aldrich	97%
Chromium nitrate (Cr $(NO_3)_3.9H_2O$)	Aldrich	98%
Iron nitrate (Fe $(NO_3)_3.9H_2O$)	Aldrich	97%
Ammonium hydroxide solution	Saarchem	99.99

2. 2 Catalytic preparation

2.2. 1 Synthesis of pure silica MCM-41

In a beaker, 16.4 g of 98% CTAB was dissolved in 49 mL of distilled water at 75 °C. In the separate beaker 19.0 g of sodium silicate solution was diluted with 40 mL of distilled water. The solution of second content was stirred at room temperature while 1.2 g of sulphuric acid was added drop wise. CTAB solution was then added to the sodium silicate solution and stirred for 15 minutes, then diluted further with 20 mL of distilled water and stirred for a further 30 minutes. The mixture was sealed and left over-night (≈ 16 hours) for aging. Then it was transferred to an autoclave reactor for reaction at 100 °C for 72h. The catalyst was then washed and filtered and tested for the presence of Br^- with silver nitrate. The catalyst was dried and calcined at 560 °C for 6h through atmospheric air. The synthesis process was repeated at the following reaction temperatures; 90, 120, 140, 150 °C. Another set of samples were synthesised at 120 °C varying the time reaction, 22, 48, 72, 96 and 120 hours.

2.2. 2 Synthesis of metal-doped MCM-41 catalyst

- Solution A was a template solution prepared by dissolving 16.0 g of CTAB in 50 mL distilled water while heating.
- Solution B was prepared by diluting 19 g TEOS with 40 mL of distilled water, and then 1.2 g of sulphuric acid was added drop-wise.
- Solution C was prepared by dissolving a metal salts such as $Al(NO_3)_3.9H_2O$, $Cr(NO_3)_3.9H_2O$ and $Fe(NO_3)_3.9H_2O$ in 50 mL of distilled water.

Solution A was slowly added to solution B while under magnetic stirrer to mix. The gel was formed then solution C was slowly added to the mixture of solution A and B over a period of 5 minutes, then the mixture was stirred for a further 15 minutes. The mixture was diluted with 50 mL distilled water and further stirred for 30 minutes. The pH of the mixture was adjusted to a range of 10 to 10.6 using sulphuric acid/ ammonium solution. The mixture was sealed and aged for 3 days before transferring to the autoclave reactor for reaction at 150 °C

for 72 hours. The temperature of 150 °C was used because in the presence of metal, the gel could not crystallise. The catalyst was then filtered and washed to remove Br^- which was tested with silver nitrate. It was then dried and calcined at 560 °C for 6h under atmospheric air.

2.2. 3 Synthesis of mixed-metal MCM-41 catalyst

- Solution A was prepared by dissolving 16.0 g of CTAB in 50 mL distilled water while heating.
- Solution B was prepared by diluting 19 g TEOS with 40 mL of distilled water, and then 1.2 g of sulphuric acid was added drop-wise.
- Solution C was prepared by dissolving Al $(NO_3)_3.9H_2O$ in 50 mL of distilled water.
- Solution D was prepared by dissolving Cr $(NO_3)_3.9H_2O$ or Fe $(NO_3)_3.9H_2O$ in 50mL of distilled water.

Solutions A was mixed with solution B and stirred for 15 minutes before solution C and D added slowly simultaneously. The mixture was further stirred for an hour and aged overnight then proceed as described in section 2.2.2 above.

2.2. 4 Synthesis of Cr-MCM-41, Al-MCM-41 and Fe-MCM-41 by wet impregnation

Al-MCM-41, Cr-MCM-41 and Fe-MCM-41 were prepared by the wet impregnation method. Slurry was formed by adding 20 mL deionised water to 9 g MCM-41 while stirring at 100 rpm for five minutes at room temperature. A solution of Al $(NO_3)_3.9H_2O$ salt in 20mL deionised water was added to MCM-41 slurry. Then the mixture was heated at 50 °C for 10 minutes while stirring. Without stirring the solution was left in the oven at 120 °C for ~20 hours then calcined at 560 °C for 6 hours. The impregnation process was repeated for $Cr(NO_3)_3.9H_2O$ and Fe $(NO_3)_3.9H_2O$

2. 3 Characterisation of the catalysts

2.3. 1 Brunauer–Emmett–Teller (BET) surface area measurements

The BET surface area of MCM-41 was determined using a Micrometrics 3300 Tristar Surface Area and Porosity Analyser. Each sample was degassed by heating approximately 0.2 g of sample in the BET under He flow at 400 °C for 4 hours. Samples were then loaded onto the analysis station for determination of the adsorbate at -195 °C.
Then BET data was collected after 6 hours.

2.3. 2 Fourier transform infrared (FTIR) spectroscopy

FTIR spectra for zeolite catalysts appear at the vibration region between 400 cm^{-1} and 4000 cm^{-1} at room temperature, which were recorded with the Elmer Parker Infrared spectroscopy by using the powder catalyst. FTIR was used to reveal the chemistry of surface functional groups. About 2 mg of the synthesized MCM-41was fixed in the cell and skewed to measure its frequency. The spectral data were collected on the computer equipped 2012 Perkin Elmer, Inc. version 10.03.07

2.3. 3 X-ray diffraction (XRD) patterns of the catalysts

Powder XRD patterns were obtained using a BRUKER AXS D8 Advance diffractometer (radiation source was Cu-K_α and $\lambda K_{\alpha 1}$ = 1 546 Å) operated at 4 kV and 2θ range of 5-10°. Analyses were carried at a tube voltage 40 kV and current 40 mA. Samples were measured long enough for good statistics which is 1 second per step and were detected using PSD Vantec-1. A semi quantitative phase analysis was obtained using the Match 2 software to give an estimation of the amount of each phase present in the sample.

2.3. 4 Solid State Nuclear Magnetic Resonance (SS-NMR)

Solid state NMR experiments were performed on a Bruker Advance III HD Ascend standard bore 500 MHz spectrometer operating at (^{27}Al) 130 MHz and (^{29}Si) 99 MHz. The samples

were packed into 4.0 mm zirconia rotors. Direct polarization solid state ^{29}Si and ^{27}Al NMR spectra were obtained using a 4 mm magic angle spinning (MAS) BB NMR probe with spinning speeds of 5 kHz and 12 kHz, respectively.

2.3. 5 Scanning electron microscopy (SEM)

Scanning electron microscopy (SEM) micrographs were obtained using a High resolution– SEM EHT 5.00 kV equipped with Smart SEM imaging Software and AZTEC EDS Software. All samples were either carbon or gold coated before imaging. Working Distance for images is displayed on each image under the following conditions (KV used for EDS was 20 KV, working distance for EDS was 9mm, Gun Vacuum was $7.7x10^{-10}$ mbar, System Vacuum was $7.3x10^{-7}$ mbar and Filament Current was 2.35

2.3. 6 Ammonia-Temperature Programmed desorption (TPD)

TPD was performed in a U-shaped quartz tubular reactor charged with ≈ 0.1 g sample. Samples were degassed with helium (99.99% from air liquid SA) at 25 ml/min gas flow. The temperature was simultaneously increased to 500 °C at a rate of 10 °C/min and held at 500 °C for an hour before being cooled to 100 °C under helium flow. Ammonia in helium (4% NH_3 balance helium) was passed over the sample for an hour at 100 °C. Ammonia is adsorbed on to the catalyst surface area. Then ammonia is desorbed in helium at a flow rate of 25ml/min while heating the sample from 100 to 700 °C at 10 °C/min rate. The amount of desorbed ammonia relative to temperature was obtained using thermal conductivity detector.

2.3. 7 Evaluation of catalysts

Catalyst evaluation was performed at atmospheric pressure using a conventional fixed-bed quartz tube reactor and 1-hexene as a probe molecule. The reactor tube was charged with 1 g of a catalyst then heated from room temperature up to 350 °C. 1-Hexene was introduced by a syringe pump at a rate of 0.098 mL/min with the syringe of 29 mm diameter continuously for 4 hours. All products were analysed offline on either a Bruker 450 GC equipped with a BR-

Al_2O_3/Na_2SO_4 column (C_1–C_6), BR-1 column (C_7 –C_{17}) or a Bruker HC 450 gas chromatogram fitted with a wall coated open tubular column (WCOT) and detected with flame ionization detector (FID) or Thermal connectivity detector (TCD).

GC analyses were performed using either a Bruker HC 450-gas chromatogram fitted with a wall coated open tubular column (WCOT) or a Bruker HC 450-gas chromatogram fitted with two columns; namely BR-Alumina/Na_2SO_4 (for C_1–C_6 analysis) and BR-1 (for C_7 –C_{17} analysis). The eluted hydrocarbons were then analysed using a flame ionization detector (FID) and Thermal connectivity detector (TCD). Hydrogen (99.99% from Air liquidSA) was used as a carrier gas. Typically a one µL sample was injected through a syringe needle placed in an injector port maintained at 50 °C. The initial temperature of the oven was 50 °C which was maintained for 10 minutes followed by ramping to a temperature of 190˚C at a ramp rate of 8 °C per minute. The oven was maintained at 190 °C for 32 minutes.

CHAPTER 3: Study of MCM-41 synthesis conditions

3. 1 Brief introduction

MCM-41 zeolites are mesoporous silica materials prepared using cation surfactants as templates. Their preparation includes micelles which are formed in the aqueous solution, polymerisation of inorganic source as well as removal of surfactants from the pore. The morphology and porosity of these hexagonal highly ordered mesoporous species are determined by parameters such as silica source used, type of surfactant template, pH, temperature, aging time, solvents and composition of used material [45].

Described in this chapter is the effect of different parameters on MCM-41 synthesis under our laboratory environment. In this study the effect of temperature and reaction time at a constant pH of 10 were investigated. Hydrothermal synthesis temperature for mesoporous MCM-41 catalyst was studied to obtain an optimum synthesis condition for MCM-41 prepared using our reagents. The synthesis was carried out at pH 10 which is known to be suitable for synthesis of siliceous mesoporous material. Studying synthesis pH, it was found that hexagonal unit cell increases with synthesis pH and that acidic pH presence long range order distortion of mesoporous structure [46]. The treatment of synthesis gel with sulphuric acid improves the initial lamellar phase to hexagonal MCM-41 [47]. Samples were synthesized using Sodium Silica solution from Aerosil 200 Degussa and cetyltrimethylammonium bromide (CTAB) Aldrich and aged at room temperature for 16 hours, and then hydrothermally treated at 110 °C.

3. 2 Results and discussion

3.2. 1 Time effect on MCM-41 synthesis

The synthesised siliceous materials were calcined at 560 °C for 6 hours in air. Material surface area and pore size were determined by multi-point adsorption desorption technique to study the effect of crystallisation time. The obtained values of surface area and pore characterisation are tabulated in Table 3.1 below.

Table 3. 1: Surface area and pore volume of MCM-41 synthesised material at 110 °C.

Reaction time/ hours	BET surface area (m^2/g)	Ext. surface area (m^2/g)	Pore volume (cm^3/g)	*d*-spacing Å[a]	Pore diameter (Å)	Wall thickness (Å)
22 h	916	883	0.886	42.52	38.68	10.41
36 h	954	948	0.924	42.52	38.73	10.37
48 h	877	938	0.798	41.46	36.09	11.78
72 h	1081	1132	1.048	41.25	37.03	10.60
96 h	1066	1040	0.969	41.05	36.35	11.05
120 h	1054	1043	0.945	40.65	35.86	11.08

[a] the *d*-spacing reported herein was determined from the XRD shown in Fig.3.3 below

Pore volume as well as pore size distribution are the most crucial parameters for porous material and shape-selectivity catalyst. N_2 adsorption isotherms of these materials were measured at -196 °C after degassing at 400 °C for 4 hours. The isotherm plots are shown in Figure 3.1 below.

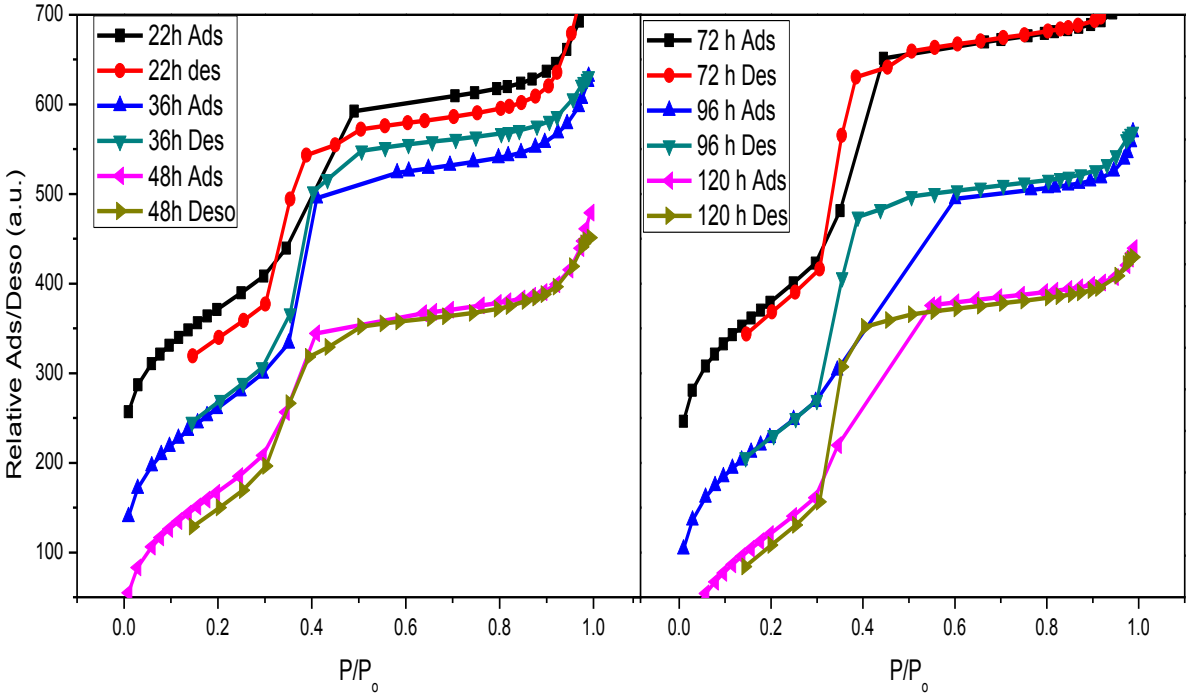

Figure 3. 1: N_2-adsorption isotherms for MCM-41 synthesised at 100 °C for (a) 22 h, (b) 36 h, (c) 48 h, (d) 72 h,(e) 96 h and (f) 120 h.

Figure 3.2 shows the pore size distribution (for the material synthesised) determined using the BJH method. All pore diameters were measured from zero to 200 Å and zoomed in the section presented below.

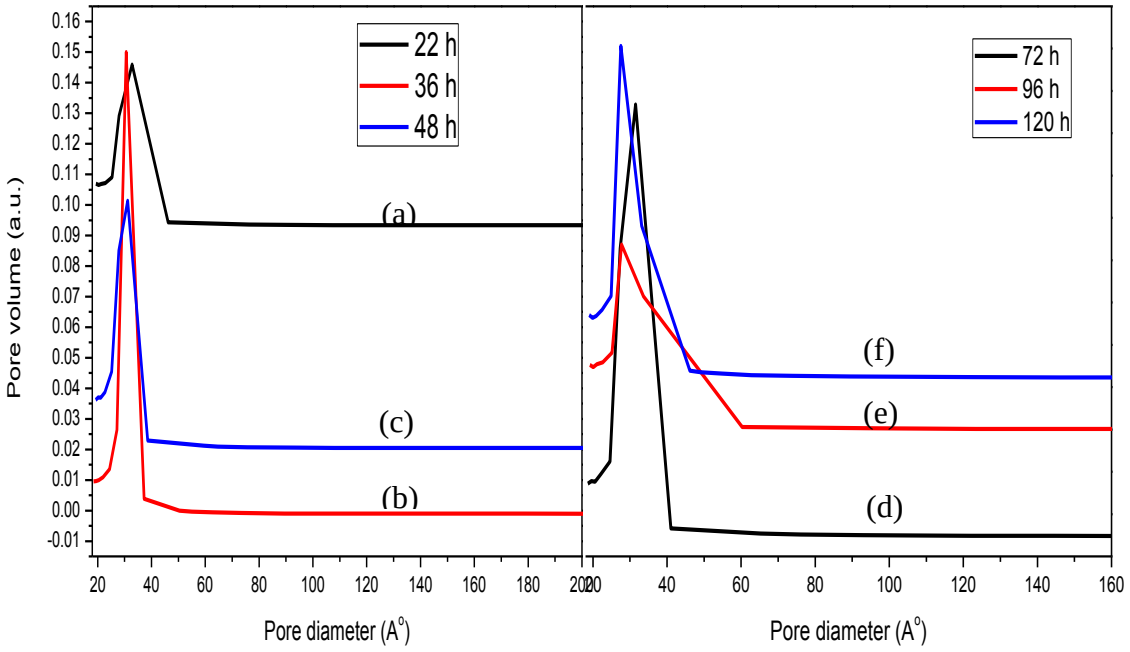

Figure 3. 2: Pore volume against pore diameter for MCM-41 synthesised at 100 °C for (a) 22h, (b) 36 h, (c) 48 h, (d) 72 h,(e) 96 h and (f) 120 h.

Nitrogen adsorption isotherms in Figure 3.1 show a strong adsorption at a relative pressure range of 0.28 to 0.38 for all the samples studied. An absorption-desorption cycle shows a hysteresis loop that is characteristics of capillary condensation into uniform mesopores. The steepness of the loop indicates the extent of mesoporous structure formed. Therefore the samples possess a good mesoporous structure and a narrow pore size distribution [48]. The steep rise at P/P_o greater than 0.30 indicates a higher pore volume suggesting the existence of mesoporisity or macroporisity among the nanocrystals forming the MCM-41 aggregates [49]. It is seen that surface area increases and reaches the optimum at 72 hours then starts to decrease.

The reduction of BET surface areas and volumes confirms the breakdown of catalyst framework. Pore volume, surface area and pore diameter of the MCM-41 catalyst synthesised in the study of time effect are summarised in Table 3.1. Increase in reaction time shows an increase in surface area from 883 to 1132 m^2/g. As seen in Figure 3.2 that pore volume is affected by the duration of the reaction as the minimal period results in less intensity of peak, indicating less pore volume. The sharpness inflection of pore diameter and the height indicates the pore volume which is less intense hence lower pore volume [50]. It seems like the optimum volume is obtained in 72 hours of reaction time. All the samples show pore size distribution centered at a diameter of 30 Å ≈ 3 nm.

X-ray diffraction patterns of synthesised powders were obtained in a 2-θ range of 1.0 to 10°. The diffractogram obtained are displayed in Figure 3.3 below. This allows the determination of material phase, purity and the degree of crystallinity. Due to higher *d*-spacing for mesoporous material, their diffraction lines appear at a lower angle.

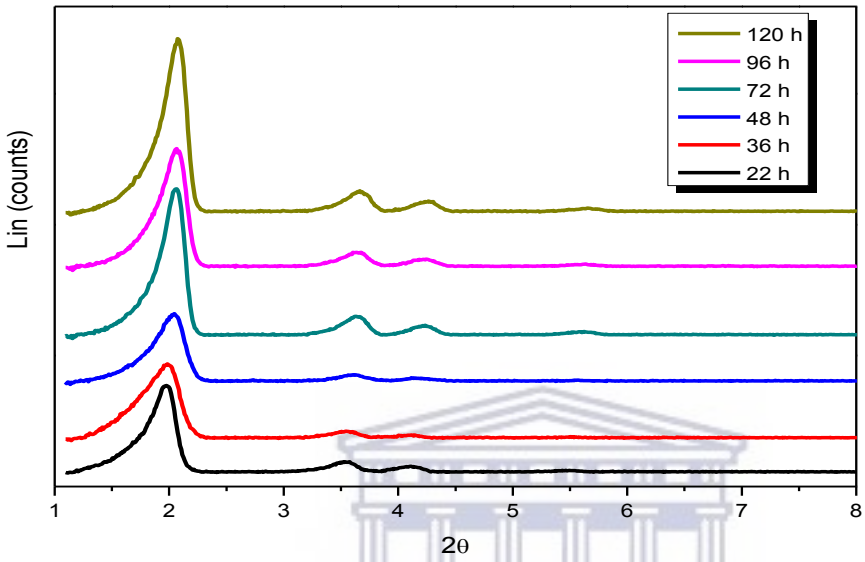

Figure 3. 3: XRD patterns at 2θ for MCM-41 synthesis at 100 °C for 22 h, 36 h, 48 h, 72 h, 96 h and 120 h.

The XRD patterns for materials synthesised over different crystallisation time show one major peak in the 2-θ region of 2° to 2.4° which corresponds to reflection (100). This peak is the characteristic diffraction assigned to hexagonal symmetry of mesoporous MCM-41. This is consistent with what was reported [51, 52]. This intense peak had a *d*-spacing of approximately 40 Å which is reduced to 37Å after calcination [53]. Reflections (110) and (200) were observed at 3.5° and 4.2° respectively. At 72 hours crystallisation period showed a small peak at 5.7°, reflection peak (210) was observed which was reported as the presence of long-range order and good textural uniform of mesoporous structure [56]. Therefore, this affirms the presence of MCM-41 structure on the synthesised materials with long-range ordering and thermal stability increases as crystallisation period increases. The crystallization time increase is proportional to the intensity of the peaks which corresponds to the increases of catalyst crystallinity [48, 54, 55].

FTIR spectra illustrated in Figure 3.4 below were all used to characterise the porous material. These were analysed from a region of 400 to 4000 cm^{-1} which provides information of material structure and the presence of organic material within the pores.

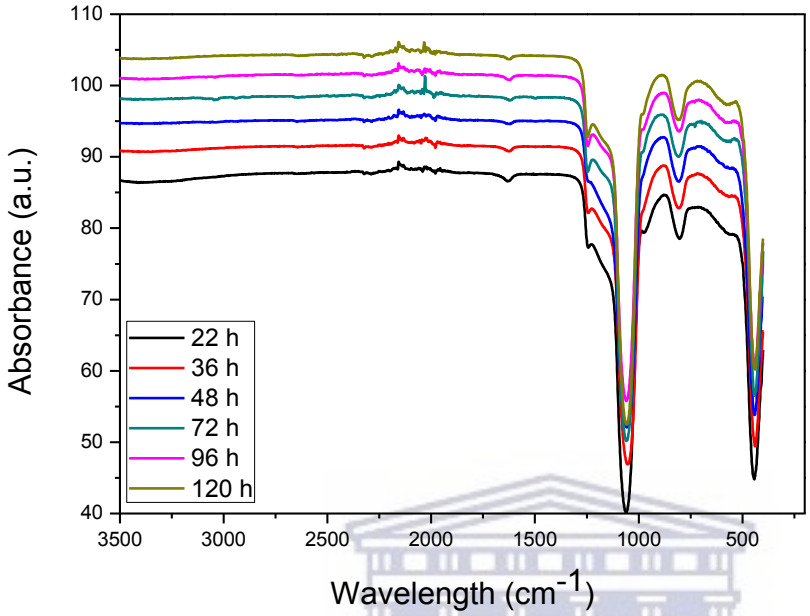

Figure 3. 4: FTIR spectra for MCM-41 synthesised at 100 °C for (a) 22 h, (b) 36 h, (c) 48 h, (d) 72 h, (e) 96 h and (f) 120 h.

The IR spectrum shows two major absorption bands at 490 and 1080 cm^{-1} and minor band at 800 cm^{-1} which is associated with hexagonal mesoporous MCM-41 [50]. Asymmetric and symmetric Si-O stretching vibrations correspond to bands at wave number 1080 cm^{-1} and 810 cm^{-1} respectively. The band at 460 cm^{-1} is due to band vibrations and stretching of Si-O-group while the band at 1230 cm^{-1} is due to Si-O-Si bridge asymmetric stretching vibrations [48].

Scanning electron microscopy was used to generate high- resolution images showing the shape of the synthesised materials and determination of elemental composition using EDS. and the SEM images can be seen in Figure 3.5 below. Chemical composition was not displayed because at this stage it was only silica.

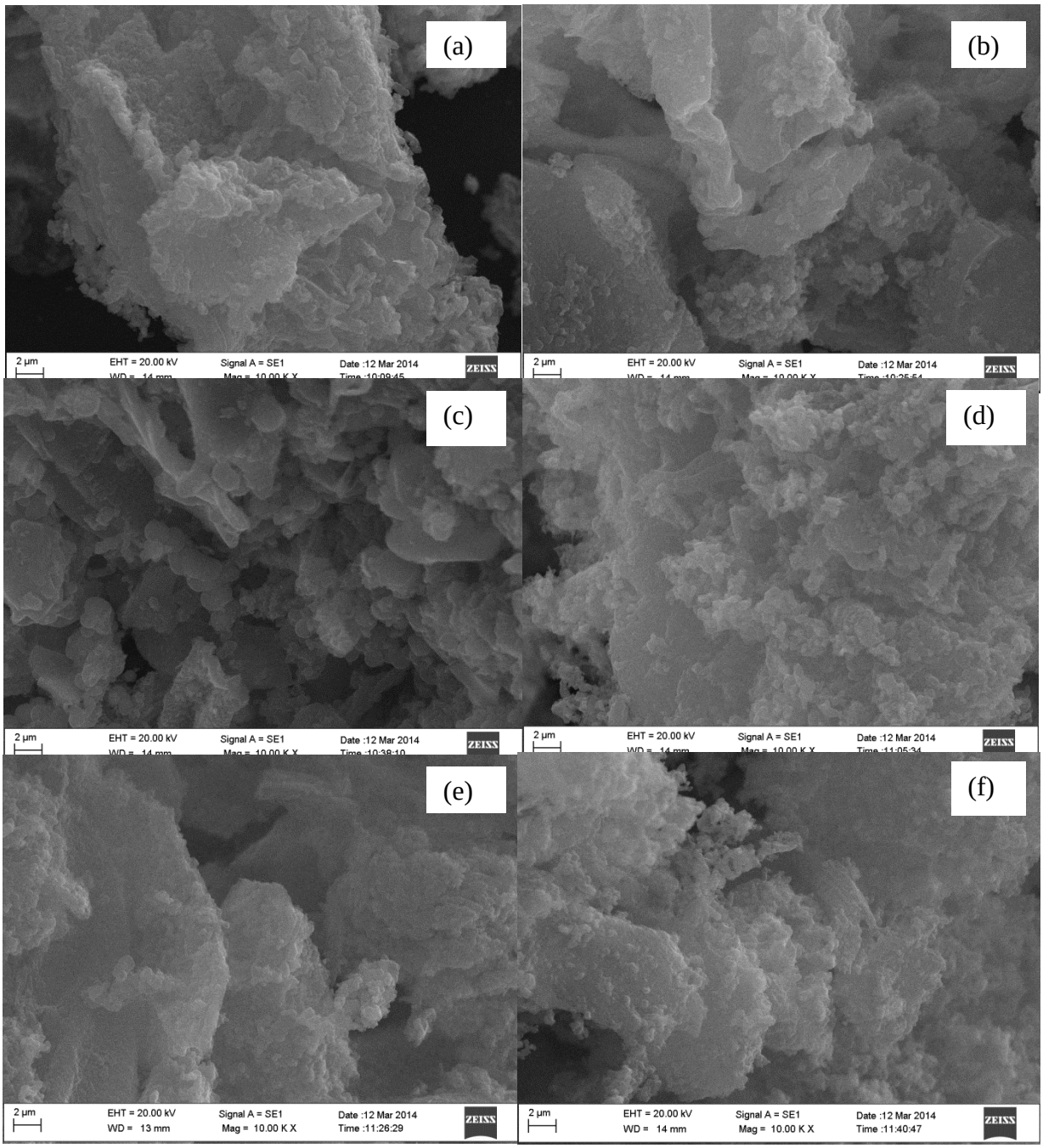

Figure 3. 5: SEM micrographs for MCM-41 synthesised at 100 °C for (a) 22 h, (b) 36 h, (c) 48 h, (d) 72 h,(e) 96 h and (f) 120 h.

The scanning electron microscopy images of as-synthesised MCM-41 as a study of crystallisation time which confirms that morphology changes due to time. Samples show the sheet like particles with tubular structured particles. Image (c) shows spherical shape particles. More clear shapes can be enhanced by using higher resolution scanning electron microscopy.

3.2. 2 Temperature effect on MCM-41 synthesis

Synthesised siliceous materials were calcined at 560 °C for 6 hours. Material surface area and pore size were characterised by the multi-point adsorption desorption technique to study the changes as it is exposed to largely increasing temperature. The obtained values of surface area and pore characterisation are tabulated in Table 3.2 below.

Table 3. 2: Surface area and pore volume of MCM-41 Catalysts synthesised for 72 hours.

Temperature (°C)	BET surface (m^2/g)	Ext. surface area (m^2/g)	Pore volume (cm^3/g)	*d*-spacing (Å)[a]	Pore diameter (Å)	Wall thickness(Å)
90	1072	1051	1.066	39.62	39.77	5.979
100	1043	1028	0.954	39.80	36.59	9.367
120	955	1001	0.920	41.52	36.76	11.18
140	31	26	0.058	41.19	32.08	9.532
150	391	378	0.443	54.98	45.23	18.26

[a] the *d*-spacing reported herein was determined from the XRD shown in Fig.3.8 below

Effects of crystallisation temperature on the synthesised material surface area were obtained using BET analysis. The nitrogen adsorption isotherm plots in Figure 3.6 were due to the amount of nitrogen adsorbed at a fixed relative pressure. Barrett-Joyner-Halenda (BJH) analysis method was used to determine the pore size distribution. The pore diameter was measured from zero to 200 Å zoomed in as shown in Figure 3.7. Silica and silica like particles were synthesised under hydrothermal conditions. The crystallisation temperature effect on texture of the synthesised MCM-41 catalyst is shown in Table 3.2 above. The BET analysis

shows that increase in synthesis temperature results in the decrease of external surface area as well as the pore volume of the catalyst. This shows that increase in temperature negatively affects MCM-41 formation as it was reported [45, 56, 57].

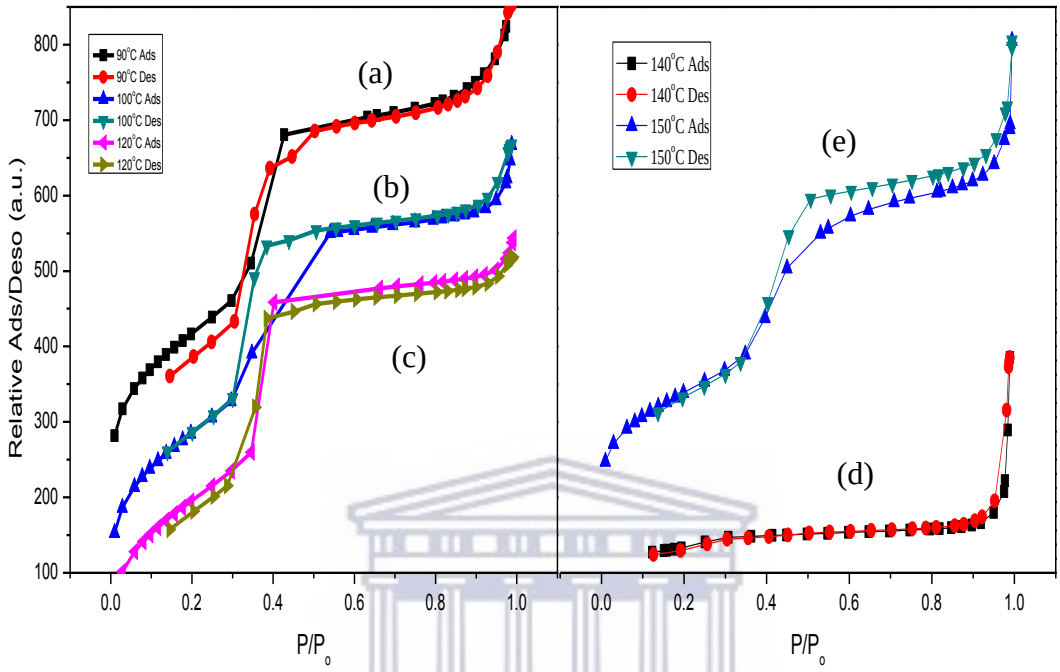

Figure 3. 6: N_2-adsorption isotherm for MCM-41 synthesised at (a) 90 °C, (b) 100 °C, (c) 120 °C, (d) 140 °C, (e) 150 °C for 72 hours.

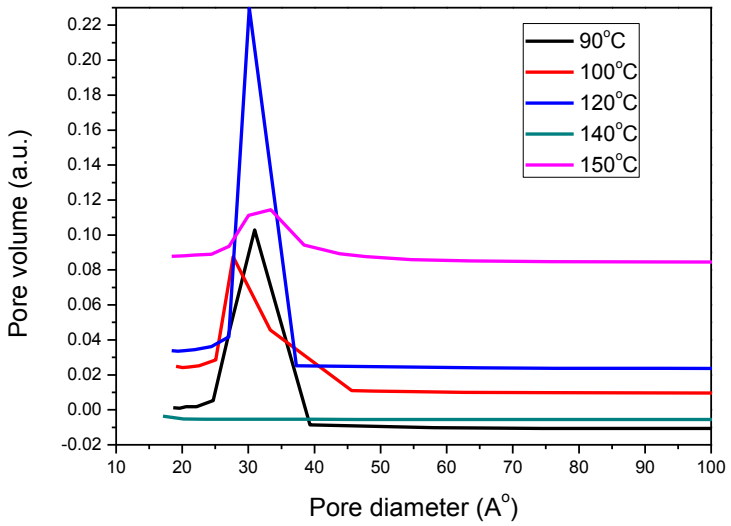

Figure 3. 7: Pore volume against pore diameter of MCM-41 synthesised at 90 °C, 100 °C, 120 °C, 140 °C and 150 °C for 72 hours.

The isotherms show a gradual increase in the relative pressure (P/P_o) range of 0.3 to 0.6. The steep is due to nitrogen condensation within the mesopores which also indicate good order of MCM-41 structure. These isotherm shapes are named type IV with mesopores of 3.0-3.2 nm diameters. The isotherm at 140 °C synthesis temperature showed a gradually increase at a relative pressure 0.9 which was confirmed by the pore volume shown in Figure 3.7 that the material had lost its mesoporisity character [45, 56, 58-60].

X-ray diffraction patterns of crystal phase were characterised at an angle from 1.0 to 10° displayed in Figure 3.8. This allows the determination of material phase, purity and degree of crystallinity. Due to higher d-spacing for mesoporous material, their diffraction lines appear at a lower angle.

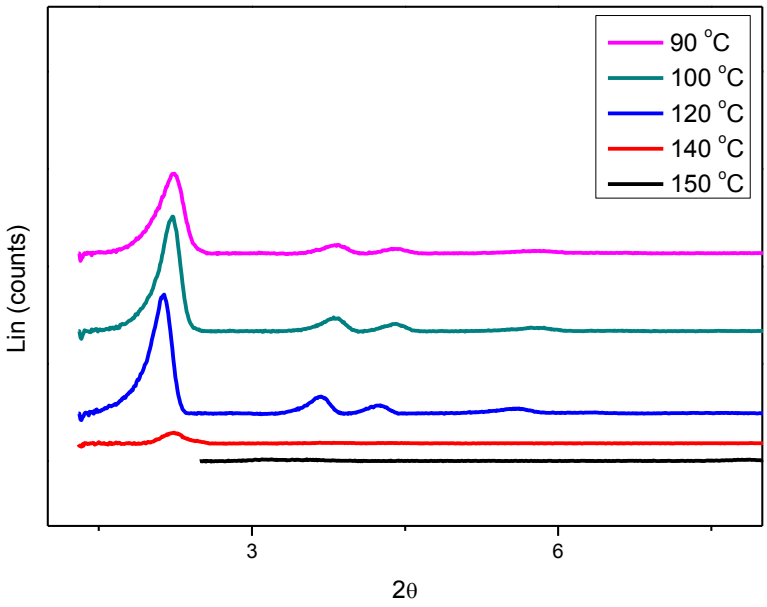

Figure 3. 8: XRD patterns at 2θ of MCM-41 synthesised at 90 °C, 100 °C, 120 °C, 140 °C and 150 °C for 72 hours.

XRD diffraction patterns show that catalyst character is retained at the reaction temperature 90 to 120 °C which all show reflection (100) indicating hexagonal structure as well as (110) and (200) indicates mesoporous material. The MCM-41 characteristics were completely lost at a reaction temperature of 150 °C as none of the (100), (110) and (200) reflection peaks were obtained. This was previously observed when comparing MCM-41 silica synthesised at 80 °C and 100 °C [58]. This was explained as the results of evaporation of water and ammonium hydroxide, therefore the solution in not completely sealed and the mixture composition cannot be kept [61]. Therefore, it was concluded that a good quality of MCM-41 mesoporous cannot be synthesised at a temperature more than 120 °C. Therefore 120 °C seems to be the best synthetic temperature as the peaks are more intense meaning the more crystallisation of the catalyst. Siliceous materials synthesised were also characterized using FTIR and data obtained is displayed in Figure 3.9 below. These were analysed from a region of 400 to 4000 cm^{-1} which provide information of material structure and the presence of organic material within the pores.

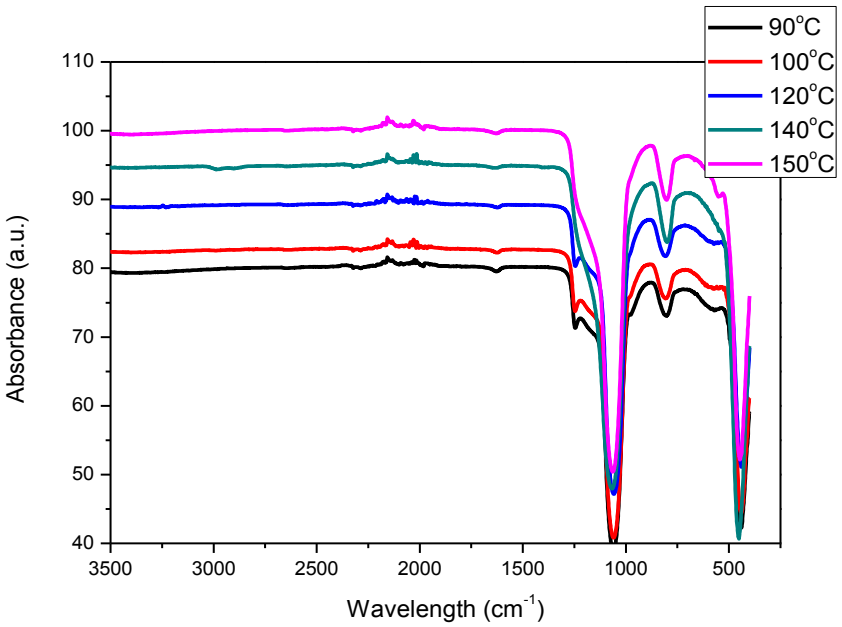

Figure 3. 9: FTIR spectra of MCM-41 synthesised at 90 °C, 100 °C, 120 °C, 140 °C and 150 °C for 72 hours.

FTIR spectrum showed bands at the same wavelength range as those when reaction time was studied with same peak intensity for all samples. At a lower temperature there is a band at 1225 cm^{-1}, which disappears as the temperature increases. This confirms a hexagonal mesoporous structure of MCM-41. The absence of the band at 2919 cm^{-1} and 2849 cm^{-1} for n-C-H and d-C-H respectively indicate that surfactant was completely removed after calcination. The small hump at 1630 cm^{-1} is believed to be due to deformational vibration of adsorbed molecules. Asymmetric stretching, symmetric stretching and bending of Si-O-Si skeleton are indicated by the bands at 1080, 750 and 495 cm^{-1} respectively [62].

These materials were imaged using Scanning electron microscopy to generate high-resolution images showing the shapes of the synthesized materials and determination of elemental composition using EDS. The images were displayed in Figure 3.10 and chemical composition was not displayed because at this stage it was only silica.

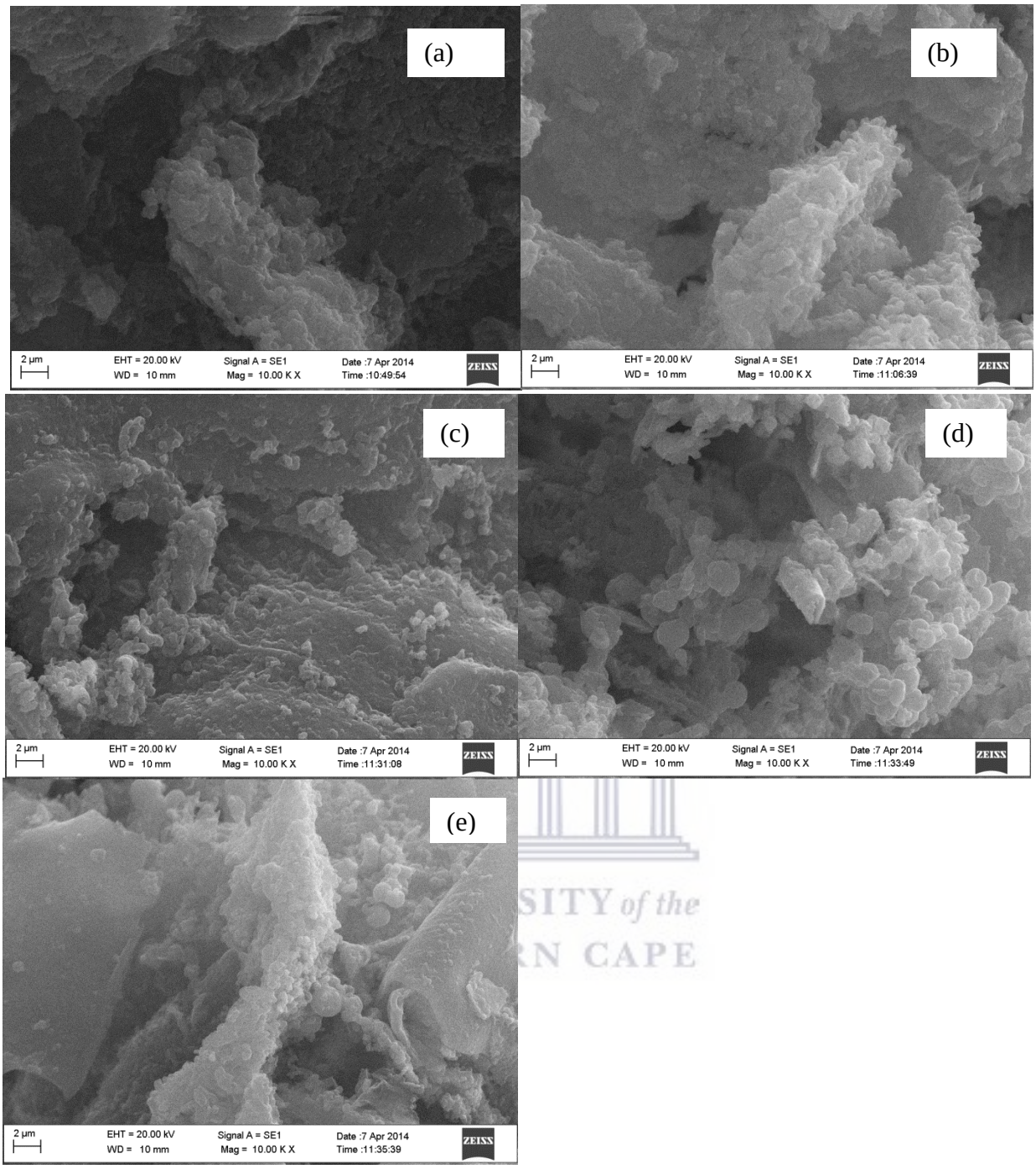

Figure 3. 10: SEM micrographs of MCM-41 synthesised at (a) 90 °C, (b)100 °C, (c) 120 °C, (d) 140 °C,(e) 150 °C for 72 hours.

SEM micrograph displayed above shows the sheet particles which is a result of amorphous silicate [63]. Particles show aggregated material with no characteristic size or shape.

Spherically shaped particles are also observed with size range of 0.8 to 1.2 nm as temperature increases and it looks like the size increased as the temperature increased.

3. 3 Conclusion

Mesoporous MCM-41 materials were synthesised under different conditions to study the effect they pose on the catalyst properties. A temperature of 100 °C was used for synthesis as it has been repeatedly reported for the synthesis of mesoporous MCM-41. It was observed that the longer the zeolite gel is kept at synthesis temperature, the greater the surface area and pore volume of the catalyst. Morphologically, all the samples were essentially the same and showed hexagonal symmetry of mesoporous MCM-41 although defenses were observed in their extents of crystallinity. XRD patterns show that an increase in crystallisation time lead to higher peak intensity and narrower width at half-height for all reflections indicative of higher crystallinity. The highest surface area was observed with a sample kept at synthesis temperature of 110 °C for 72 hours. This duration was deemed suitable and optimal for the synthesis of these materials in our laboratories.

The study of synthesis temperature showed a higher surface area at 90 °C to 100 °C which was within the surface area range when crystallisation time of the material was studied. Pore volume increased with temperature and reached a maximum at 120 °C this declined at higher temperatures. This was supported by XRD patterns when there were no reflections at 140 °C as well as 150 °C. This indicates that at higher temperatures hexagonal symmetry of mesoporous MCM-41 is depleted. Morphology showed that the shape of species is formed as the temperature increases. It is concluded that quality mesoporous MCM-41 can be synthesized at 100 °C to 120 °C for the duration of 72 hours.

CHAPTER 4: Metal -doped mesoporous MCM-41

4. 1 Brief introduction

Metal doping the catalyst is advantageous to the catalyst because it increases the lifespan of the catalyst during thermal reactions and allows processing of sample at a higher flow rates and they are used as acid catalyst. Metal loading also reduces the channels resulting in uniform species with a greater mechanical stability of sorbent [64]. Si/M (metal) ratio plays an important role in the reaction system such as determining the structure and composition of the crystallised product. Low Si/M ratio samples are synthesised at strong alkalinity while higher Si/M ratio are synthesised at weak alkalinity. To neutralise the reaction medium, acid is used so all samples are synthesised at same pH. Suitable optimised conditions needed to be achieved so as to obtain the desired Si/Al ratio in the end product such as the use of Cetyl trimethylammonium bromide (CTAB) as the template [65].

One of the aims of this research was to investigate the effects of doping MCM-41 with aluminium, chromium and iron salts on the physicochemical properties of MCM-41. Metal doping in MCM-41 has been reported to increase the acid sites on these siliceous materials. These catalysts are aimed for production of heavier hydrocarbons from short chain alkenes such as 1-hexene.

4. 2 Results and discussion

4.2. 1 Al-MCM-41

4.2.1. 1 Synthesis of MCM-41 using sodium silicate as silica supply

Synthesised siliceous materials were calcined at 560 °C for 6 hours. Materials surface area and pore size were characterised by a multi-point adsorption desorption technique to study

the changes as it is exposed to largely increasing temperature. The obtained values of surface area and pore characterisation are tabulated in Table 4. 1 below.

Table 4. 1: Effect on BET surface area and texture properties as the aluminium content increases.

Si/Al ratio	BET surface (m^2/g)	Ext. surface area (m^2/g)	Pore volume (cm^3/g)	*d*-spacing (Å)[a]	Pore diameter(Å)	Wall thickness(Å)
20	85	97	0.415	42.52	17.78	31.32
30	173	187	0.678	42.80	19.31	30.11
50	336	365	0.973	51.15	29.11	29.95
80	509	496	0.870	53.53	19.93	41.88
95	472	566	0.918	59.47	25.56	43.11
110	481	597	0.980	43.89	30.58	20.10

[a] the *d*-spacing reported herein was determined from the XRD shown in Fig. 4.3 below

Al-MCM-41 was hydrothermally synthesised with different Si/Al ratio range from 20 to 110 at 150 °C for a period of 72 hours. In Section 4.1 we have concluded that 120 °C was the best synthetic temperature for these mesoporous materials but in the presence of aluminium the gel could not crystallise so the temperature was raised to 150 °C. Pore volume and BET surface area displayed in Table 4.1 seem to decreases with an increase in aluminium content in the catalyst which was also reported in the synthesising Si-MCM-41 using ethyl silicate [69].

Pore volume as well as pore size distribution are the most crucial parameters for porous materials and shape-selectivity catalysts. Nitrogen adsorption isotherms of these materials were measured at -196 °C after degassing at 400 °C for 4 hours. The isotherm plots in Figure

4.1 are due to the amount of nitrogen adsorbed at a fixed relative pressure. BJH method was used to determine the pore size distribution shown in Figure 4.2.

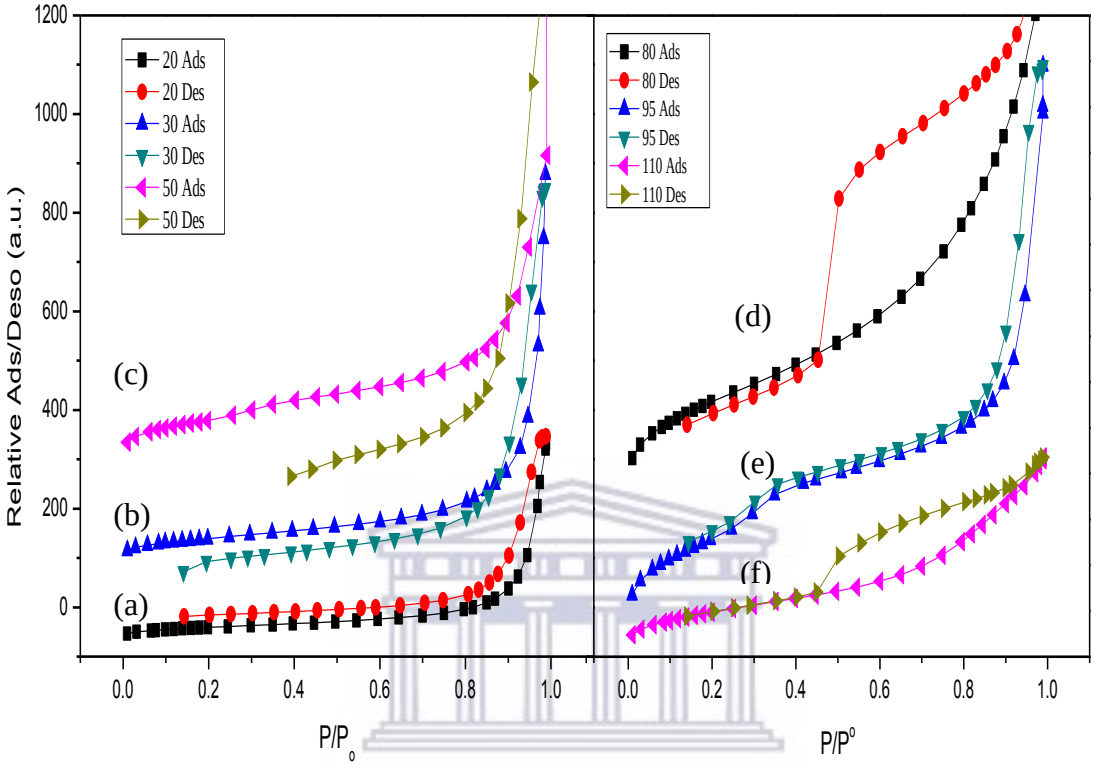

Figure 4. 1: N_2-adsorption isotherms for MCM-41 synthesised with Si/Al ratios of (a) 20, (b) 30, (c) 50, (d) 80, (e) 95 and (f) 110 at 150 °C for 72 hours.

In the present study it is observed that the pore size decreased from 3.0 to 2.5 nm (30 to 25Å) as the aluminium content was increase. Similar observation was reported where conclusion was that the reduction in pore volume is due to increased wall thickness and structural irregularity [66, 67]. Nitrogen isotherms show a type III curve at lower Si/Al ratios which indicates the presence of micropores and type IV curve is seen as Si/Al ratios increases. Therefore, the mesoporous structure is retained at Si/Al ratios of 95 to 110.

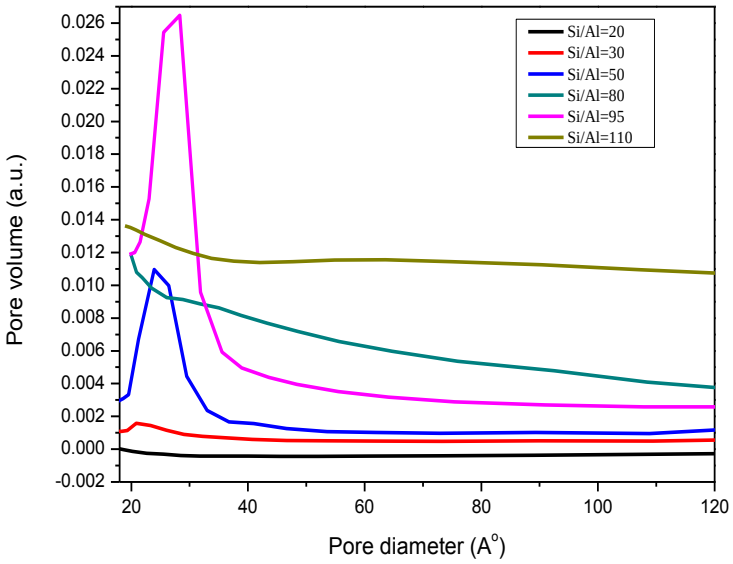

Figure 4. 2: Pore volume against pore diameter for MCM-41 synthesised with Si/Al ratios of 20, 30, 50, 80, 95 and 110 at 150 °C for 72 hours.

Synthesised materials of different silica to aluminium ratio were analysed by XRD in a region of 1.0 to 10° two-theta angle. X-ray diffraction patterns of powder are displayed in Figure 4.3. This allows the determination of material phase, purity and degree of crystallinity. Due to higher *d*-spacing for mesoporous material, their diffraction lines appear at a lower angle

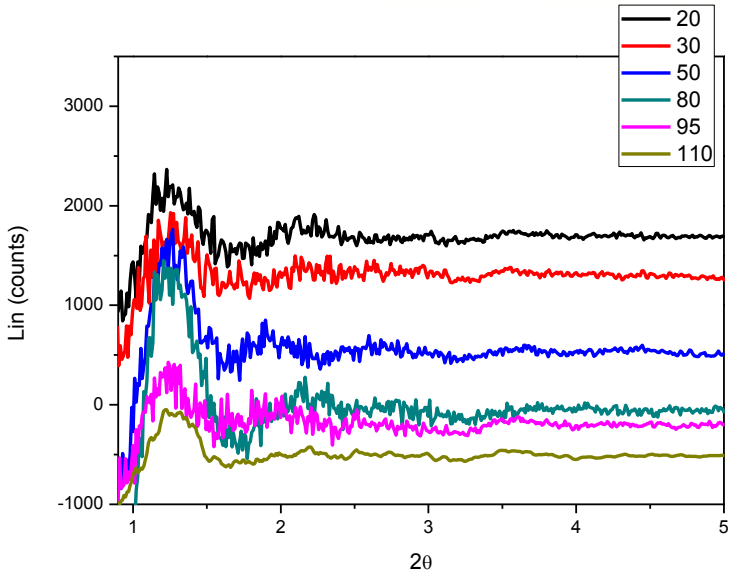

Figure 4. 3: XRD patterns of MCM-41 catalyst 41 synthesised with Si/Al ratios of 20, 30, 50, 80, 95 and (f) 110 at 150 °C for 72 hours.

The diffraction patterns shows a peaks reflection (100) for Si/Al ratio of 20 to 110 with *d*-spacing range at 42.52 to 59.47 Å corresponding to hexagonal structure of mesopores MCM-41 catalyst at 0.8-1.5° angle [68]. The increase in *d*-spacing is an indication of aluminium incorporation as the ionic radius of Al^{3+} (53 pm) is larger than that of Si^{4+} (40 pm)[69]. The reflection 110 was obtained at 1.8-2.5° with lower intensity indicating the loss of long-range structure and non-mesoporous structure was lost by the introduction of aluminium. The (100) diffraction peak has broadened and moved to a lower angle referring to MCM-41 diffraction, which is the result of aluminium introduction. This suggests the decrease in mesoporous structure and narrowing of the pore size of the catalyst. The broadening and lower intensity of reflection (100) is the character of distortion in long range ordering of mesoporous structure and this is believed to be due to synthesis pH [46, 70].

Silica-alumina materials synthesised were also characterised using FTIR analysis from a region of 400 to 4000 cm^{-1}. This provides information of material structure and the presence of organic material within the pores. After the oligomerisation of 1-hexene the catalyst was analysed again by FTIR for comparison with the original catalyst. The used catalyst is plotted in red together with the catalyst before reaction as illustrated in Figure 4.4 below. Bands at 470 cm^{-1} correspond to bending of $Si\text{-}O^-$ groups on the surface. While the bands at 810 and 1090 cm^{-1} correspond to symmetric and asymmetric Si-O stretching vibrations. These bands are the same as the ones obtained for silica MCM-41. The band at 2980 cm^{-1} is associated with hydroxides which is more visible on the ratio of 95 and 110. After the oligomerisation reaction the catalyst shows a new band at 3400 cm^{-1} wavelengths which is due to carbon deposition during the reaction. Over time this may result in coke deposition therefore negatively affecting the catalyst activity. A weak band at a wavenumber 960 cm^{-1} is associated with substituted aluminium to silica, Si-O-Al [71, 72].

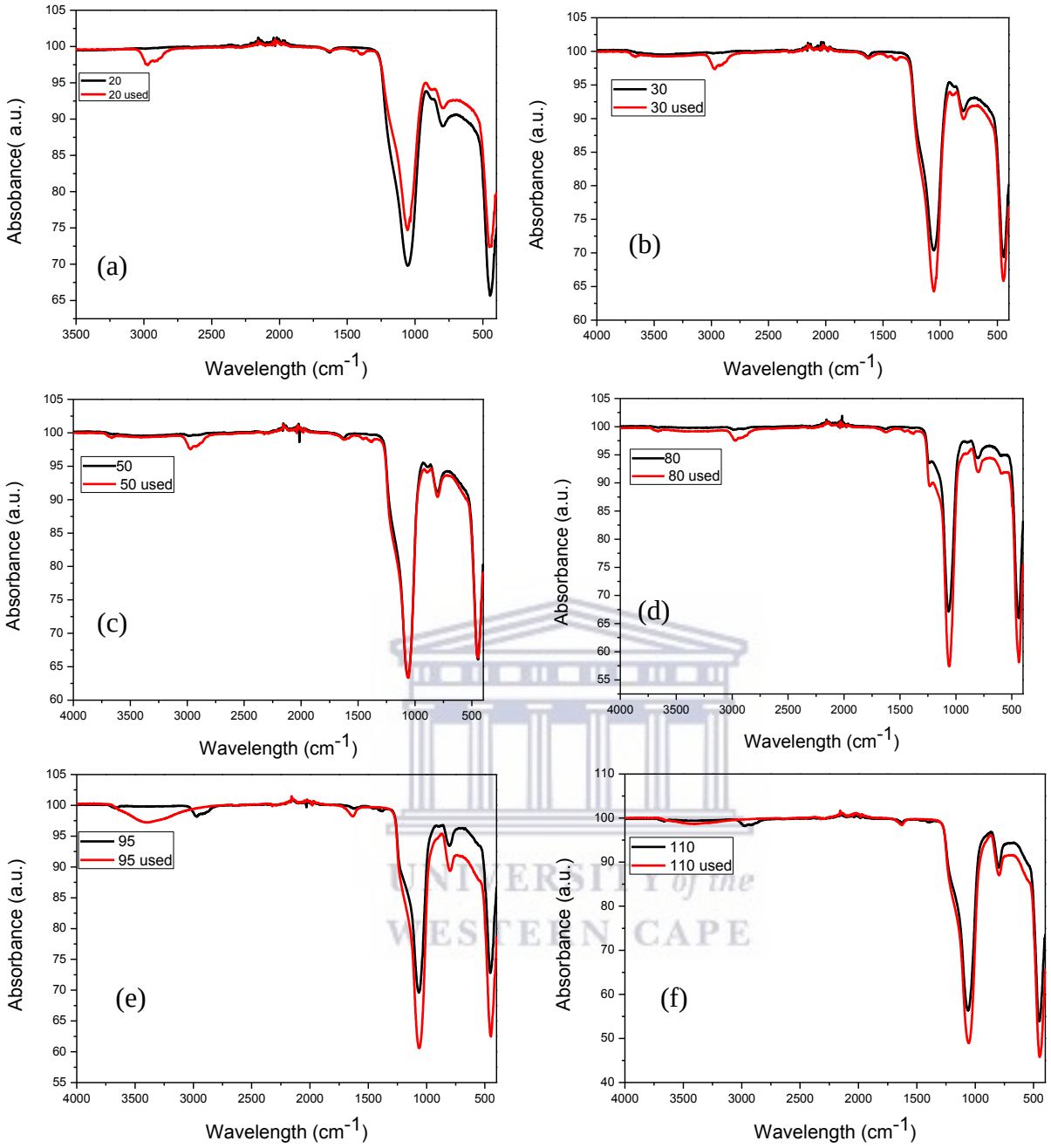

Figure 4. 4: FTIR spectra of MCM-41 synthesised with Si/Al ratios of (a) 20, (b) 30, (c) 50, (d) 80, (e) 95 and (f) 110 before and after 1-hexene oligomerisation.

These materials were imaged using Scanning electron microscopy to generate high-resolution images showing the structural shapes of the synthesised materials and determination of elemental composition using EDS. The images are displayed in Figure 4.5 below.

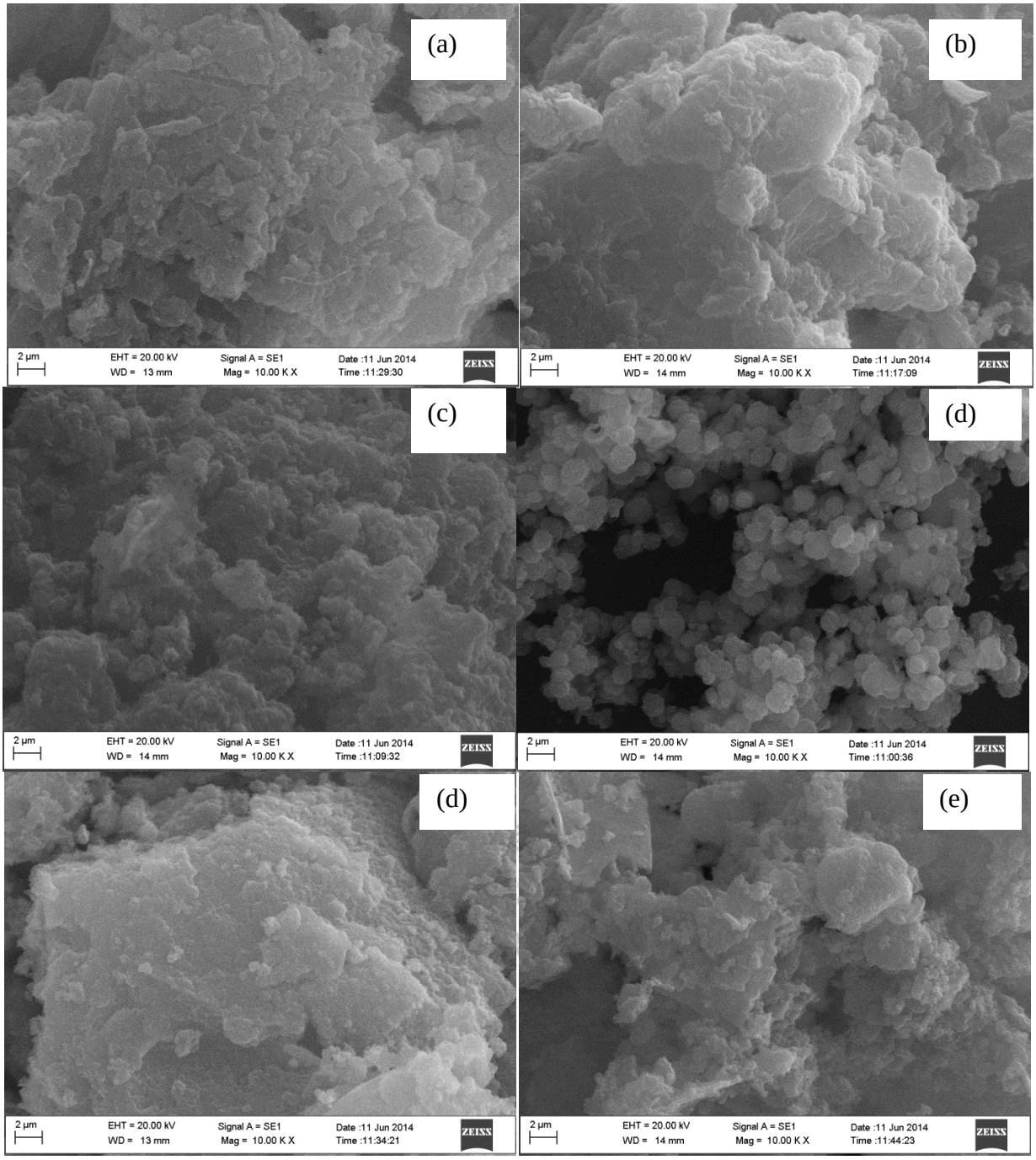

Figure 4. 5: SEM micrographs of MCM-41 synthesised with Si/Al ratios of (a) 20, (b) 30, (c) 50, (d) 80, (e) 95 and (f) 110.

SEM micrographs shows a layer of the material stacked together in flat sheets except for a catalyst synthesised with Si/Al ratio of 80 which showed a spherical shape at a size range of 0.5 to 1µm. Even when structural shapes were obtained in Si/Al ratio of 80 these particles seem like they are not likely to form shapes. This may be due to the synthetic conditions,

reagents as well as the template used. It has been reported before that particle shape did not form because propanol ratio to CTAB affects the morphology of mesoporous silica [56]. It could be assumed that reagents play a major role when preparing these materials as it is seen in Table 4.2 as the uneven amount of Al is successfully incorporated. Si/Al ratio of 80 and 95 showed to have equal Si/Al ratio of 110. The plan was to synthesised materials with Si/Al ratio of 20 to 110 but the resultant material showed Si/Al ratio from 3 to 11.

Table 4. 2: Elemental composition of synthesised material detected by energy dispersive spectroscopy (EDS).

Samples code	Si atomic %	Al atomic %	Si/Al ratio	SiO_2/Al_2O_3 ratios
Si/Al 20	15.43	6.31	3	6
Si/Al 30	82.20	17.80	5	10
Si/Al 50	10.12	1.66	6	12
Si/Al 80	16.94	1.63	10	20
Si/Al 95	16.45	1.71	10	20
Si/Al 110	10.62	1.00	11	22

Synthesised materials were tested for catalytic activity in the oligomerisation of 1-hexene using a fixed bed reactor made of quarts as described in chapter 2. The product obtained hourly at 350 °C was analysed by gas chromatography. The effect of crystallisation time on catalyst properties for the conversion of product is shown in Figure 4. 6 below. The selectivity of the synthesised materials in the conversion of 1-hexene at a WHSV of 4 h^{-1}at 0.980 mL/min rate and 1 bar pressure to hydrocarbons is shown in Figure 4.7 below. Addition of Al to these silicate species is known to increase acid sites hence increase the activity of the catalyst. In the figure below it shows that as Si/Al ratio of 110 conversion increases over time. This was different for other materials with a higher amount of Al which shows higher conversion at the beginning and decreases with increase in time.

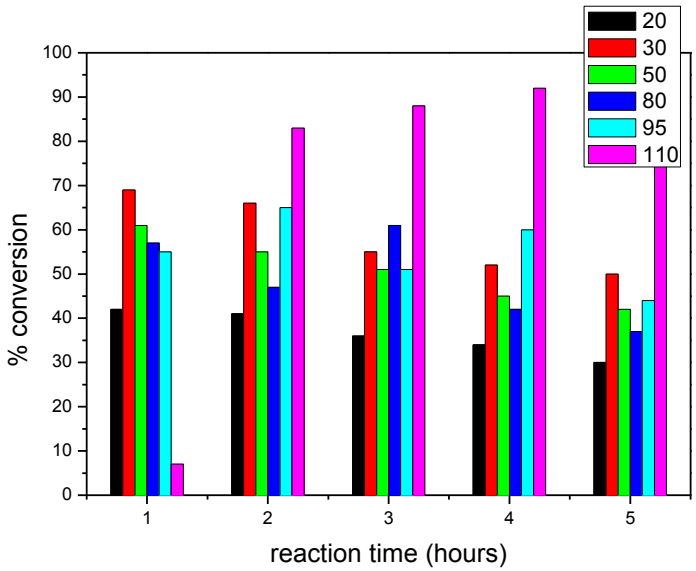

Figure 4. 6: Conversion of 1-hexene to liquid products over MCM-41 catalysts with different ratios of Si/Al on a quartz fixed bed reactor at 350 °C.

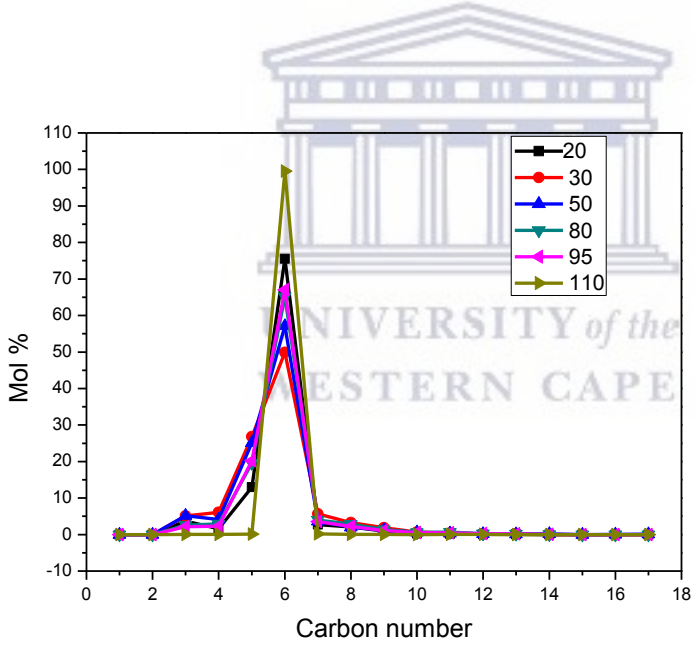

Figure 4. 7: Selectivity of various ratios of Si/Al-MCM-41 catalysts in the oligomerisation of 1-hexene to liquid hydrocarbon product on a quartz fixed bed reactor at 350 °C.

Mesoporous MCM-41 showed to be selective towards C_6 hydrocarbons as seen in Figure 4.7 above. With aluminum addition the materials seem to also form C_5 hydrocarbons with higher mole percentage at higher Al content. As we aim for heavier hydrocarbon the synthesised

material was not suitable for the reaction as we obtain cracking and isomerisation of 1-hexene.

4.2.1. 2 Synthesis of MCM-41 using TEOS as silica supply

Table 4.3 below displays the external surface area and pore volume of the synthesised material analysed by BET analysis. Material surface area and pore size were characterised by multi-point adsorption desorption technique to study the changes as different amount of aluminium is incorporated in the siliceous surface as well in the pore. The wall thickness in the table shows how the aluminium addition affects the catalyst frame structure.

Table 4. 3: The influence of aluminium on pore diameter and exterior surface area of mesoporous MCM-41.

SiO_2/Al_2O_3 ratio	BET surface (m^2/g)	Ext. surface area (m^2/g)	Pore volume (cm^3/g)	*d*-spacing (Å)[a]	Pore diameter (Å)	Wall thickness (Å)
MCM-41	955	1001	0.920	41.52	45.23	2.713
20	546	715	0.962	44.34	20.57	30.63
30	593	783	0.881	41.16	26.90	20.63
50	421	503	0.611	36.94	26.96	15.69
80	299	309	0.523	36.74	19.66	22.76
95	298	379	0.588	39.49	21.42	24.18
110	281	288	0.602	39.30	28.84	16.54

[a] the *d*-spacing reported herein was determined from the XRD shown in Fig. 4.10 below

Pore volume as well as pore size distribution are the most crucial parameters for porous material and shape-selectivity catalyst. Nitrogen adsorption isotherms of these materials were

measured at -196 °C after degassing at 400 °C for 4 hours. The isotherm plots in Figure 4.8 are due to the amount of nitrogen adsorbed at a fixed relative pressure. BJH method was used to determine the pore size distribution. Pore diameter was measured from zero to 200 Å and zoomed to a region shown in Figure 4.9. This shows the effect of aluminium incorporation on the pores of siliceous materials.

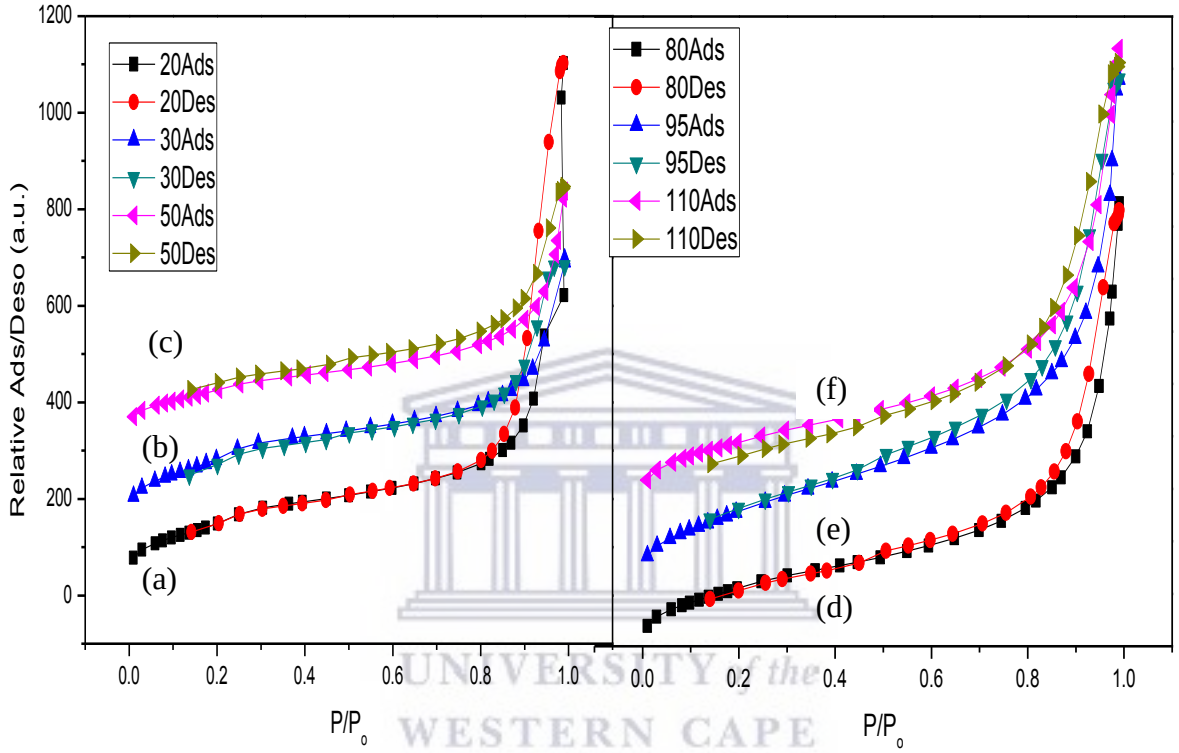

Figure 4. 8: N_2-adsorption isotherm for MCM-41 synthesised with Si/Al ratio of (a) 20, (b) 30, (c) 50, (d) 80, (e) 95 and (f) 110.

Nitrogen adsorption isotherms of Al-MCM-41 at different ratios showed type III character. These materials possess both microporous and mesoporous structure. Zeolites micropores structure is indicated by the rise of sorption at P/P_o less than 0.05. Increases of adsorption at P/P_o 0.2-0.5 correspond to the presence of mesopores on the synthesized material [73].

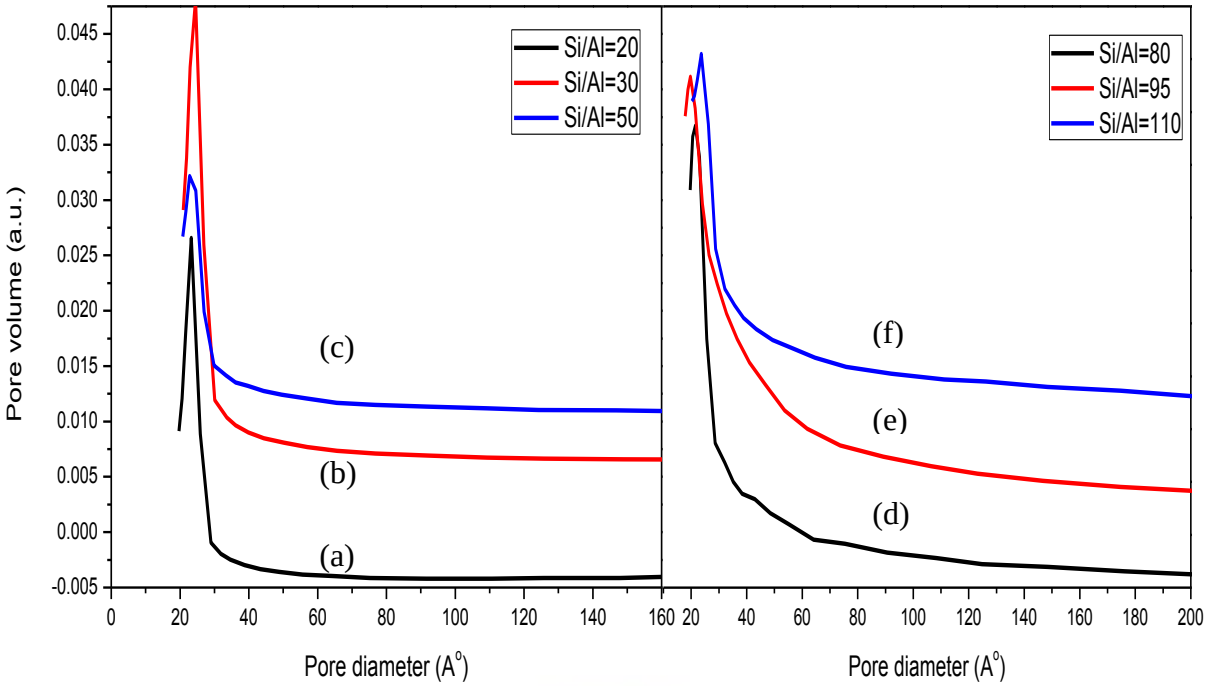

Figure 4. 9: Pore volume against pore diameter for MCM-41 synthesised with Si/Al ratios of (a) 20, (b) 30, (c) 50, (d) 80, (e) 95 and (f) 110.

Pore size distribution curves for Al-MCM-41 have sharp peaks ranging at 19-25 Å which is approximately 1.9-2.5 nm which was close to what was reported with an average of 1.92-2.02 nm pore diameter [58]. This showed a decrease in pore diameter compared to non-aluminium synthesised MCM-41 found to have pore size ranging between 3.0-3.2 nm (≈ 30-32 Å) above. Table 4.3 also shows the decrease in surface area and pore diameter due to aluminium incorporation. Previous studied were reported with different silica supply amount during synthesis and discovered that higher content of TEOS in the initial gel results in non-mesoporous species due to high ethanol production as hydrolysis and condensation of TEOS occurs [74].

X-ray diffraction patterns of powder materials were obtained at region of 1.0 to 10° as shown in Figure 4.10 below.

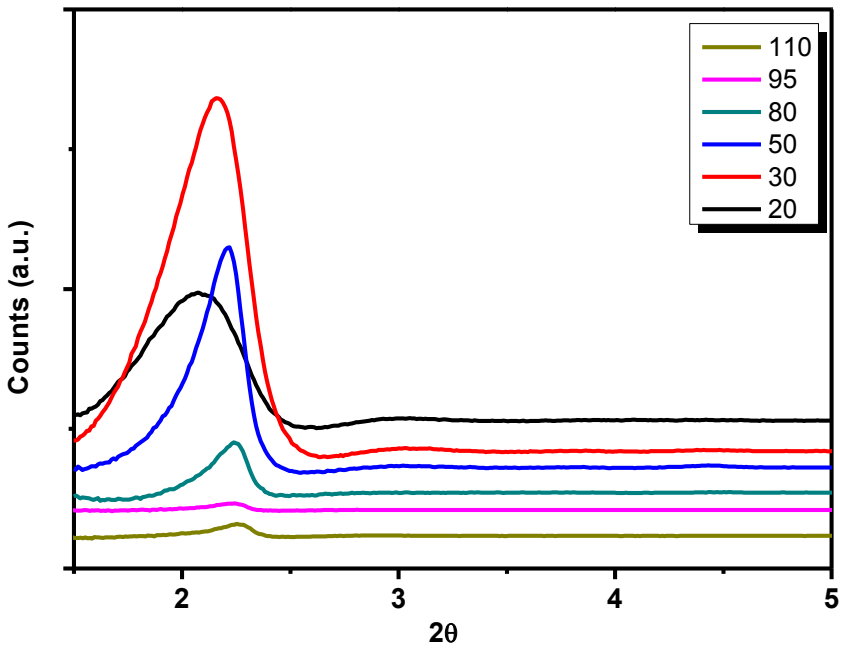

Figure 4. 10: XRD pattern of MCM-41 catalyst synthesised with Si/Al ratio of 20, 30, 50, 80, 95 and 110.

Due to higher *d*-spacing for mesoporous material, their diffraction lines appear at a lower angle while showing the effect of aluminium on the peaks intensity. The XRD patterns of materials show one major peak at 2θ ranging between 1.2° to 2.6° which indicates a hexagonal mesoporous MCM-41 structure on the synthesised catalysts. Al incorporation result in intensity reduction and peak broadening and they shift to a higher angle as more aluminium is incorporated [60]. Conclusion was that regularity of mesoporous structure decreases while pore size narrows with introduction of aluminium. Si/Al ratio 30 and 50 show a high intensity at refraction (100). The lower intensity of other material is believed to be due to direct mixed-gel synthesis which causes disruption on structural ordering. A slightly shift in peaks at reflection (100) to high 2θ angle indicates a decrease in *d*-spacing as Al content increases which is seen in the table [48].

Powder material were analysed by FTIR technique from a region of 400 to 4000 cm^{-1} before and after the oligomerisation process as shown in Figure 4.11 below.

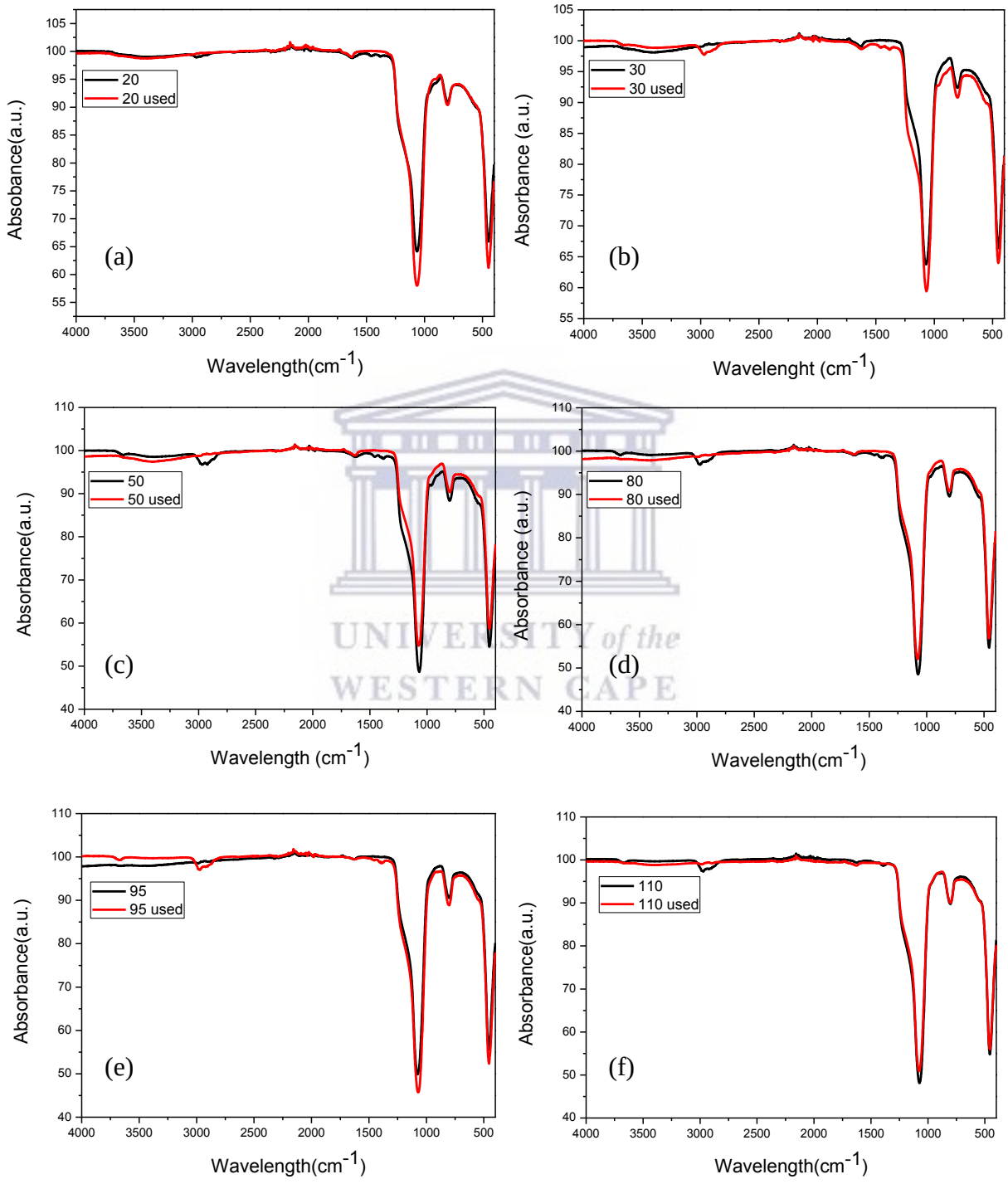

Figure 4. 11: FTIR spectra of MCM-41 synthesized with Si/Al ratios of (a) 20, (b) 30, (c) 50, (d) 80, (e) 95 and (f) 110 before and after 1-hexene oligomerisation.

Infrared spectroscopes for as-synthesised Al-MCM-41 catalyst show that all the bands obtained for MCM-41 were also present in these materials. A weak band at 960 cm^{-1} was only observed for Si/Al = 50 which is an indication of aluminium incorporation. Absence of the bands at 3618 cm^{-1} which is Al-O vibration indicates that octahedral sheet of inner Al-O has been destructed [75]. Red spectra show new peak at 3400 cm^{-1} wavelengths which is a carbon deposition during oligomerisation reaction. When the samples were calcined at 560 °C and analysed under infrared spectroscopy they show same spectroscopy as before the catalyst undergoes oligomerisation reaction. This shows that the catalyst is recovered to a certain degree.

Figure 4.12 shows the images of synthesised materials obtained by scanning electron microscopy. SEM analyses of synthesised Al-MCM-41 zeolites were done after calcination at 560 °C for 6 hours. Morphology shows rod-shaped structures of the synthesised material which did not change with the difference in Si/Al ratio. The uniformity of this shape was previously observed expects that species were in round shape [76]. In the presence of CTMABr as surfactant and addition of silicate species in liquid crystal phase molecules assembly to hexagonal liquid crystal phase. Therefore it is believed that the rod structures transform to MCM-41 hexagonal mesostructure [15].

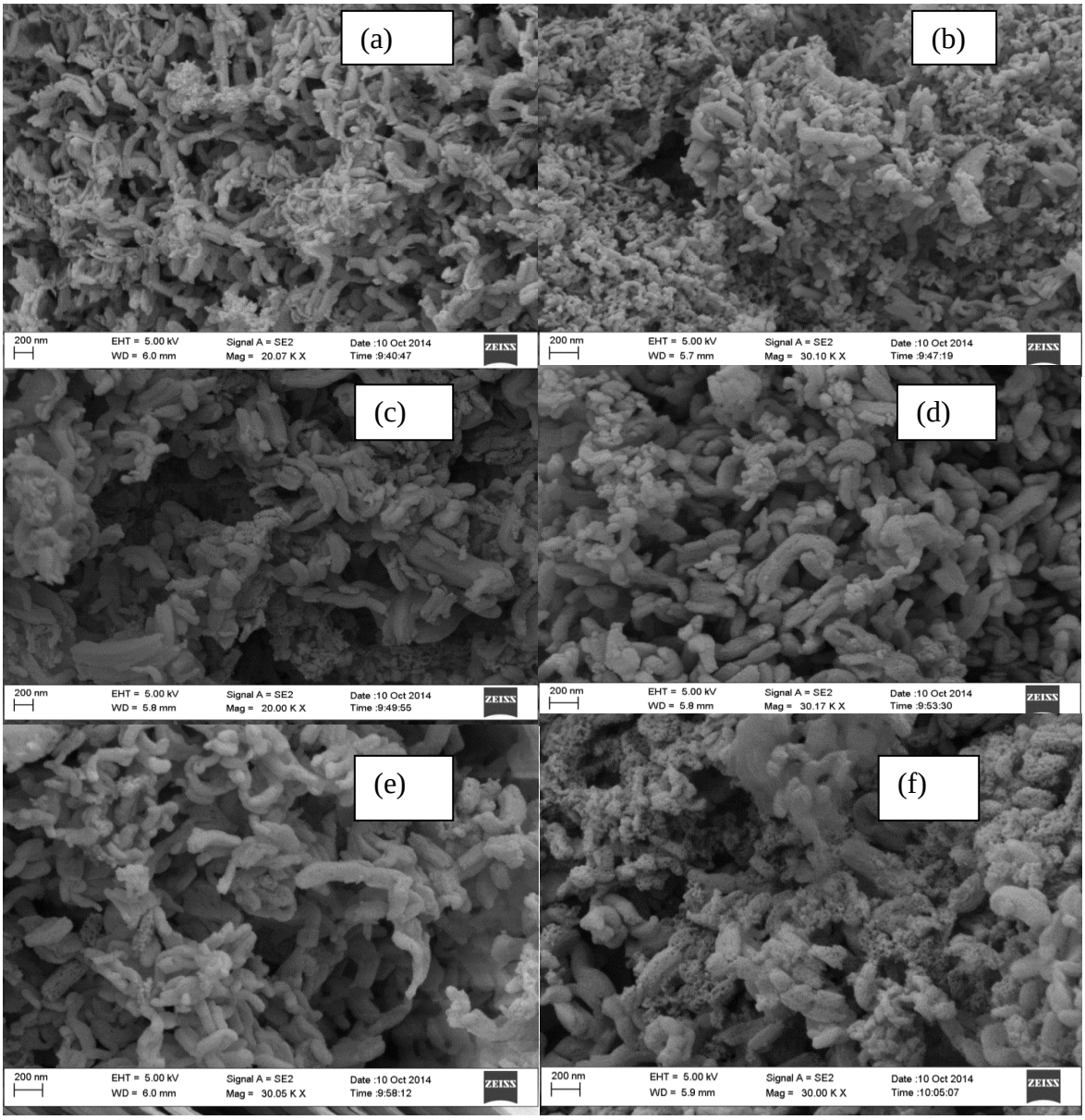

Figure 4. 12: SEM micrographs of the mesoporous MCM-41 synthesised with Si/Al ratios of (a) 20, (b) 30, (c) 50, (d) 80, (e) 95 and (f) 110.

Each catalyst atomic percentage was detected by EDS analysis is shown in the Table 4.4 and the successfully incorporated aluminium was calculated. It shows that a successfully synthesised Si/Al ratio was from 20 to 102 hence the behaviour of the catalyst in oligomerisation is different.

Table 4. 4: Elemental composition of samples detected by energy-dispersive spectroscopy (EDS).

Sample code	Si atomic %	Al atomic %	Si/Al ratio	SiO_2/Al_2O_3 ratio
Si/Al 20	30.63	3.09	10	20
Si/Al 30	38.76	2.47	16	32
Si/Al 50	37.85	1.72	22	44
Si/Al 80	30.23	0.78	39	78
Si/Al 95	38.11	0.88	43	86
Si/Al 110	39.95	0.78	51	102

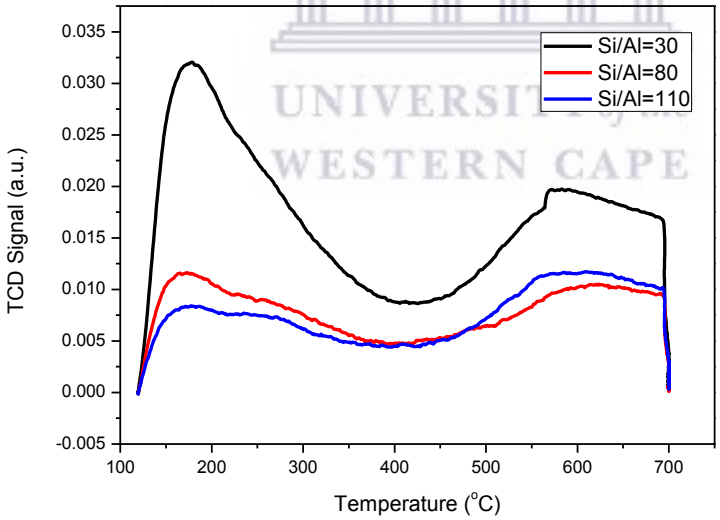

Figure 4. 13: Ammonia-TPD patterns of Al-MCM-41 with different Si/Al ratios.

Ammonia-TPD pattern shown above are that of synthesised Al-MCM-41 materials showing the presence of mild acidity known as Brönsted acid sites, which appear at 250 to 310 °C [77, 78]. Strong acid site known as Lewis acid sites also appeared at approximately 600 °C as seen

in the figure above. Si/Al ratio of 30 catalysts contains higher number of acid sites which was expected since it contains higher amount of metal. Si/Al ratio of 30 showed higher number of acid sites most of which are Brönsted acid site. The acidity of these material decreases as the amount of aluminium incorporated decreases. The Si/Al ratio of 110 and 80 had almost equal number of strong acid sites and weak acid sites. A decrease in desorption temperature for Si/Al ratio of 80 compared to ratio 30 indicates a weak Brönsted acid sites [79].

Table 4. 5: Acidity of Al-MCM-41 samples measured by ammonia-TPD

Sample code	Brönsted acids(200-400 °C)	Lewis acid (400-700 °C)	Total acidity (mmol/g)
Si/Al 30	0.519 (177 °C)	0.239(591 °C)	0.758
Si/Al 80	0.186 (166°C)	0.132 (627 °C)	0.318
Si/Al 110	0.124 (168 °C)	0.149 (623 °C)	0.273

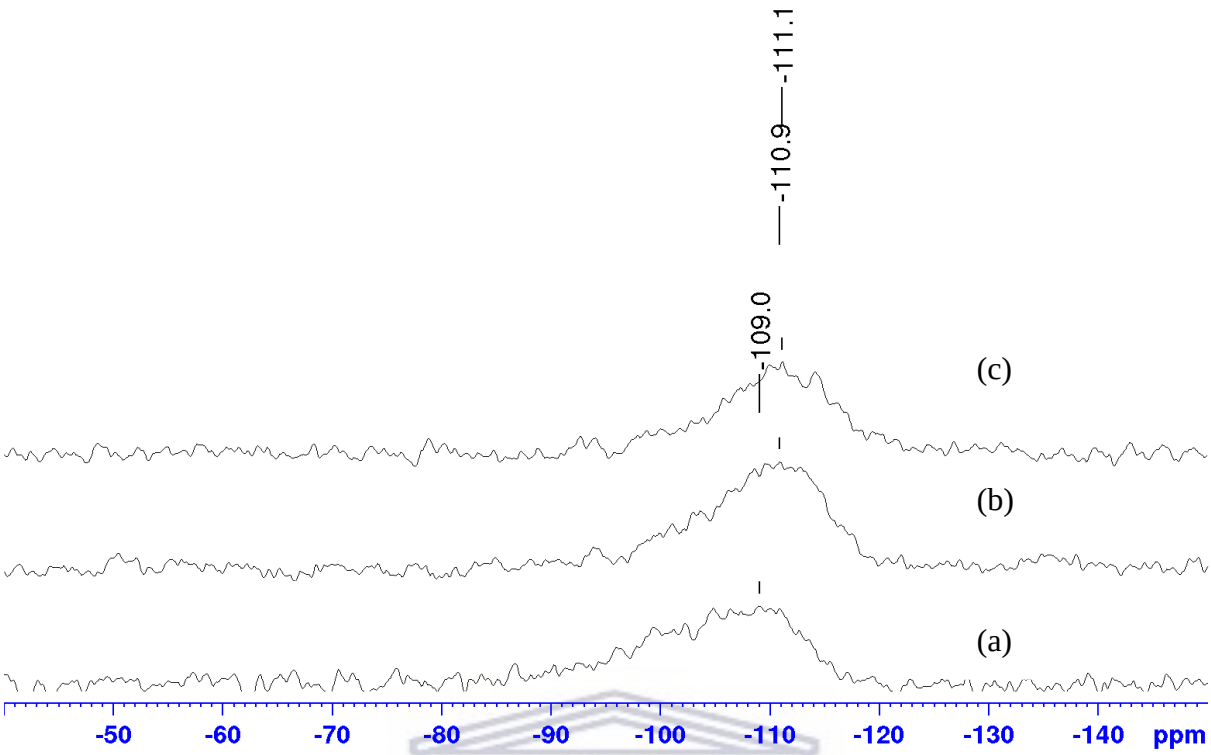

Figure 4. 14: ^{29}Si NMR spectra of Al-MCM-41 with Si/Al ratios (a) 30, (b) 80, (c) 110.

^{29}Si NMR spectra shows a broad signal at -110 ppm which is known to be for silicon not bound to aluminium ($Si(OSi)_4$). The shoulders at -100 ppm which make these peaks broader are due to aluminium substituted silicon ($Si(OSi)_3$ OH) and -90 ppm is assigned to $Si(OSi)_2$ $(OH)_2$. Aluminium substitution results in the shift of these peaks to lower field by 5 ppm for each substituted aluminium. Due to large number of Al-O-Si angles in MCM-41 species, therefore shift for each aluminium substituted is impossible to observe [70, 80, 81].

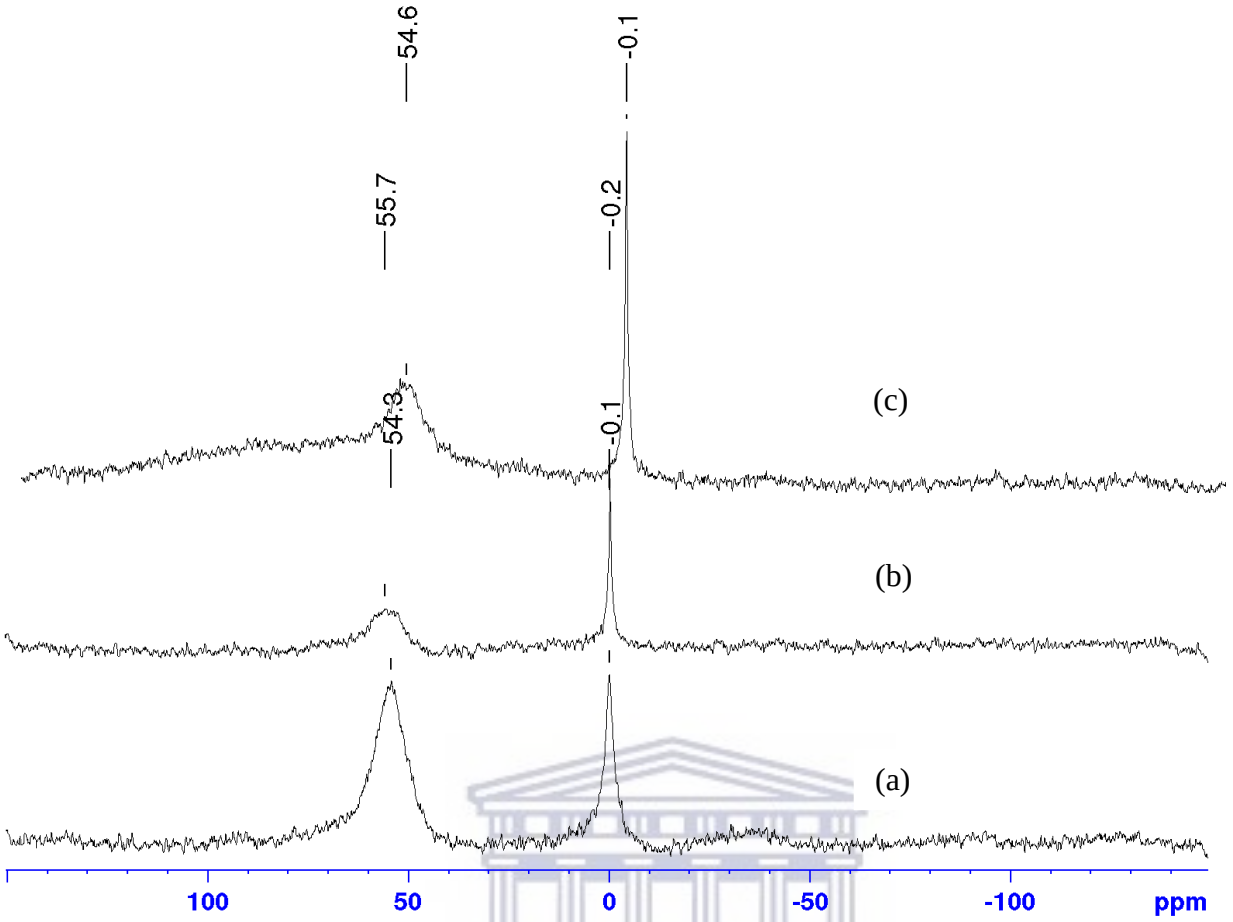

Figure 4. 15: ^{27}Al **NMR spectra of Al-MCM-41 with different Si/Al ratios (a) 30, (b) 80, (c) 110.**

The solid state ^{27}Al NMR above shows peaks at around 54 ppm and another one at 0ppm. The peak at 54 ppm is broader than previously reported [82]. The signal at 54 ppm is assigned to tetrahedral coordinated framework aluminium (T_d-Al) and that at 0 ppm to octahedral coordination non-framework aluminium [80, 82, 83]. Spectrum (a) show more intensity on a peak at 54 ppm and it is believed to be influenced by the synthesis pH. Presence of tetrahedral aluminium is proportional to Brönsted acid site while octahedral aluminium is proportional to Lewis acid sites [82, 84]. The intensity of peaks for (a) is almost the same which mean equal amount of acid sites should be obtained which is not the case when looking at Figure 4.13. Spectra (b) and (c) above have lower intensity at 54 ppm peak than at 0 ppm indicating less Brönsted acid sites Lewis acids sites. Even if the Lewis acid sites are higher, though NH_3-TPD show that they are just 0.02 mmol apart.

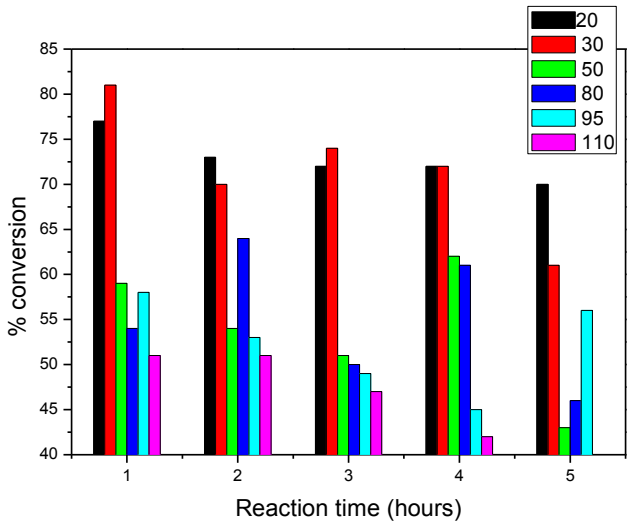

Figure 4. 16: Conversion of 1-hexene to liquid product over different ratio of silica to Al-MCM-41 mesoporous catalyst on a quartz fixed bed reactor at 350 °C.

Incorporation of aluminium in MCM-41 creates the acid sites in the catalyst which was tested in the conversion of 1-hexene. During 1-hexene oligomerisation reaction, products were sampled hourly and a calculated conversion is displayed in Figure 4.16 against time. Si/Al ratios of 20 and 30 maintain higher conversion throughout the reaction time of 5 hours compared to other synthesised catalyst. For the first four hours their conversion ranges between 71 to 82% with a decrease as time increases. Catalysts with Si/Al ratios of 50 to 95 showed an uneven trend which the percent conversion depended on the hour. The trend from this catalyst behavior could not be concluded. Si/Al ratio of 110 catalysts displayed a decrease on the 1-hexene conversion which shows deactivation of the catalyst with low aluminium content.

The adjustment of catalyst properties affects its activity towards resulting in selectivity to the certain reaction over the others. Figure 4.17 below shows the selectivity of the catalyst to the converted product. Mesoporous MCM-41 showed 70% selectivity to C_6 hydrocarbons group. Looking at Scheme1 in Chapter 1, MCM-41 might be a good isomerisation catalyst hence high selectivity of n-hexene or hydrogenation catalyst. The same behavior was reported in the conversion of phenol and formaldehydes [85]. MCM-41 also shows selectivity towards lower hydrocarbons with selectivity of 30%, 10% and 15% towards C_3, C_4 and C_5 respectively.

Increase in the content of Al did not show any changes in the selectivity except for C_6. Even with incorporation of aluminium, in this case we still observed cracking but with an improvement compared to siliceous MCM-41.

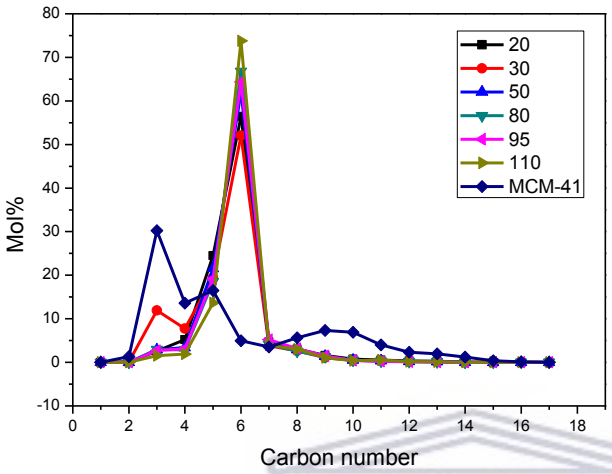

Figure 4. 17: Selectivity of synthesised various Al-MCM-41 in 1-hexene oligomerisation at 350˚C and 1 bar.

Behavior shown by MCM-41 in this case has led to repeating the oligomerisation process of 1-hexene. The product was analysed using DHA chromatograph which shows the mass percentage of each component in the product. Table 4.6 shows that olefins were the main components in the product with 79% C_6 hydrocarbons. From Appendix A it has been discovered that these are hexene isomers and hydrogenated species. About 7.53 mass % of paraffins were also formed during the reaction and 9.33 mass % of possible aromatics or naphtha. The selectivity of the catalyst was towards C_6 carbon number which is identify as the isomers of hexene with the mass % of 83.0. C_7 showed mass % of 4.87 is mostly an iso-paraffins. The C_5 product has the second highest number of olefins formed with mass % of 3.42 which result from catalytic cracking during the reaction.

Studies show that Al-MCM-41 was not active for oligomerisation reaction due to lack of strong acid sites seen in NH_3-TPD, although it has been seen selective for C_{12}- C_{30+}, mostly

dimerasation and trimerisation. The temperature of 100 °C was used in the production C_{12}-C_{30+} which was much lower than 350 °C that was used during this study [120].

Table 4. 6: Liquid fragments of the oligomerisation product in mass % over MCM-41

Carbon number	Paraffins Cyclo	Paraffin iso	Paraffins Normal	Olefins	Others	Total
	0.00	0.00	0.00	0.00	7.98	7.98
C3	0.00	0.00	0.00	0.07	0.00	0.07
C4	0.00	0.00	0.00	0.40	0.00	0.40
C5	0.02	0.00	0.00	3.32	0.08	3.42
C6	0.00	0.02	2.64	79.1	1.27	83.0
C7	0.00	4.63	0.04	0.20	0.00	4.87
C8	0.04	0.00	0.07	0.08	0.00	0.19
C9	0.00	0.04	0.00	0.00	0.00	0.04
C12	0.05	0.00	0.00	0.00	0.00	0.05
Total	**0.10**	**4.69**	**2.74**	**83.14**	**9.33**	**100.0**

4.2. 2 Chromium-modified MCM-41 (Cr-MCM-41)

Table 4.7 below display the external surface area and pore volume of the synthesised material analysed by BET analysis. Material surface area and pore size were characterised by multi-

point adsorption desorption technique to study the changes as different amount of chromium is incorporated in the siliceous surface as well in the pore.

Table 4. 7: Chromium effect on MCM-41 surface area.

MCM-41 catalyst	BET surface (m^2/g)	Ext. surface area (m^2/g)	Pore volume (cm^3/g)	*d*-spacing (Å)[a]	Pore diameter(Å)	Wall thickness(Å)
MCM-41	955	1001	0.920	41.52	37.03	10.91
Si/Cr 30	104	69.5	0.151	36.62	23.18	19.10
Si/Cr 80	157	110	0.189	36.45	19.78	22.31
Si/Cr 110	134	86.9	0.174	36.45	23.16	18.93

[a] the *d*-spacing reported herein was determined from the XRD shown in Fig. 4.20 below

The surface areas obtained by BET analysis shown in Table 4.7 seem not to have a constant pattern with what has been previously reported which states that increase in metal content results in a decrease in surface area as well as pore volume[48]. These values were relatively lower than that reported, with values from 460 to 667 m^2/g depending on the amount of Cr added.

Exterior and interior surfaces of these materials were studied by BET at -196 °C after degassing at 400 °C for 4 hours. Nitrogen adsorption-desorption isotherms and pore size of the synthesised materials were plotted and appear in Figure 4.18 and 4.19, respectively. Pore diameter was measured from zero to 200 Å and zoomed to the region shown below.

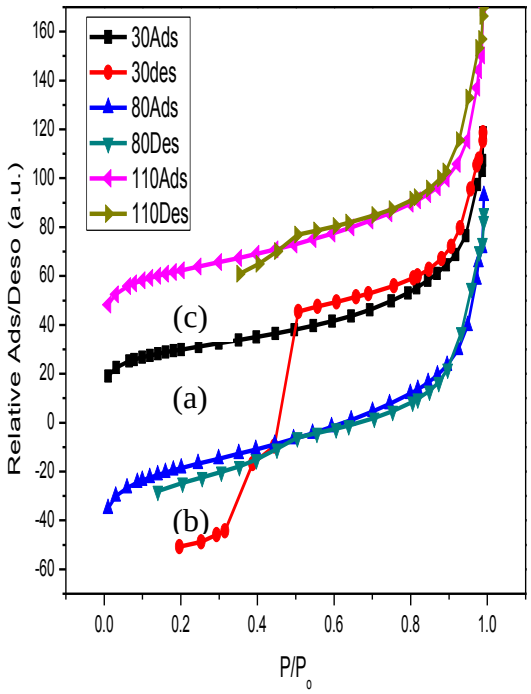

Figure 4.18: N_2-adsorption isotherms for MCM-41 synthesised with Si/Cr ratio of (a) 30, (b) 80 and (c) 110.

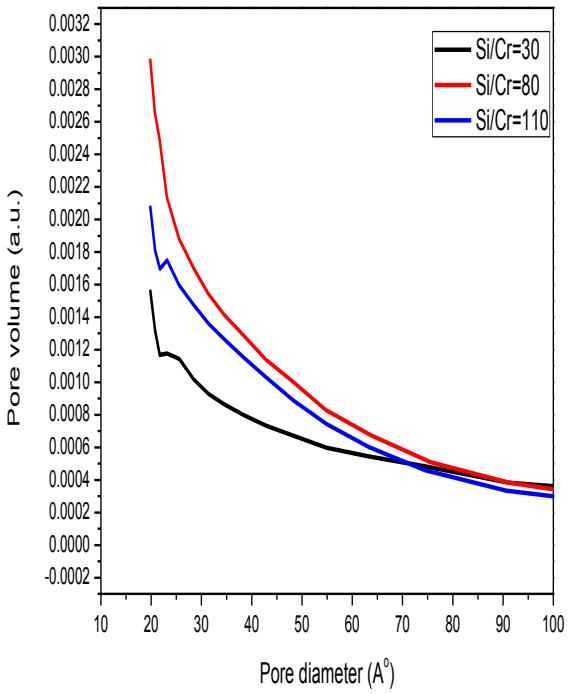

Figure 4.19: Pore volume against pore diameter for MCM-41 synthesised with Si/Cr ratio of 30, 80 and 110.

The plot showed type III isotherms which are a capillary condensation of micropores. Type IV isotherms are associated with hexagonal array of mesopores MCM-41, which here is not the case as SEM analysis showed absence of hexagonal material [23, 86]. The similarities in the isotherms shape of all samples suggest that any amount of metal loaded affects MCM-41 the same way and the pore uniformity is lost as seen in Figure 4.19. Pore size distribution is broad with disappearing of peak at a range of 2.5 nm. Studies had shown that increase in aluminium incorporate results in broader pore size distribution carve and narrowing of pore diameter [82].

XRD pattern in Figure 4.20 display reflection 100 at 2.5° and reflection 110 and 200 at 4.1° and 4.7° respectively [86]. These correspond to hexagonal arrangement of uni-dimensional channels of the MCM-41 structures. The appearance of these refractions after calcination of samples is proof that MCM-41 sample are thermally stable [12, 23]. The intensity of all the reflation peaks was the same in all synthesised materials. This indicates that the crystallinity of these materials was not affected by the amount of chromium hence confirmed by

morphology in SEM analysis. The absence diffraction line corresponding to chromium oxide crystallites suggest that no such species were formed [86].

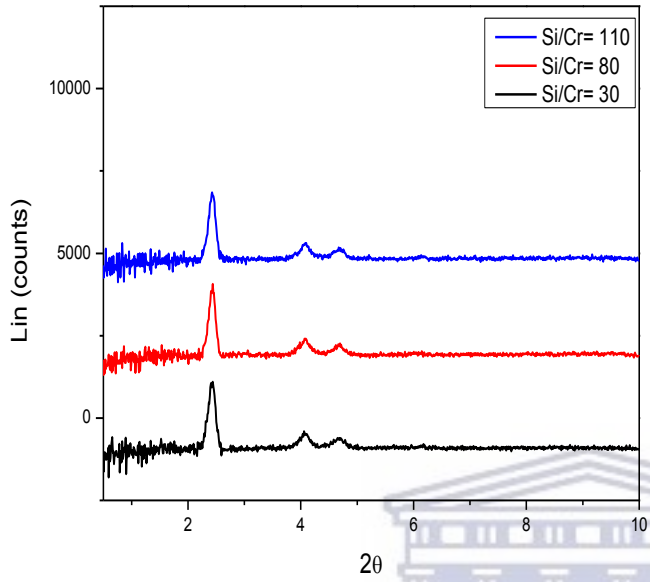

Figure 4. 18: XRD pattern of MCM-41 catalyst synthesised with Si/Cr ratio of (a) 20, (b) 30 and (c) 110.

It was also noted from Table 4.7 that *d*-spacing was the same for Si/Cr ratio of 80 and 110 then increases at Si/Cr ratio of 30 which is a result of increased metal content. The shift of the refractions to the lower angle is due to shrink of hexagonal shape [23].

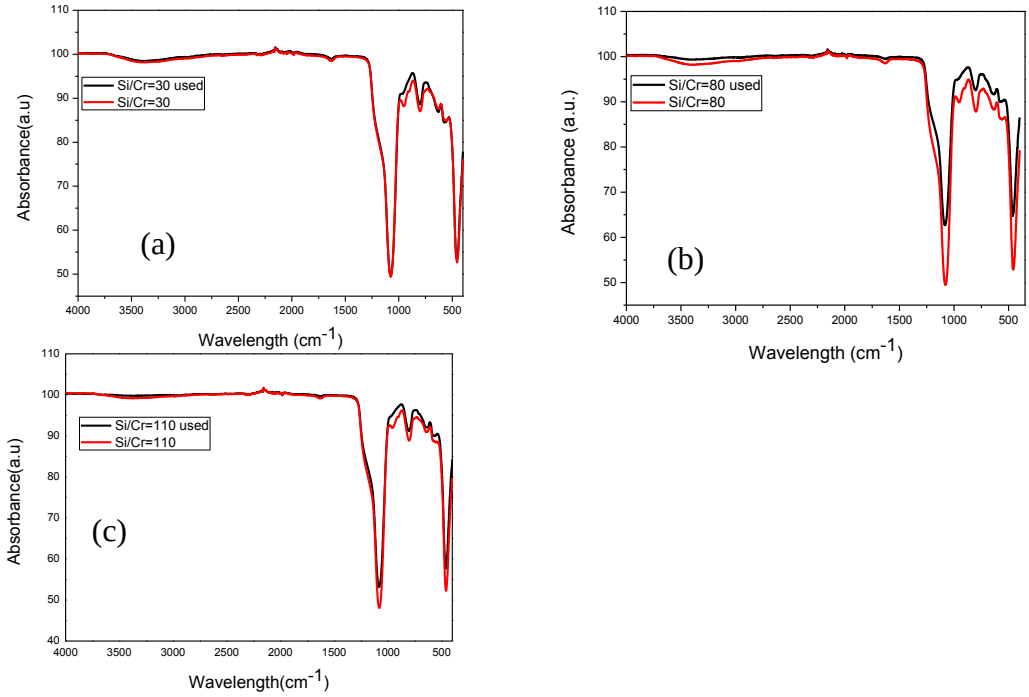

Figure 4. 19: FTIR spectra for MCM-41 synthesised with Si/Cr ratios of (a) 30, (b) 80 and (c) 110 before and after 1-hexene oligomerisation on a quartz fixed bed reactor at 350 °C.

The FTIR spectra illustrated in Figure 4.21 before and after oligomerisation of 1-hexene show no new bands than those obtained for synthesised MCM-41 except for change in the band intensity. Band at 470 cm^{-1} correspond to bending of $Si\text{-}O^{-}$ groups on the surface. While the bands at 810 and 1090 cm^{-1} correspond to symmetric and asymmetric Si-O stretching vibrations [87]. Spherically shaped structure materials were seen by SEM micrograph in Figure 4.22 which is explained by the absence of type IV isotherm shape that is associated with hexagonal array. The similar morphology indicates that the amount of chromium added does not have different effects on the material appearance.

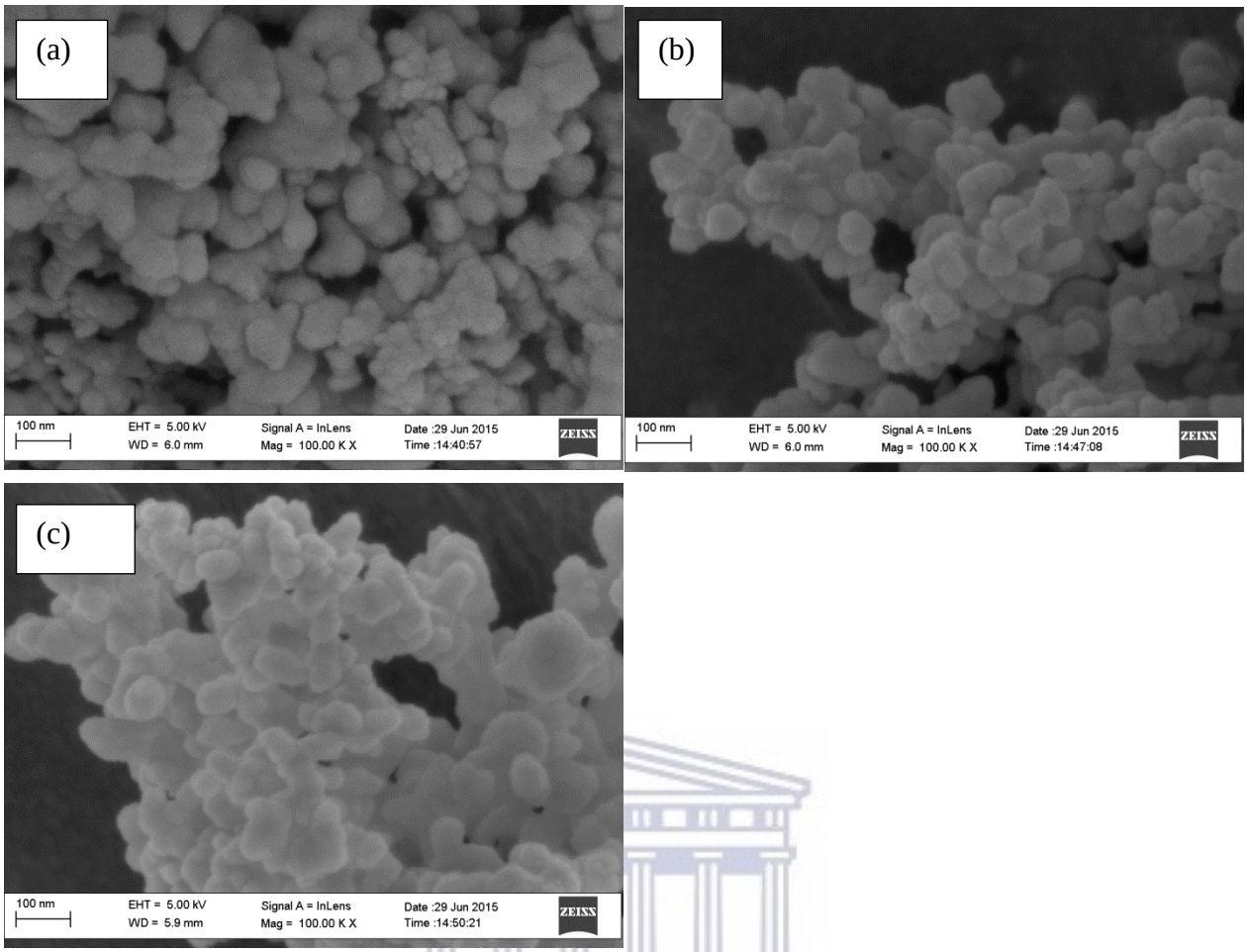

Figure 4. 20: SEM micrographs of the mesoporous MCM-41 synthesised with Si/Cr ratio of (a) 30, (b) 80 and (c) 110.

Material was also tested in 1-hexene reaction for the catalytic activity after their modification of active sites. Even though it seems like different amounts of chromium loading have no different structural surface of the catalyst, the catalytic testing shows a different behavior. It seems like catalysts with a Si/Cr ratio of 30 have higher conversion for the first hour then deactivate as reaction proceeds. The deactivation is not understood as FTIR showed no deposition of hydrocarbons to the catalyst framework. As seen in Figure 4.23 above Si/Cr ratio of 110 showed the same behavior while in Si/Cr ratio of 80 the conversion of 1-hexene increases for 3 hours then it declines again.

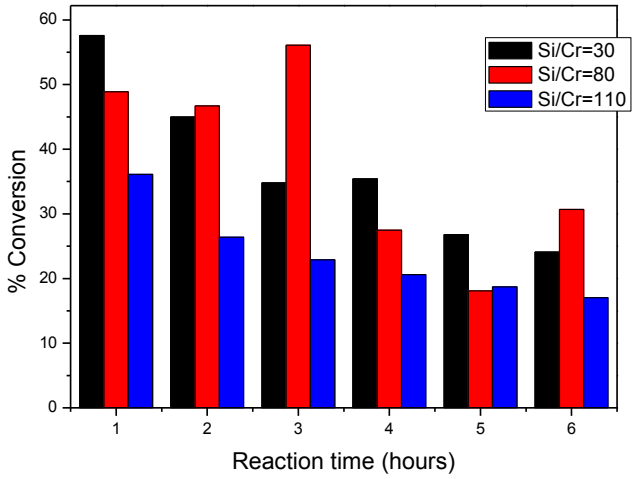

Figure 4. 21: Selectivity of synthesised co-precipitated Cr-MCM-41 for 1-hexene oligomerisation on a quartz fixed bed reactor at 350 °C.

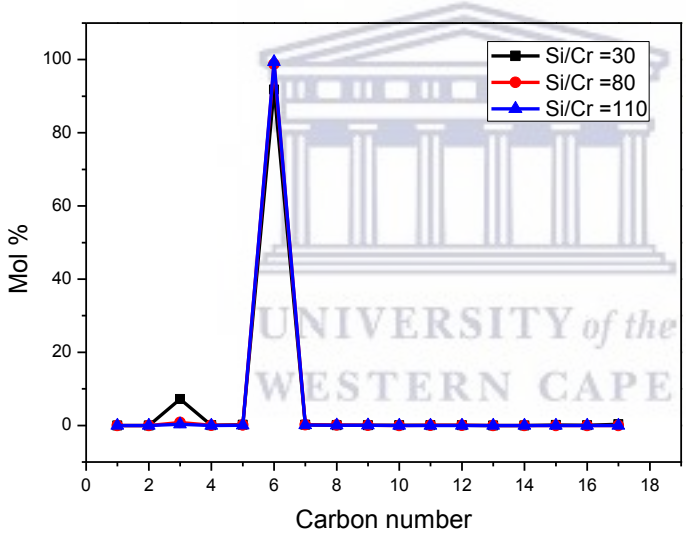

Figure 4. 22: Conversion of 1-hexene to liquid product over chromium-modified MCM-41 mesoporous catalyst of different ratio.

The catalyst showed almost 100% selectivity forwards C_6 hydrocarbons while only Si/Cr ratio of 30 showed about 10% selectivity towards C_3 hydrocarbon which is believed to be in the gas state. Increase in chromium content in a support material increases the activity of the catalyst [88]. It has been observed in this study that chromium increase does not bring any changes to the selectivity of product hydrocarbons.

4.2. 3 Iron-modified MCM-41

MCM-41 was modified by introduction of iron to its framework structure. The effect induced by metal addition was studied with BET analysis. Table 4.8 below shows changes on the surface areas as well as pore sizes and wall thickness

Table 4. 8: Iron effect on synthesised MCM-41 surface area.

MCM-41 catalyst	**BET surface (m^2/g)**	**Ext. surface area (m^2/g)**	**Pore volume (cm^3/g)**	***d*-spacing (Å)[a]**	**Pore diameter(Å)**	**Wall thickness(Å)**
MCM-41	955	1001	0.920	41.52	37.03	10.91
Si/Fe30	241	232	1.025	36.79	28.90	13.58
Si/Fe 80	154	110	0.188	36.12	19.78	21.93
Si/Fe 110	218	274	0.323	36.29	24.80	17.10

[a] the *d*-spacing reported herein was determined from the XRD shown in Fig. 4.27 below

Nitrogen adsorption isotherms and pore volume as well as pore size distribution are known as the most crucial parameters for porous material and shape-selectivity catalyst. Pore size and active site shape determines the contact between the active site and the reactant. The exit of product is also determined by pore opening for it to leave undistracted. Figure 4.25 and Figure 4.26 shows the obstruction caused by metal incorporation on the pores of these siliceous materials.

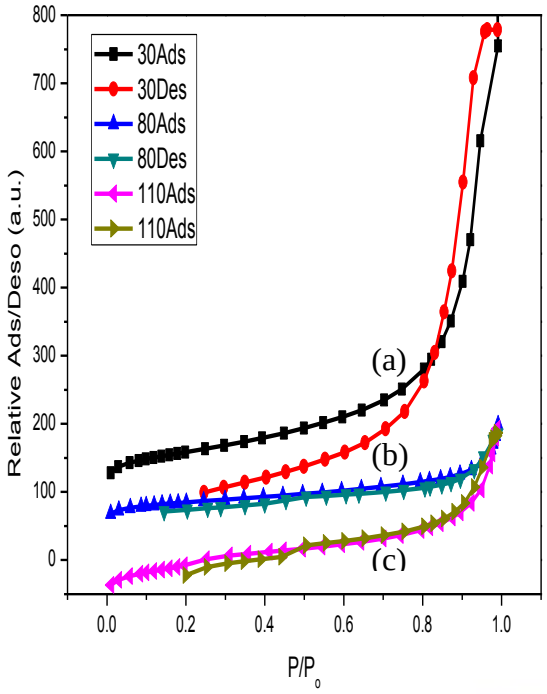

Figure 4. 23: N_2-adsorption isotherms for MCM-41 synthesised with Si/Fe ratios of (a) 30, (b) 80 and (c) 110.

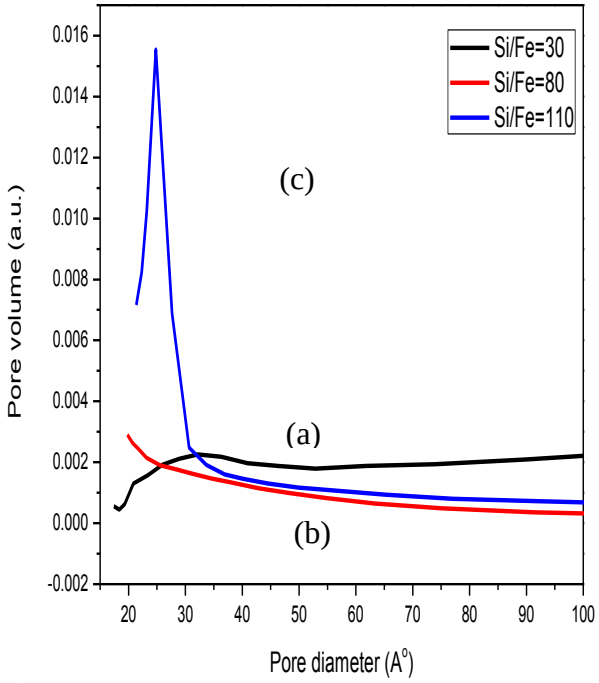

Figure 4. 24 : Pore volume against pore diameter for MCM-41 synthesised with Si/Fe ratios of (a) 30, (b) 80 and (c) 110.

The recorded values in Table 4.8 are lower than what was obtained previously during modification of MCM-41 with iron [89]. The nitrogen adsorption isotherm showed a type III isotherm which indicates the presence of micropores. The samples BJH adsorption pore sizes were within the range 2.4-2.6 nm reported. The content of TEOS in the initial gel also contributes to the pore reduction due to production of ethanol from it condensation [74].

The XRD pattern in Figure 4.27 proves that synthesised samples have hexagonal mesophase due to the intensity of reflection (100). Though samples show known peaks at reflection (100), (110) and (200), sample ratio Si/Fe of 110 showed another peak at an angle 1.9° which has not been reported before. Conclusion was this is perhaps due to sample impurities. The reduction in peak intensity with the long-range hexagonal arrays of mesopores being sustained [90]. This was not the case in the synthesised sample as the intensity of peaks has been reduced after metal loading and as metal loading increases.

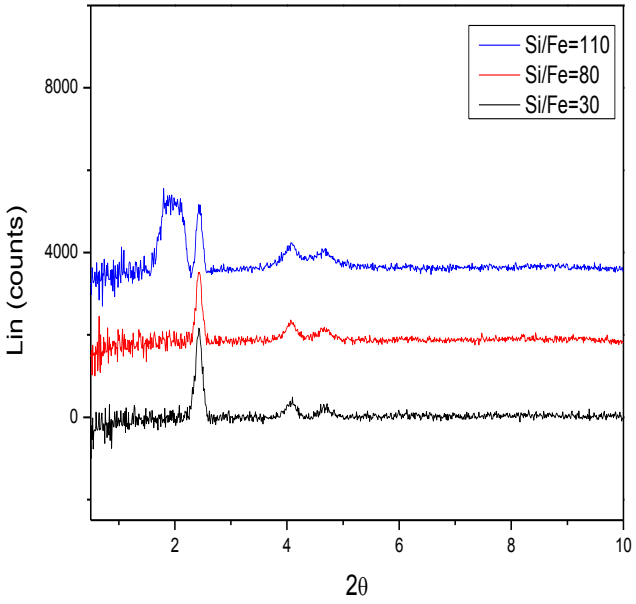

Figure 4. 25: XRD pattern of MCM-41 catalyst synthesised with Si/Fe ratios of 20, 30 and 110.

In Figure 4.28 below the FTIR of the samples before and after oligomerisation were compared and displayed on the same axis.

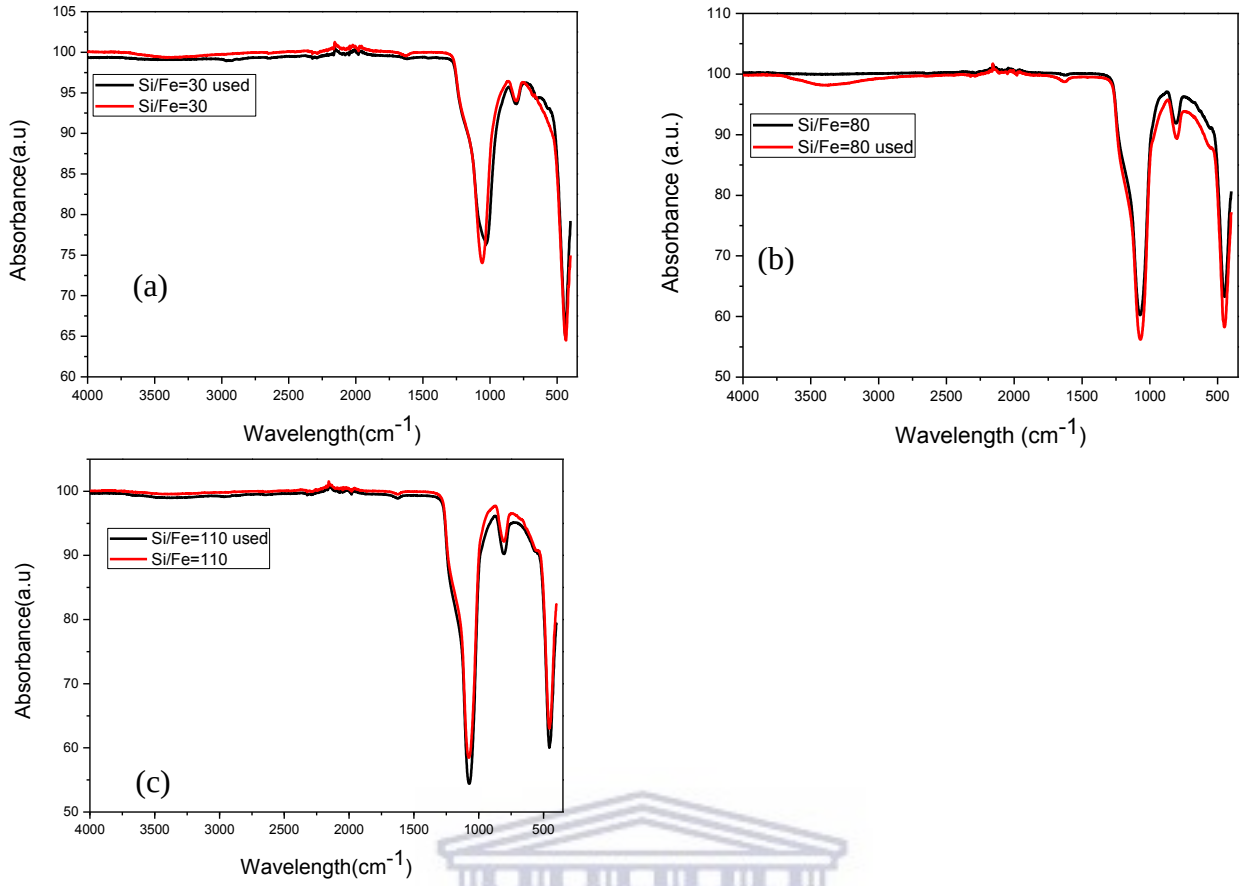

Figure 4. 26: FTIR spectra for MCM-41 synthesised with Si/Fe ratios of (a) 30, (b) 80 and (c) 110 before and after 1-hexene oligomerisation on a quartz fixed bed reactor at 350 °C.

The plot above showed bands at a range of 450 to 1600cm^{-1} which were witnessed previously when MCM-41 was modified by tungsten (W) [84]. Upon modification of MCM-41 with Al FTIR with peak at wavenumber 1350 to 1750 cm^{-1} was associated with the adsorption of Brönsted acid site (1545 cm^{-1}), and both the acid site and Brönsted at a wavenumber 1493 cm^{-1} [91]. This is not understood if the data obtained was pushed down the wavenumber due to iron introduction or the nature of iron source.

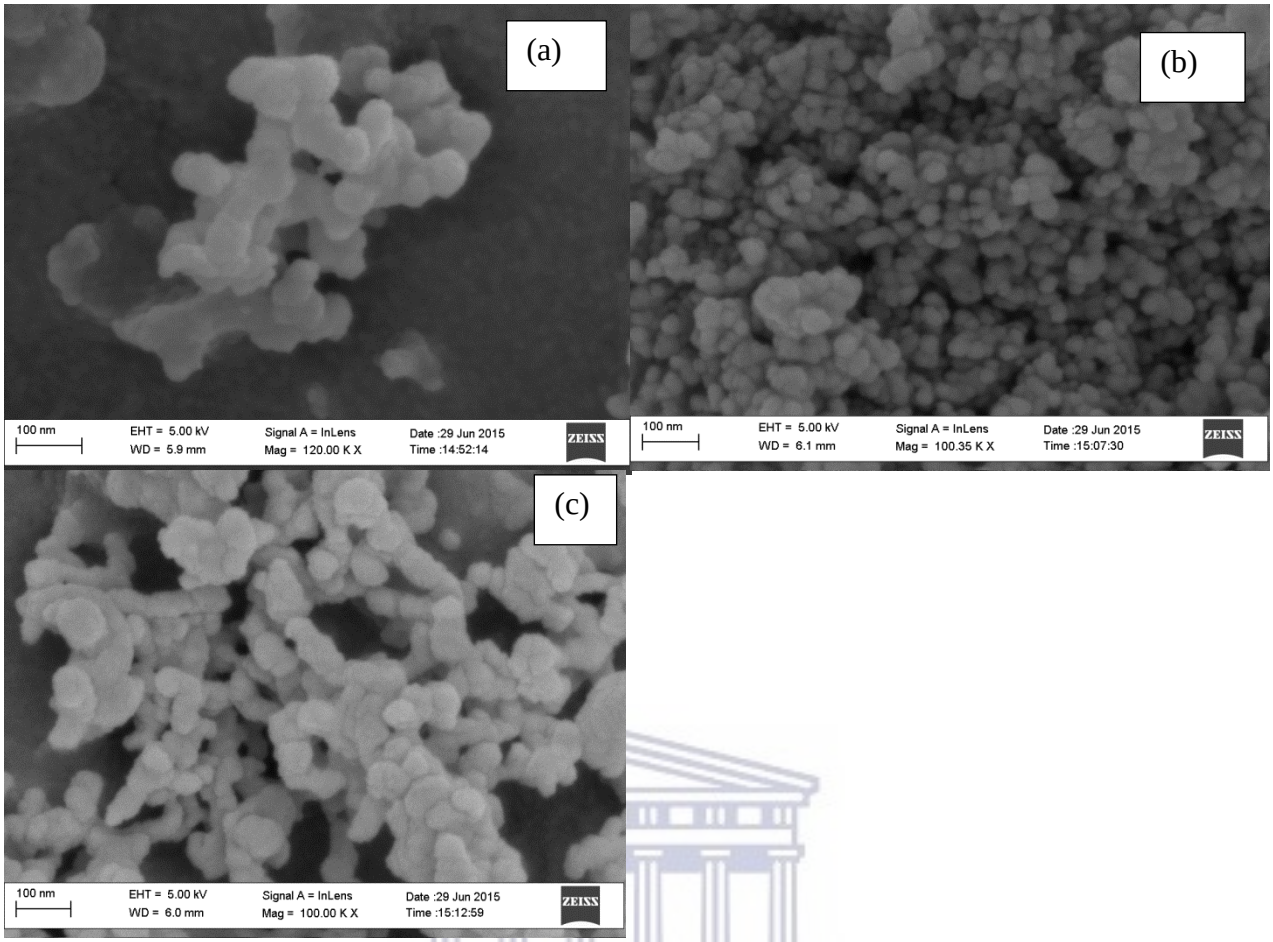

Figure 4. 27: SEM micrographs of the mesoporous MCM-41 synthesised with Si/Fe ratios of (a) 30, (b) 80 and (c) 110.

SEM micrographs for iron modified samples do not have a constant shape as spherical and tubular shapes were seen. This is constant with what has been reported for incorporation of hetero-atom in mesoporous materials [91]. Due to the mingling of these species the identification of their size could not be clearly determined. Conclusion could not be made on what shape they are, or what condition it forms spherical or tubule.

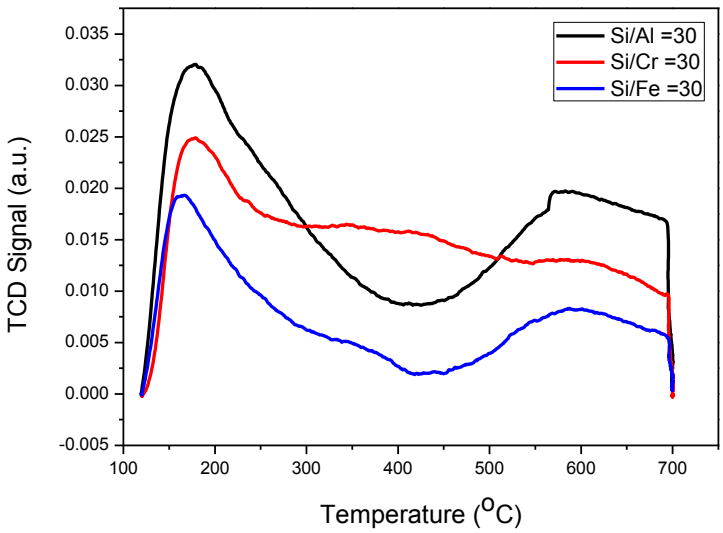

Figure 4. 28: Ammonia-TPD patterns of metal modified MCM-41.

Table 4. 9: Acidity of metal modified MCM-41 samples measured by ammonia-TPD

Sample code	Brönsted acids (200-400 °C)	Lewis acid (400-700 °C)	Total acidity (mmol/g)
Si/Al 30	0.519 (177 °C)	0.239 (591°C)	0.758
Si/Cr 30	0.334 (170 °C)	0.089 (625 °C)	0.423
Si/Fe 30	0.329 (166 °C)	0.116 (587 °C)	0.445

Acid sites were obtained by ammonia-TPD at a temperature range from 100 °C to 700 °C. Figure 4.30 above shows that the synthesised material contains both Brönsted and Lewis acid sites. The concentrations of acid sites as well as the reduction temperature of the species are shown in table 4.9 above. Aluminium catalysts have higher acid sites followed by chromium catalyst then iron catalyst. Chromium catalyst also shows mild acids site around 400 °C indicated by the hump, even though their concentrations were not calculated. The shift to higher temperature for different species is the evidence for stronger interaction between the

metal and the support [92, 93]. Reduction temperatures seen above are also smaller than those reported for Si/Cr ratio of 40 at 373 °C and 520 °C and just one peak for Si/Cr ratio of 20 °C at 520 °C.

Testing of synthesised materials on oligomerisation of 1-hexene on the fixed bed reactor made of quarts, resulted in liquid product that was analysed by gas chromatography. The effect of time on the conversion of product is shown on Figure 4.31 while the selectivity of these materials is shown in Figure 4.32 below.

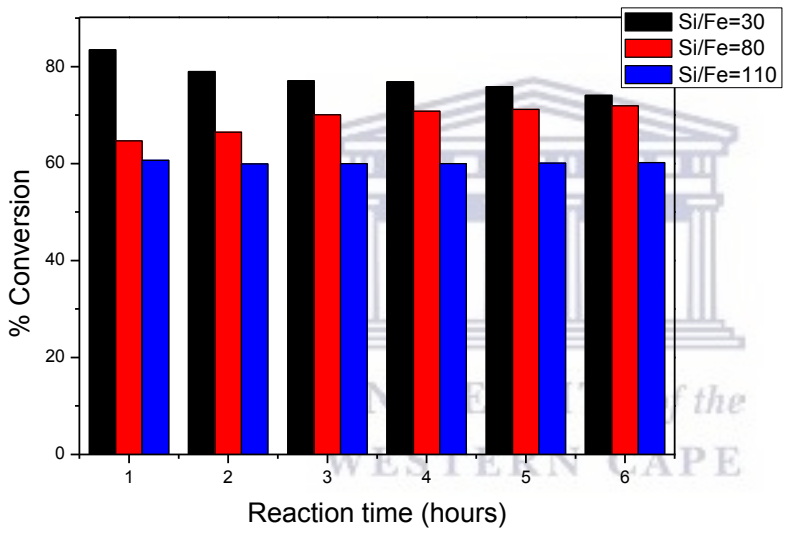

Figure 4. 29: Conversion of 1-hexene to liquid product over different ratios of Fe-MCM-41 mesoporous catalyst on a quartz fixed bed reactor at 350 °C.

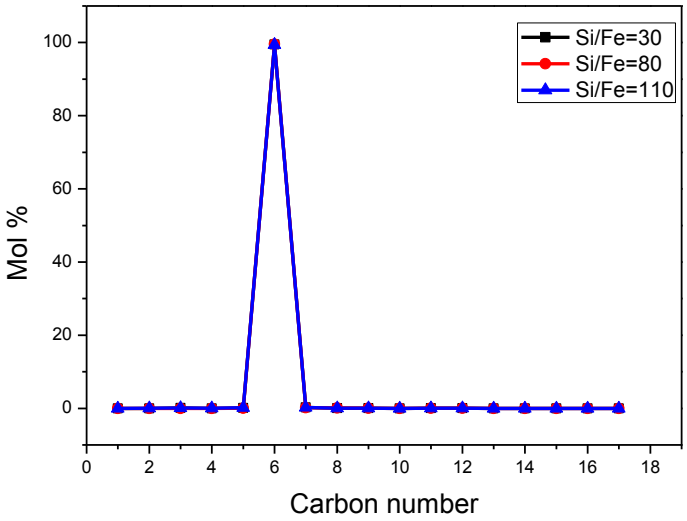

Figure 4. 30: Selectivity of synthesised co-precipitated Fe-MCM-41 for 1-hexene oligomerisation on a quartz fixed bed reactor at 350 °C.

The plots showed that iron modified MCM-41 has higher catalytic activity than pure silica-MCM-41. The higher amount of iron incorporated results to higher conversion of 1-hexene to liquid product as it is seen that Si/Fe ratio of 30 had a conversion ranging between 75% and 84%. The Si/Fe ratio of 110 showed a constant conversion for the duration of the reaction which was about 60%. While Si/Fe ratio of 80 shows a slight increase in conversion every hour. Even though the conversion of 1-hexene looks promising these catalysts were still 98% selective to C_6 hydrocarbons with no trace of longer chains hydrocarbons nor shorter chains. Even though 3% Fe-MCM-41 catalyst show 0.445 mmol/g of acid sites, these not strong enough to form longer chain olefins. At higher pressure the fate of these catalysts can be changed.

4. 3 Conclusion

Synthesis of MCM-41 containing metal (Al, Fe, Cr) in their framework structure were successful with crystallisation time of 72 hours. Although temperature studies showed that mesoporous MCM-41 is obtained at 100 °C at the presence of metal, crystallisation could not be obtained at such temperature. Therefore, all synthesis of metal doped MCM-41 materials was conducted at 150 °C. In the production of meta-MCM-41 the surface area as well as pore

volume decreases due to deposition of metal. Nitrogen adoption isotherm showed a type III isotherm indicating the decrease in mesopores and an introduction of micropores hence the decrease in pore diameter as well as pore volume.

Synthesis of Al-MCM-41 using sodium silica as silica source surface showed a decrease in pore diameter as the Si/Al ratio increases. Reflections on XRD pattern were poor implying the disruption of hexagonal framework of MCM-41 with lower crystallinity. This is due to coordination of aluminium to form either tetrahedral or octahedral bonding. Morphologically a spherical shaped structure has been obtained but with not much difference from what has been observed in chapter 3 with the absence of metal. Upon testing of the catalyst the higher ratio of silica to metals showed higher conversion of 1-hexene with higher selectivity towards C_6 hydrocarbons. In the synthesis of Al-MCM-41 using TEOS as silica source XRD pattern showed higher crystallinity as Si/Al ratio decrease. As such information has not been seen during literature review during this study it is safe to repeat the synthesis for future purposes. Lower Si/Al ratio catalyst showed higher conversion of up to 82% with selectivity towards C_6 hydrocarbons.

Cr-MCM-41 and Fe-MCM-41 XRD pattern showed three reflection peaks known for highly ordered mesoporous MCM-41. Looking at the atomic radius of these elements it can be concluded that deposition of lower radius aluminium affects MCM-41 framework structure than larger chromium and iron as higher number of Al ions are deposited to the pores. Hence spherical shapes of the materials remain the same upon introduction of both metals. Cr-MCM-41 showed lower conversion compared to Fe-MCM-41 and both with higher selectivity toward C_6 hydrocarbons. The conclusion is that synthesised materials are active in isomerisation reaction of 1-hexene than oligomerisation.

CHAPTER 5: Impregnation of MCM-41 with metal precursors

5. 1 Brief introduction

Catalyst synthesis is considered as a work of art as it can be prepared in a number of different methods. In the synthesis of these materials it is also necessary to utilize at a modern level all achievements of physical and colloid chemistry, mechanics of media as well as the solid-state physics. Different theories results in successful analysis for physicochemical processes of catalyst synthesis [94, 95]. Impregnation is a common method for preparation of supported base metals by dipping the porous support into a solution of suitable catalytic agent. Even though the penetration of the liquid into the porous support is hindered by trapped air, calcination removes the liquid in the pores exit resulting in catalytic porous material with active external surface [96]. In this chapter the effect of metal impregnation on mesoporous MCM-41 is studied and the catalyst behavior compared to co-precipitated metal doped MCM-41.

5. 2 Results and discussion

5.2. 1 Aluminium modified MCM-41

Surface changes of MCM-41 after incorporating different amounts of aluminium in the frame structure, using the impregnation route were studied using BET. This allows the determination of material surface area and pore size at multi-point adsorption desorption. The rest of the obtained data is shown in the table below.

Table 5. 1: Surface properties of MCM-41 impregnated with aluminium.

MCM-41 catalyst	BET surface (m^2/g)	Ext. surface area (m^2/g)	Pore volume (cm^3/g)	*d*-spacing (Å)[a]	Pore diameter(Å)	Wall thickness (Å)
1% Al-MCM-41	41	38	0.101	35.62	19.80	21.33
3% Al-MCM-41	32	28	0.076	38.18	23.82	20.27
5% Al-MCM-41	45	38	0.100	36.62	23.20	19.08

[a] the *d*-spacing reported herein was determined from the XRD shown in Fig. 5.3 below

Nitrogen adsorption-desorption isotherms and pore size data were plotted and displayed in Figure 5.1 and Figure 5.2 respectively. The rise in isotherm at high aluminium content samples is associated with condensation of nitrogen in the voids formed by crystal aggregation while the deviation to this sharp increase is associated with wider pore size distribution [72]. The obtained isotherms show the presence of mesoporous materials as well as microporous materials. The BJH plots show a pore diameter at 1.9 and 2.8 nm for 3%Al-MCM-41 as well as two peaks for 5% Al-MCM-41 around 2.0 to 2.6 nm. The effect of metal doping on the surface area of MCM-41 is shown in Table 5.1. It has been reported that introduction of Al decreases the quality of pore structure [73].

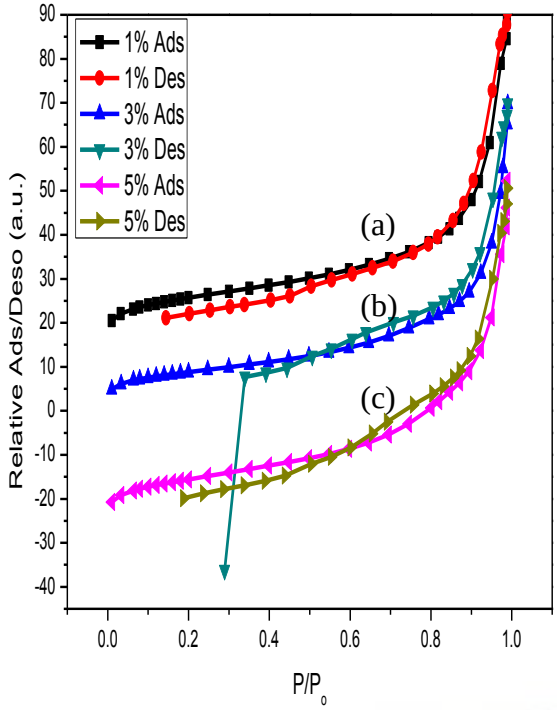

Figure 5.1: N_2-adsorption isotherms of Al-impregnated MCM-41 at weight loadings of (a) 1%, (b) 3% and (c) 5%.

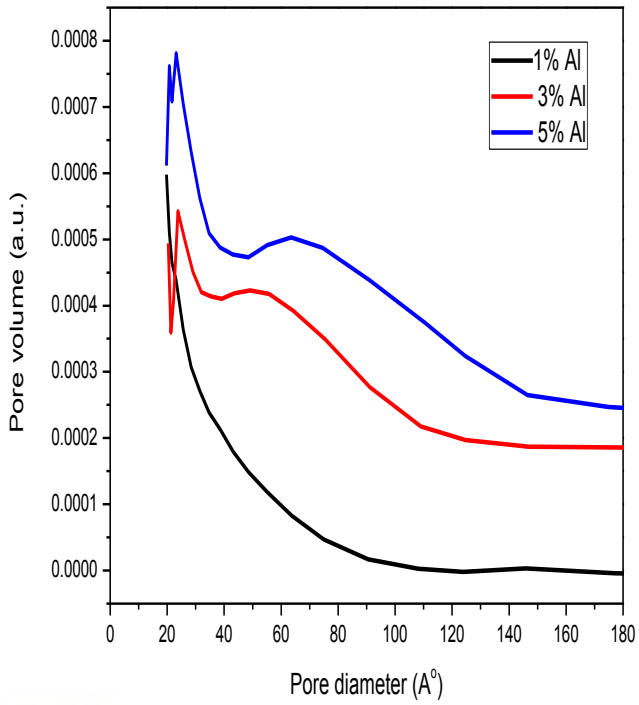

Figure 5.2: BJH plots of Al impregnated MCM-41 at weight loadings of (a) 1%, (b) 3% and (c) 5%.

X-ray diffraction patterns of powder materials were obtained at a region 1.0 to 10° and displayed in Figure 5.3. Low aluminium content materials showed higher degree of crystallinity which decreases as the aluminium increases.

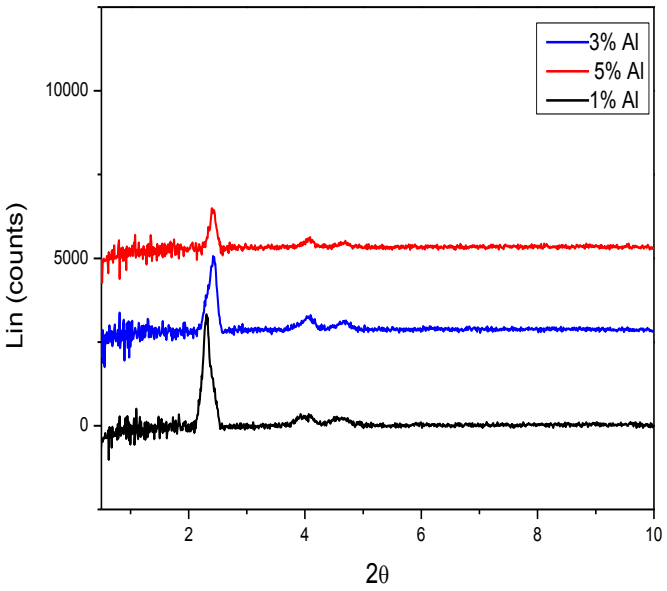

Figure 5. 1: XRD pattern of Al -MCM-41 at weight loadings of (a) 1%, (b) 3% and (c) 5%.

The appearance of the reflection at 2θ angle ranges at 1.9° to 4.8° indicating highly mesoporous materials with hexagonal symmetry. Refraction peak (100) shifts to the lower angle as the amount of aluminium incorporated increases with a decrease in the intensity and increase in *d*-spacing [97]. The alumina-silicate sample displayed that hexagonal order of MCM-41 was maintained except for the broadening of peaks and decrease in the intensity as the aluminium content increases [22, 98].

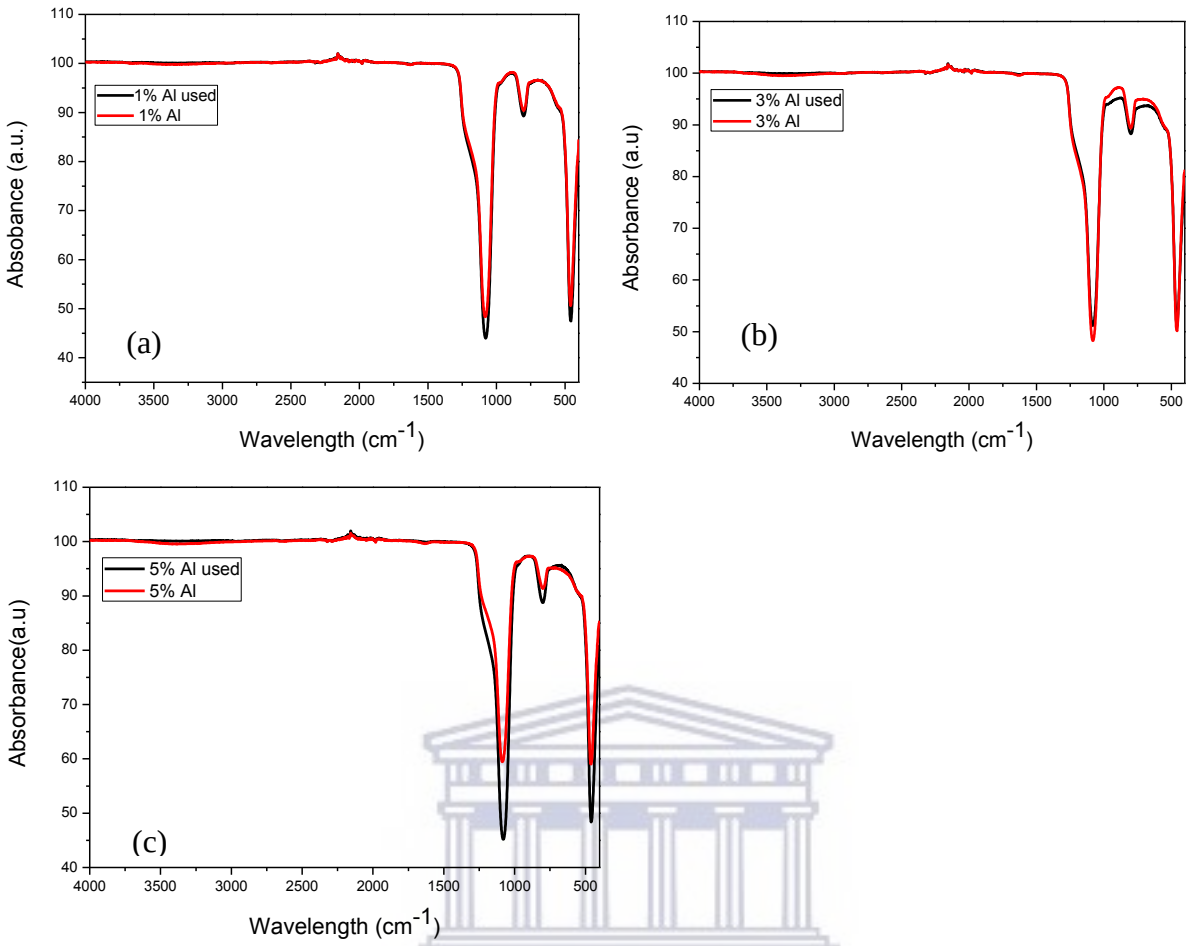

Figure 5. 2: FTIR spectra of Al-impregnated MCM-41 at weight loadings of (a) 1%, (b) 3% and (c) 5%.

The FTIR spectra are shown in Figure 5.4 and all bands seen in synthesised MCM-41 are obtained. Hydroxyl groups in the octahedral coordinated Al atoms are associated with band at 3660 cm^{-1} which was barely present in these samples [23]. The bands were not affected even after oligomerisation of 1-hexene which is different from what was seen when aluminium was co-precipitated in the gel. Impregnated samples show no indication of hydrocarbons deposition while in the co-precipitated sample a new band was observed.

MCM-41 materials are known to be hexagonal in shape which is what has made it a popular material in catalysis. The morphology of the synthesised materials is shown in Figure 5.5 below containing different amounts of aluminium.

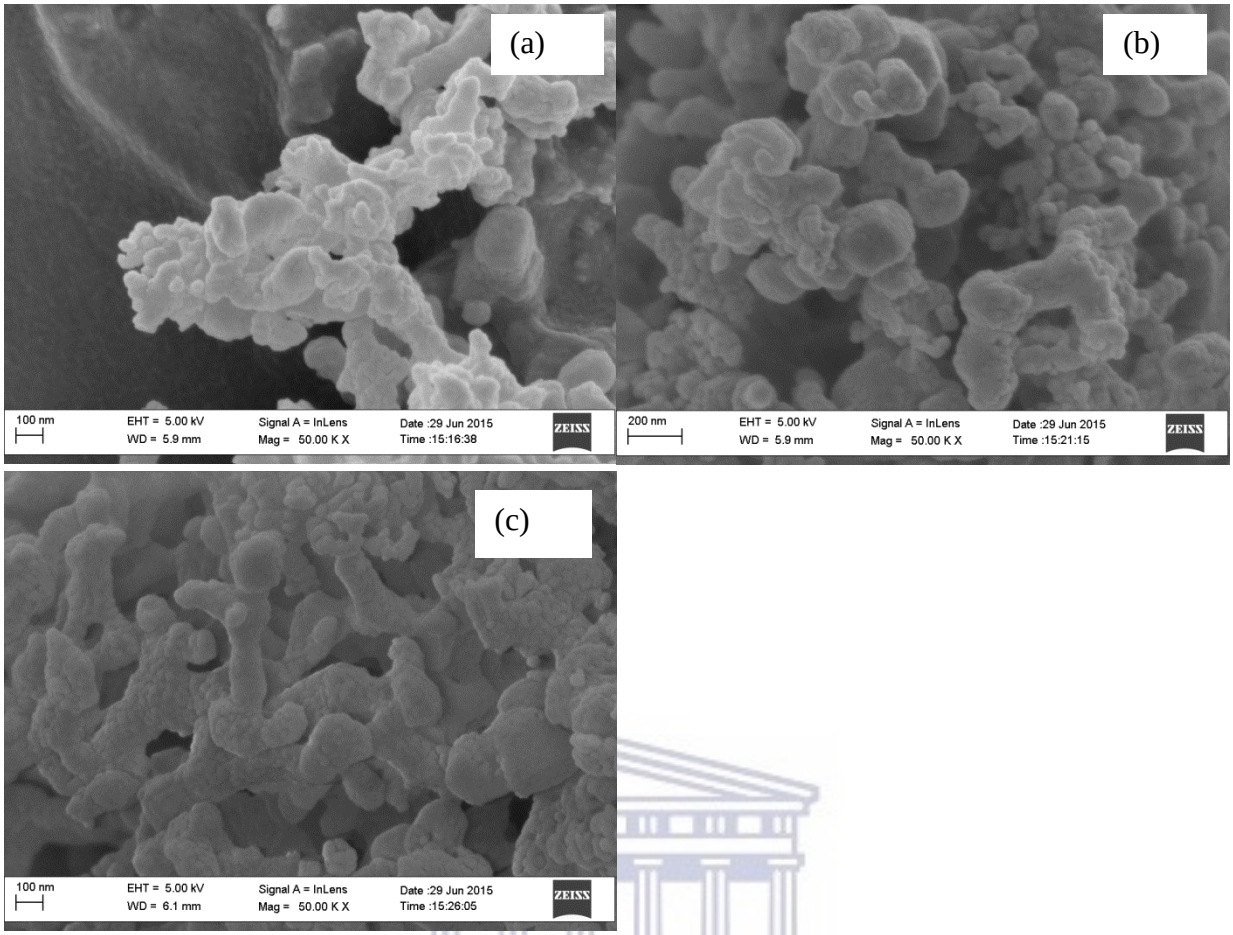

Figure 5. 3: SEM micrographs of synthesised Al-MCM-41 at weight loadings of (a) 1%, (b) 3% and (c) 5%.

SEM micrographs displayed spherical shaped structures as well as tubular shaped structures which are the results of inhomogeneous aluminium distribution [99]. The appearances of tubular shapes on these materials are consistent with mesopores not parallel to each other, indicated by reflection (100) [121].

1-Hexene was used as feed in the oligomerisation reaction to form higher liquid hydrocarbons. Like most zeolitic catalysts, these materials were able to transform 1-hexene to predominantly internal isomers. This suggests that these materials are good isomerisation catalysts. Figure 5.6 and Figure 5.7 show the conversion and selectivity of these catalysts in 1-hexene transformation, respectively.

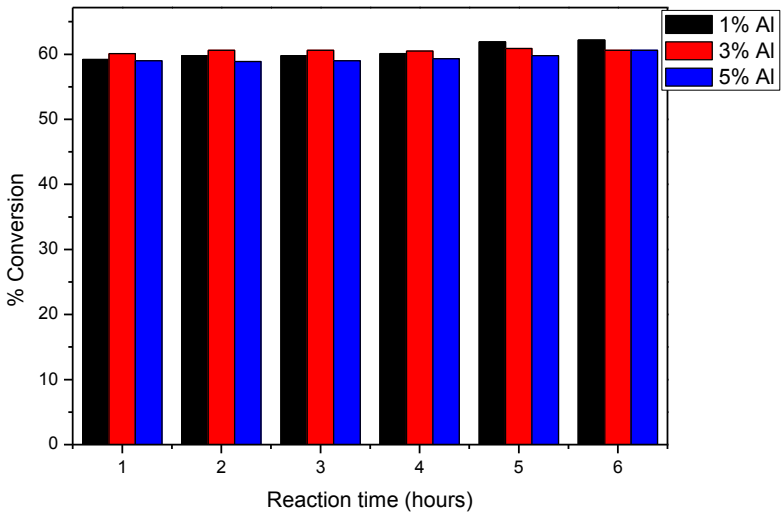

Figure 5. 4: Conversion of 1-hexene to liquid hydrocarbons over Al-impregnated MCM-41 at weight loadings of (a) 1%, (b) 3% and (c) 5%.

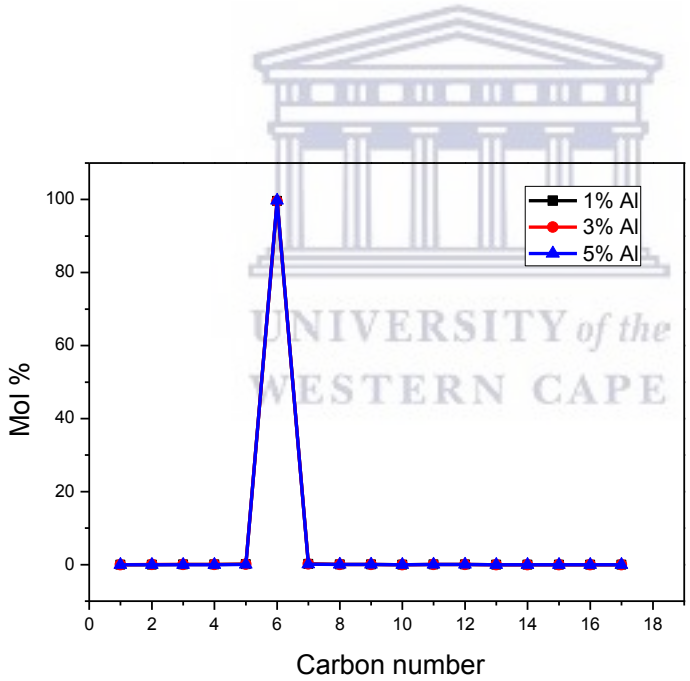

Figure 5. 5: Selectivity Al-impregnated MCM-41 at weight loadings of (a) 1%, (b) 3% and (c) 5% for the conversion 1-hexene on the fixed bed quartz reactor at 350°C .

Conversion reaction of 1-hexene showed almost the same conversion around 80% for all synthesised materials. Their selectivity was around 99% for C_6 hydrocarbons in all the synthesised aluminium containing MCM-41.

5.2. 2 Chromium-modified MCM-41

Heterogeneous chromium supported on silica gel catalyst has been widely used in the production of polyethylene. But what makes this an active catalyst is the formation of chromate ester bound to silica surface [100]. To study chromium association of the silica surface, BET technique was considered for the determination of surface area and pore sizes changes. The data obtained was tabulate in Table 5.2 below.

Table 5. 2: Properties of MCM-41 as it is modified with chromium in the absence of aluminium.

MCM-41 catalyst	BET surface (m^2/g)	Ext. surface area (m^2/g)	Pore volume (cm^3/g)	*d*-spacing (Å)[a]	Pore diameter (Å)	Wall thickness (Å)
1% Cr-MCM-41	277	335	0.340	44.04	20.78	30.07
3% Cr-MCM-41	50.4	42.7	0.118	39.26	23.17	22.16
5% Cr-MCM-41	45.7	39.2	0.118	34.41	38.01	1.723

[a] the *d*-spacing reported herein was determined from the XRD shown in Fig. 5.10 below

For further understanding of these material behaviour upon chromium introduction nitrogen adsorption-desorption isotherms and pore size were plotted as shown in Figure 5.8 and Figure 5.9 below, respectively.

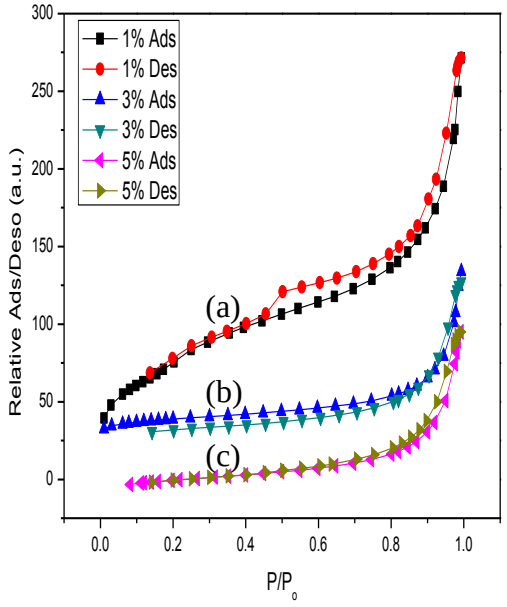

Figure 5. 6: N_2-adsorption isotherms of Cr modified MCM-41 at weight loadings of (a) 1%, (b) 3% and (c) 5%.

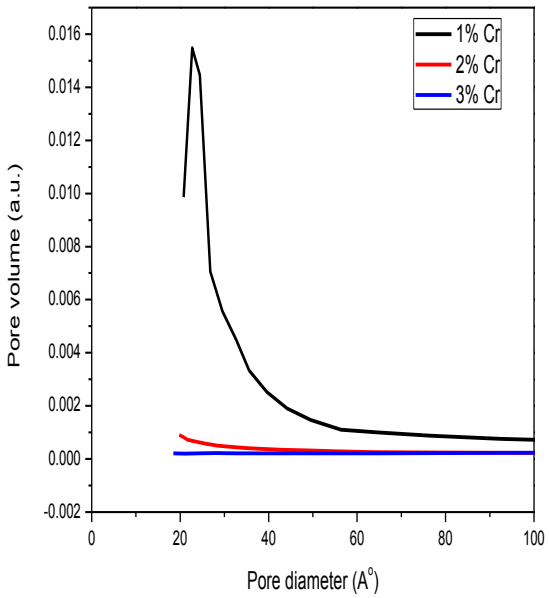

Figure 5. 7: Pore volume against pore diameter for synthesised Cr-MCM-41 at weight loadings of 1%, 3% and 5%.

It is noted that an increase in chromium content drastically decreases surface area as well as pore volume. Nitrogen adsorption isotherm displayed a type III curves which indicates the presence of mesopores as well as micropores. A type IV isotherm curves was reported when synthesising the same materials and suggested that the decrease in pores is due to bond shrinking as well as the excess metal introduced [25]. The BJH plot shows that catalyst has pore sizes as big as 2.5 nm at low chromium content with capillary condensation around P/P_o= 0.5.

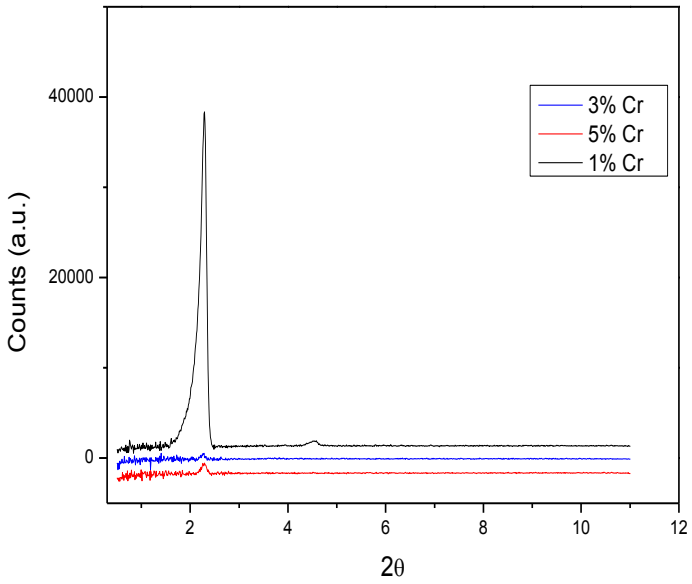

Figure 5. 8: XRD patterns for synthesised Cr-MCM-41 at weight loadings of 1%, 3% and 5%.

XRD patterns of as-synthesised Cr-MCM-41 catalysts are shown in Figure 5.10 in a 2θ angle ranging at 0.5 to 11° with a well resolved line. The presence of reflections 100 and 110 in 1% Cr-MCM-41 catalysts reflect the characteristics of hexagonal mesostructure. As the chromium content increases, the intensity of the peak decreases. This behavior is different from what has been reported when preparing Cr-MCM-41 by wet impregnation as these samples were done. Though tetraethoxysilane was used as silica source which might have had an influence on the framework structure of the synthesised catalysts. The decrease in pore volume and surface area are due to the formation of small Cr-oxide clusters dispersed inside the channel and larger particles in the external surface area [95].

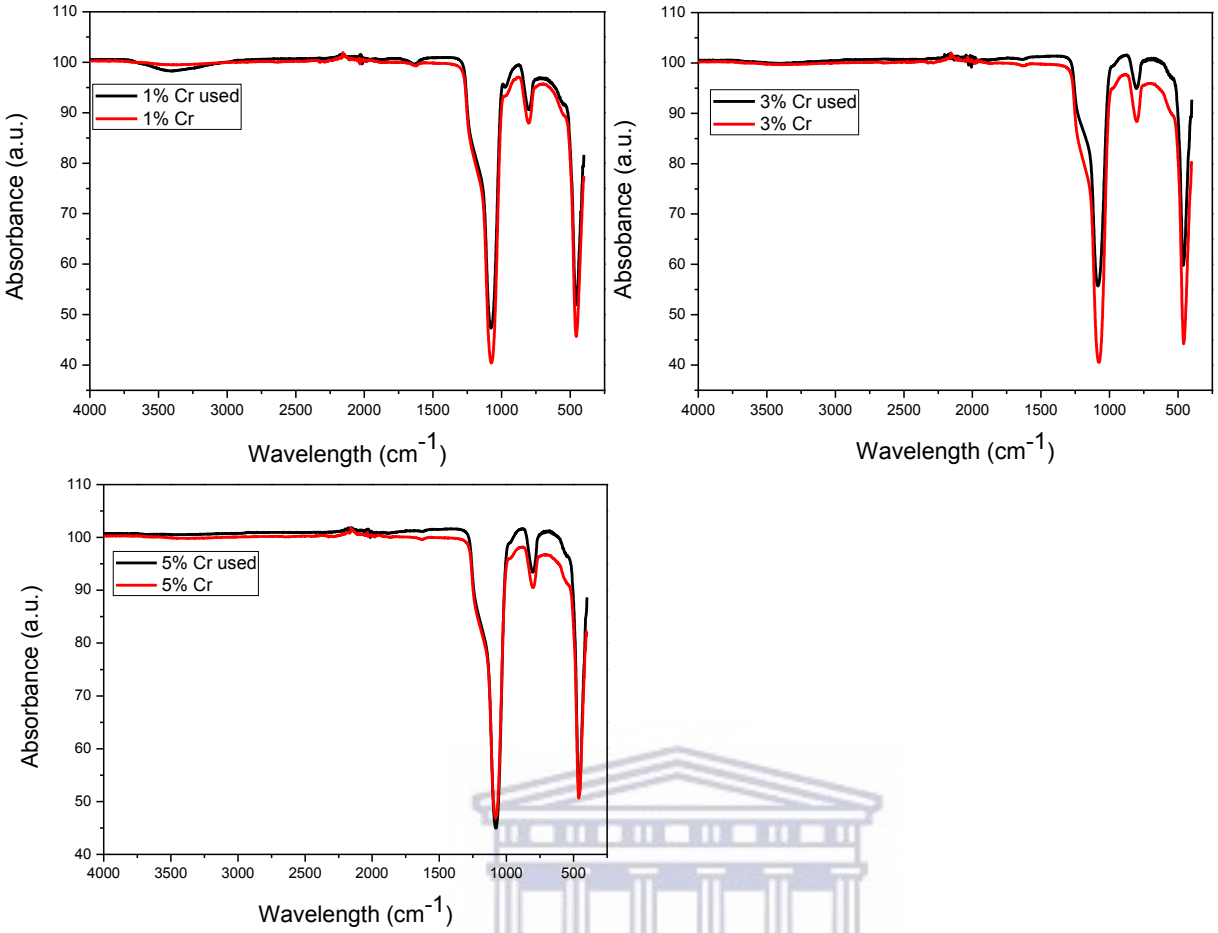

Figure 5. 9: FTIR spectra for synthesised Cr-MCM-41 before and after 1-hexene oligomerisation at weight loadings of (a) 1%, (b) 3% and (c) 5%.

These materials were also analyzed with FTIR in the 450 to 4000 cm^{-1} wavenumber range as shown in Figure 5.11. Hexagonal skeleton of mesoporous MCM-41 is indicated by bands at 1080, 750 and 495 cm^{-1} for asymmetric stretching, symmetric stretching and bending of Si-O-Si skeleton respectively. Bands for asymmetric stretching of Si-O are seen at 1200 cm^{-1} [101] . These seemed to be similar as the spectra obtained for synthesised MCM-41 except that they are narrower with higher intensity. When analysed again after conversion of 1-hexene there were no new peaks formed hence the catalyst was not deactivated due to coke formation. SEM micrographs in Figure 5.12 show that the synthesised material formed a spherical shaped structure of about 20 nm and rod structures of 80 nm lengths. These particles are clustered together which makes it harder to recognise the shape as well as size, which was identified as not of any particular crystalline habit and maybe results of intergrowth of small particles [95].

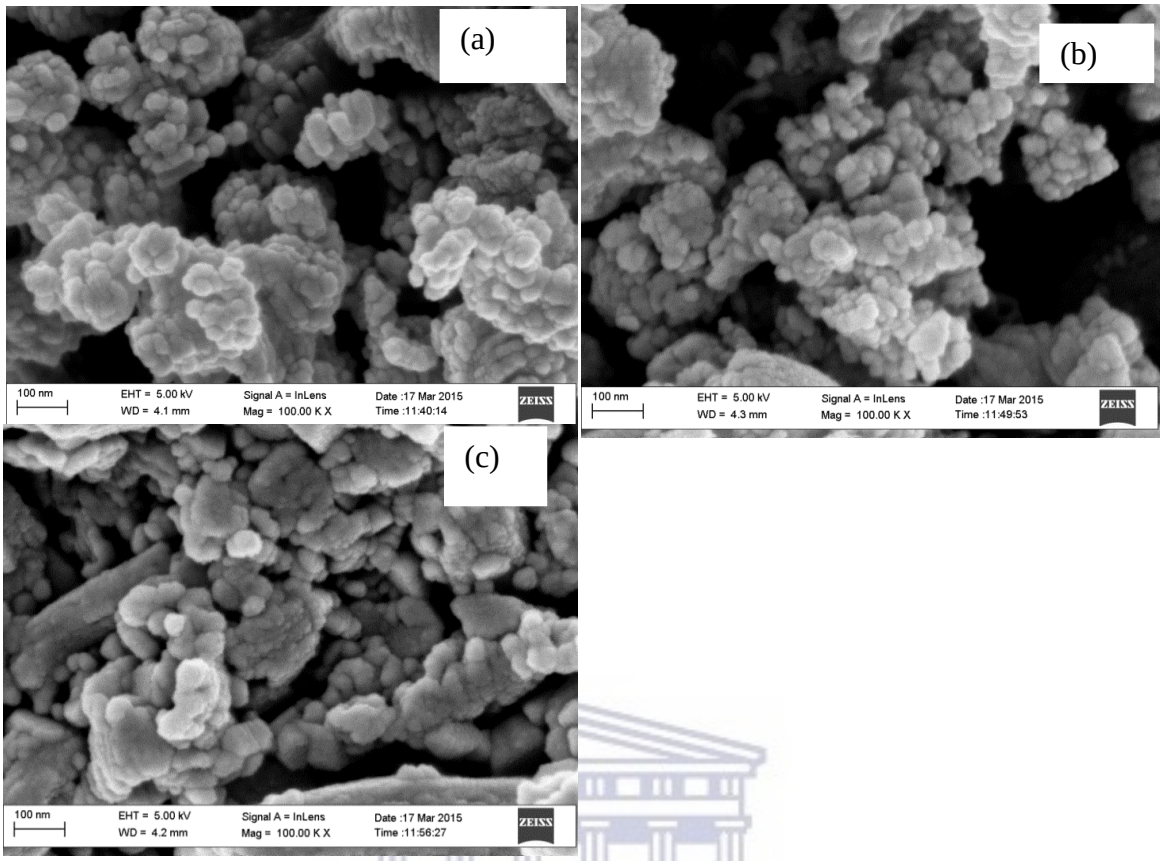

Figure 5. 10: SEM micrographs of synthesised Cr -MCM-41 at weight loadings of (a) 1%, (b) 3% and (c) 5%.

Chemical composition of these materials were analysed by Energy-dispersive spectroscopy (EDS) and tabulated on Table 5.3 below. The EDS analysis show the amount of the reagents precursor that forms part of the final material indicated as atomic percentage.

Table 5. 3: Elemental composition of synthesised Cr/Al-MCM-41 samples detected by energy-dispersive spectroscopy (EDS).

Samples	Si atomic %	Al atomic %	Cr atomic %
1%Cr	9.70	1.28	0.940
3%Cr	14.69	0	33.90
5%Cr	14.58	0	21.31

The synthesised materials were catalytically tested on the conversion of 1-hexene. Conversion to liquid product is plotted as a function of time in Figure 5.13 and its selectivity in Figure 5.14 below.

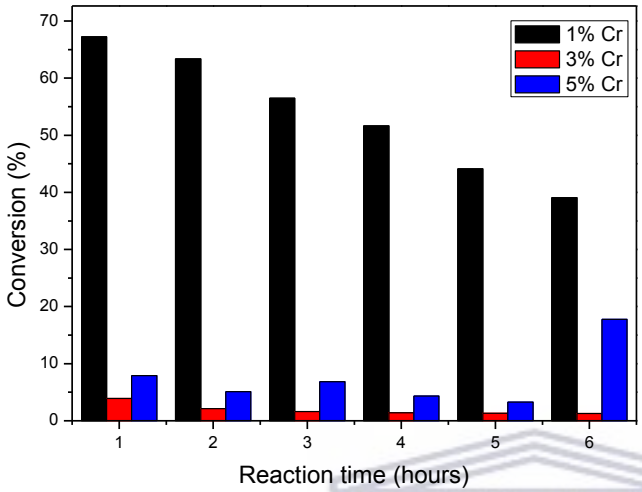

Figure 5. 11: Conversion of 1-hexene to liquid product over different loadings of chromium-modified MCM-41.

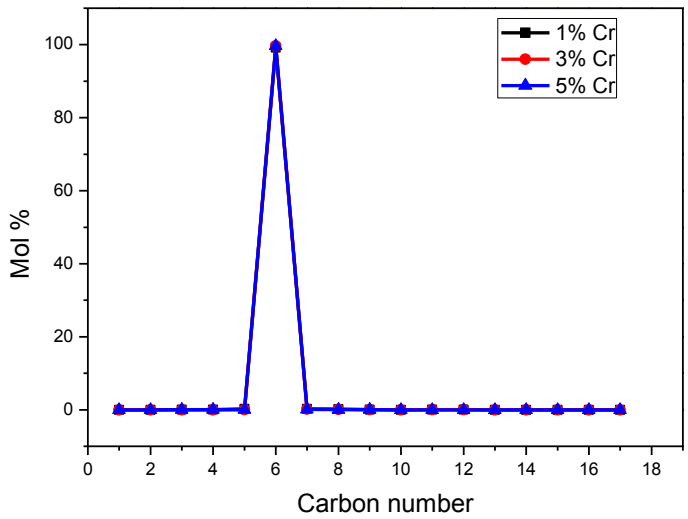

Figure 5. 12: Selectivity of Cr-MCM-41catalysist of different loadings for 1-hexene oligomerisation in a quartz fixed bed reactor at 350 °C.

These catalysts showed about 98% selectivity towards the middle-grouped hydrocarbons while 1% Cr-MCM-41 showed higher conversion**,** which decreases as time passes. This could be explained by presence of aluminium showed in Table 5.3 that contaminated the sample during synthesis. This again proves the improvement of the catalyst in the presence of modified acid sites. FTIR shows the carbohydrate depositing into the structure during the reaction hence the appearance of a bend in 3400 cm^{-1} wavelengths for 1% Cr-MCM-41. Upon calcination, these samples changed from green to yellow which was also seen in Si/(Al + Cr) sample due to transformation of trivalent chromium ions to hexa-valent chromium ions [102].

5.2. 3 Iron-modified MCM-41

Iron was impregnated on silica materials for hopefully an improved activity as a catalyst was studied using BET. This analysis was done to obtain a better picture on the materials surface. Some of the data obtained was tabulated in a table below.

Table 5. 4: Shows the effect of iron on MCM-41 surface area.

MCM-41 catalyst	BET surface (m^2/g)	Ext. surface area (m^2/g)	Pore volume (cm^3/g)	*d*-spacing (Å)[a]	Pore diameter (Å)	Wall thickness(Å)
1% Fe-MCM-41	49.6	44.2	0.116	44.19	23.96	27.07
3% Fe-MCM-41	56.5	49.7	0.136	42.75	19.77	29.59
5% Fe-MCM-41	25.8	17.6	0.093	44.16	20.73	30.26

[a] the *d*-spacing reported herein was determined from the XRD shown in Fig. 5.17 below.

Pore volume as well as pore size distribution are the most crucial parameters for porous material and shape-selectivity catalyst. The plot in Figure 5.15 and Figure 5.16 give an indication of what occurs to pores and surface area as iron binds to silica frame structure.

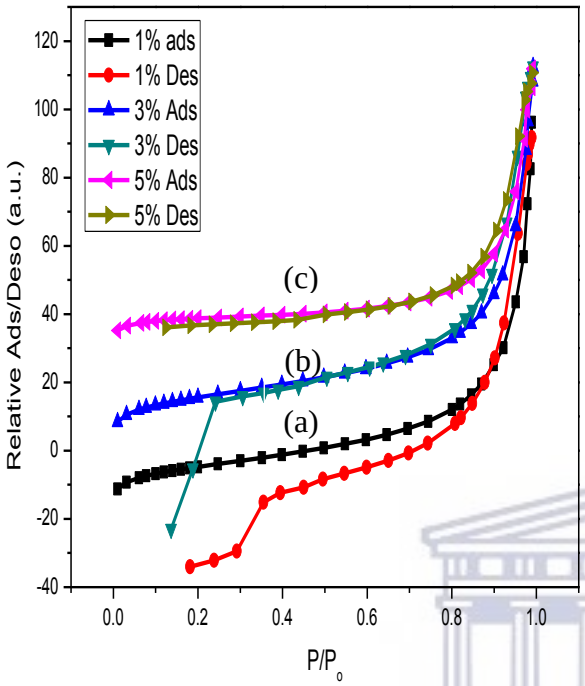

Figure 5. 13: N_2-adsorption isotherms of iron modified MCM-41 at weight loadings of (a) 1%, (b) 3% and (c) 5%.

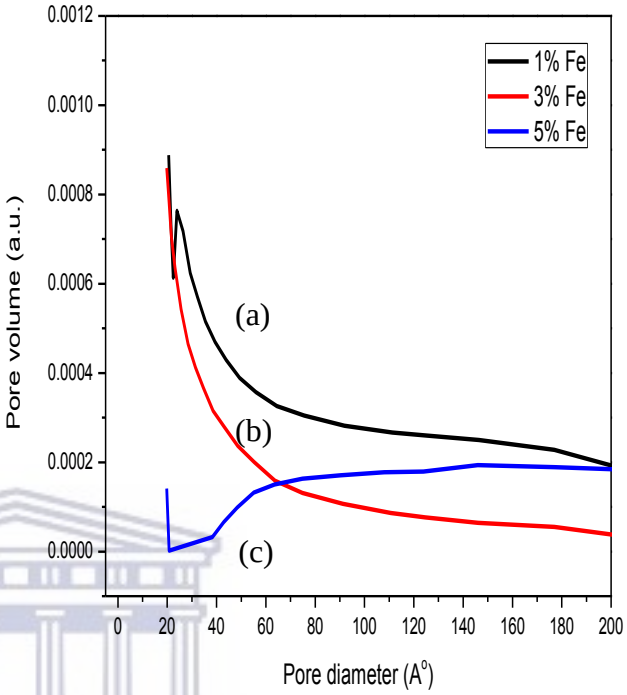

Figure 5. 14: Pore diameter against pore volume of synthesised Fe-MCM-41 at weight loadings of (a) 1%, (b) 3% and (c) 5%

Nitrogen isotherm showed that the synthesised materials form a type III isotherm indicating the presence of micropores. Previous studies showed a type IV isotherms for the synthesised samples which were described as a highly ordered mesoporous material with narrow size distribution [103]. Materials of 1% Fe modified showed pores with a diameter of 2.4 nm which is lower than that was reported of 3.8 nm diameter [93]. Table 5.4 shows the effects posed by introduction of iron into MCM-41. The increase in iron content results in the decrease of surface area and pore volume. Decrease in surface area results in an increase in wall thickness which is due to enhance activity of the catalytic by processing the transportation of the substrate access to the confined mesopores [104].

XRD patterns for Fe-MCM-41 catalysts in Figure 5.17 showed a 100 reflection at 2.4° angle with a *d*-spacing of 44.19Å (1% Fe-MCM-41), 42.75Å (3%Fe-MCM-41) and 44.16Å (5% Fe-MCM-41). These peaks correspond to hexagonal arrangement pore structure MCM-41 their intensity decreases as iron loading increases which were also reported [108]. The fact that no unknown peak is detected on the XRD pattern means that all iron has been uniformly dispersed on surface of MCM-41 [105, 106]. FTIR in Figure 5.18 showed three main bands which had been observed for MCM-41 corresponding to stretching and bending vibrations of Si-O-Si bridge.

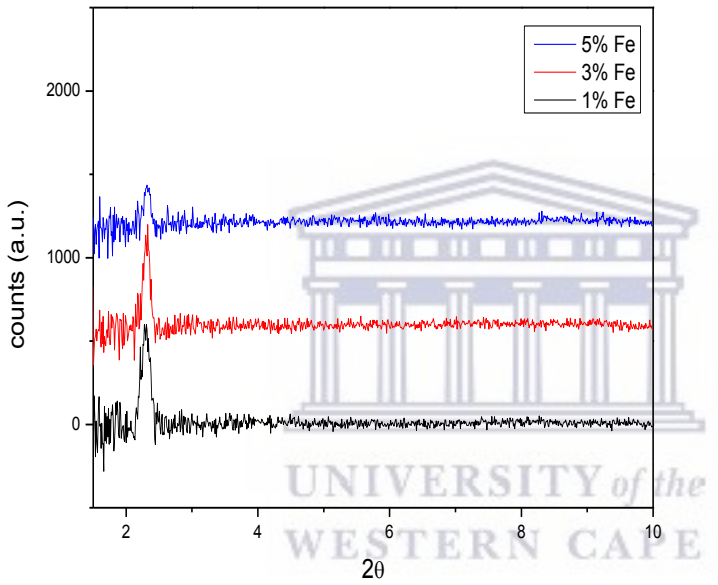

Figure 5. 15: XRD patterns measured at 2-theta angle for Fe-MCM-41 at weight loadings of 1%, 3% and 5%.

The NO^- ion vibration should be observed at 1380 cm^{-1} to confirm the presence of $Fe(NO_3)_3$ in the synthesized Fe-MCM-41 [107]. This band is not visible in the FTIR spectra but it might be possible that it has joined the shoulder on band 1080 cm^{-1}. Band at 470 cm^{-1} correspond to bending of $Si\text{-}O^-$ groups on the surface. While the bands at 810 and 1090 cm^{-1} correspond to symmetric and asymmetric Si-O stretching vibrations. These are the same bands which have been obtained for other synthesised materials.

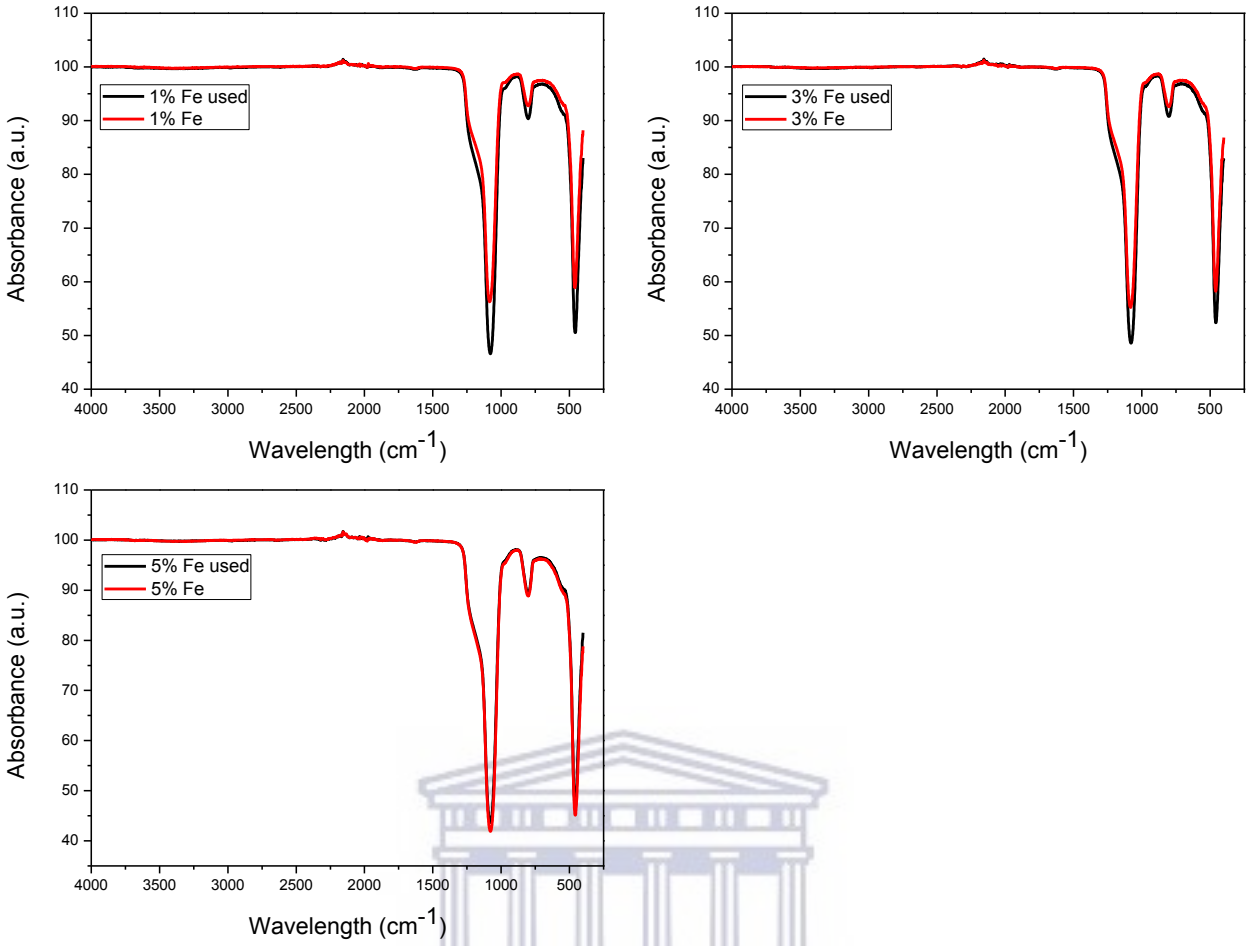

Figure 5. 16: FTIR spectra of Fe-MCM-41 before and after 1-hexene oligomerisation with metal weight loading of (a) 1%, (b) 3% and (c) 5%.

A different morphological shape has been obtained, shown in Figure 5.19**,** where spherical and rod structural species appeared which are small than what was previously reported. The size of these materials depends on the condensation of silica and length of silicate-CTA^+ micelles. The decrease in particles size is due to an increase in iron content which is believed to have an effect on the charge interaction between ferric species and silicate-CTA^+ micelles [107].

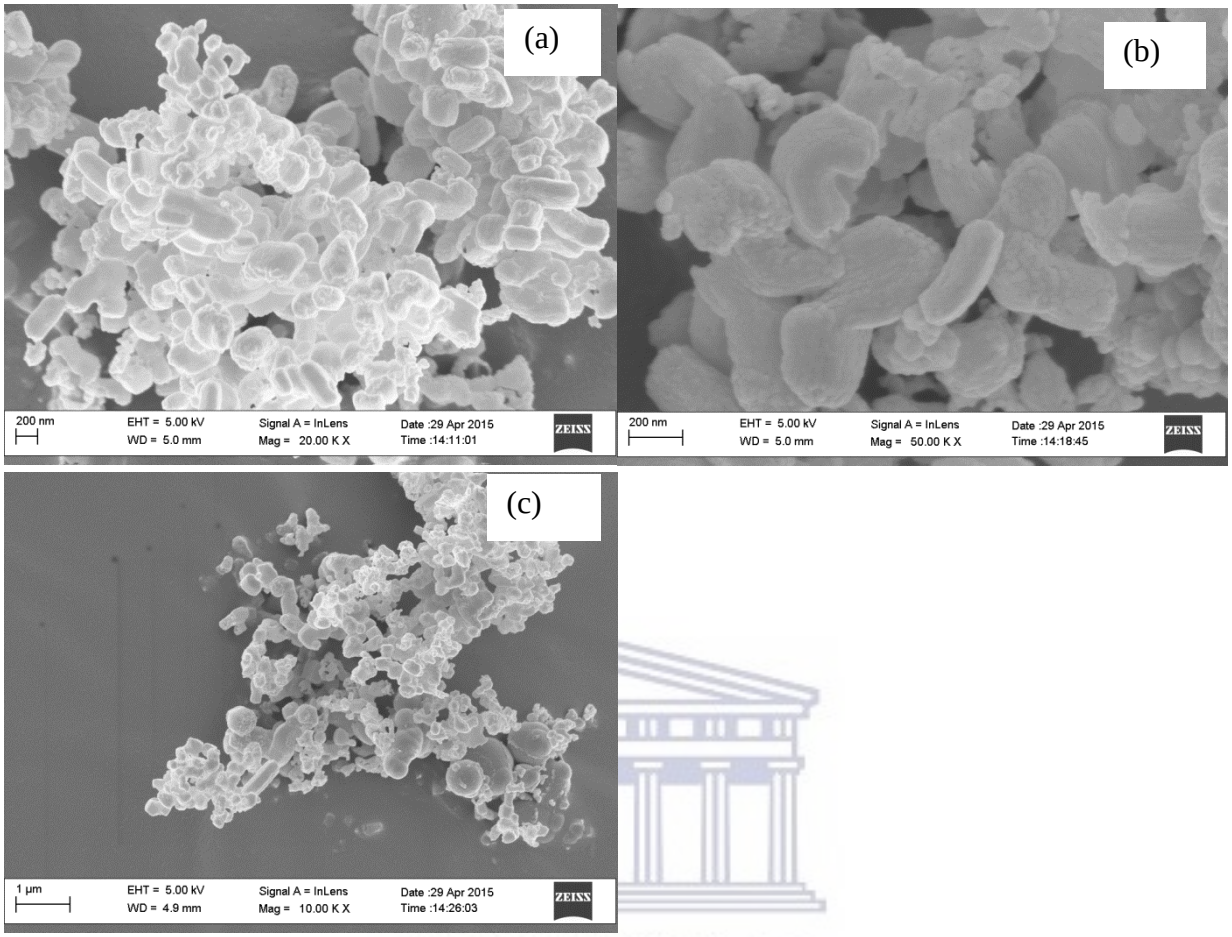

Figure 5. 17: SEM micrographs of MCM-41 modified with iron weight loadings of (a) 1%, (b) 3% and (c) 5%.

Chemical composition of the synthesised material was obtained by SEM equipped with EDS. The table below show atomic percentage of each elemental composition within the synthesised sample. The displayed information showed that the amount of iron integrated on the silica framework structure in not consistent.

Table 5. 5: Elemental composition of synthesised Fe-MCM-41 samples detected by energy-dispersive spectroscopy (EDS).

Samples	Si atomic %	Fe atomic %
1%Fe	38.84	0.91
3%Fe	34.90	2.30
5%Fe	31.81	1.22

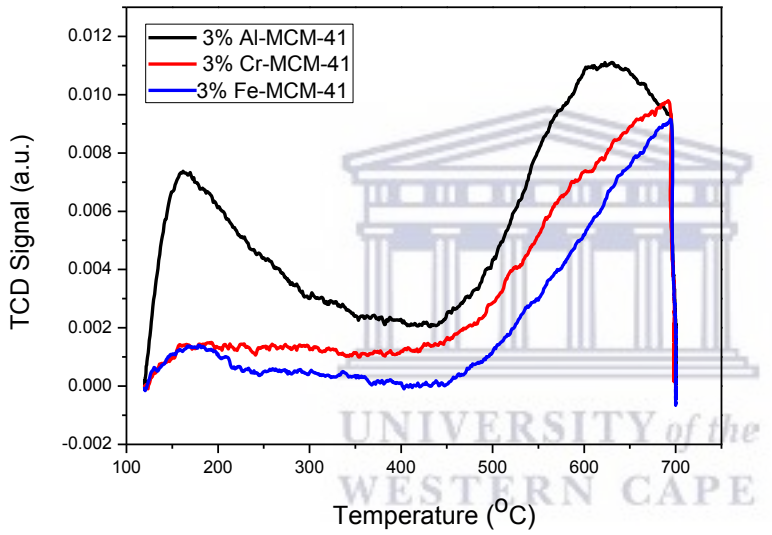

Figure 5. 18: Ammonia-TPD profiles of modified MCM-41 with equal amount of different metal.

The ability of metal reduction is considered as a useful tool for it allows the study of metal-support interaction. Direct incorporation of metal to the synthesis gel has shown reduction in catalyst ability. The highly dispersed small metal oxides results in stronger interaction with the support hence reduced reduction [94]. The TPD pattern above show adsorption peaks at ±165° for Brönsted acid sites and at range from 630 to 695° for Lewis acid sites as shown in the table below. Reduction temperature for these impregnated species is lower compared to co-precipitated material which indicates weak interaction between metal and support. Higher acid sites of aluminium catalyst imply higher activity which was the opposite when these

materials were tested for catalytic activity. The iron catalyst was found to be more active which may imply that these materials are not good oligomerisation catalyst.

Table 5. 6: Acidity of modified MCM-41 samples measured by ammonia-TPD

Samples	Brönsted acids sites (200-400 °C)	Lewis acid sites (400-700 °C)	Total acidity (mmol/g)
3% Al-MCM-41	0.117 (162 °C)	0.167 (630 °C)	0.284
3% Cr-MCM-41	-	0.155 (692 °C)	0.155
3% Fe-MCM-41	0.023 (168 °C)	0.158 (695 °C)	0.181

Testing of these materials for catalytic activity reaction resulted in liquid product which was analysed by gas chromatograph. The conversion of 1-hexene feed was plotted as a function of time shown in Figure 5.21 and selectivity of the catalyst in Figure 5.22 below.

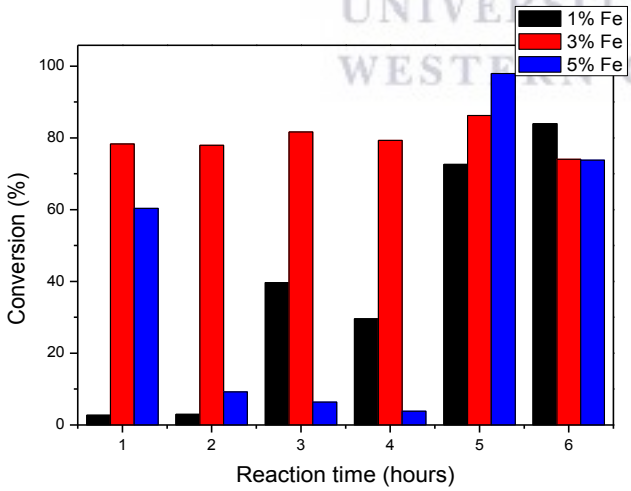

Figure 5. 19: Conversion of 1-hexene to liquid products over modified MCM-41 catalyst at Fe weight loadings of (a) 1%, (b) 3% and (c) 5%.

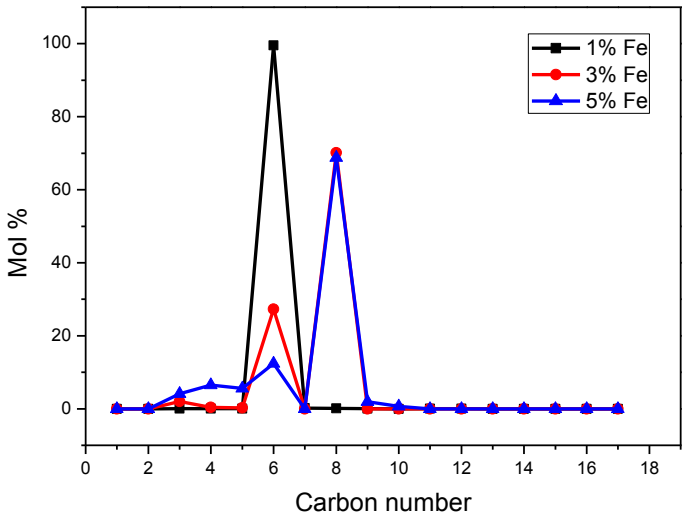

Figure 5. 20: Selectivity of Fe-MCM-41 catalysts at weight loading of (a) 1%, (b) 3% and (c) 5% over conversion of 1-hexene in quart fixed bed reactor a 350 °C.

Catalyst containing 1% Fe-MCM-41 showed an increase in the conversion of 1-hexene after two hours while 3% Fe-MCM-41 catalyst maintained between 75 and 85% conversion. 5% Fe-MCM-41 and 3% Fe-MCM-41 showed an increase selectivity of 70% to C_8 hydrocarbon this showed that the catalyst does more than just isomerisation. Catalyst of 5% Fe-MCM-41 showed a decreasing than increasing activity or conversion with 70% selectivity toward C_6 hydrocarbons. Particle size has the effect on the reaction as smaller addition of metal to MCM-41 showed higher conversion. This is because nano-particles allow accessibility of reactant to catalytic Fe species in a shorter mesoporous channels. The shorter the channels, the less the chances of the by-product clotting in the channels, hence the catalyst remains active for longer [109]. Table 5.5 shows the chemical composition of the catalyst and it explains higher activity of 3% Fe-MCM-41 Fe catalyst than 5% Fe-MCM-41 is due to larger amount of metal content.

5. 3 Conclusion

Impregnation of metal ions to mesoporous resulted in the reduction of pore diameter and surface area. Nitrogen adsorption isotherms indicated an increase in micropores rather than

mesopores as pore diameter became smaller while the amount of metal incorporated increases. Chromium showed a larger effect on the pore size due to its larger atomic radius. Introduction of aluminium into MCM-41 retained the highly ordered MCM-41 structure as proven by appearance of three peaks. The absence of these peaks upon iron and chromium introduction onto MCM-41 structure can be concluded as collapsing of MCM-41 framework structure.

Metal incorporation had the same effect on mesoporous MCM-41 morphology as spherical shaped species has been observed for all the synthesised material. Even if the XRD reflection suggest loss of highly ordered MCM-41 framework structure, FTIR show no effect on the structure as the same peaks has been obtained for every synthesised species. Activity of Al-Ammonia-TPD show that incorporation of aluminium increases both Brönsted and Lewis acid sites in the catalyst while Chromium and ion produces Lewis acid sites.

MCM-41 catalyst was not dependent on the amount of aluminium introduced as conversion and selectivity were merely the same. While catalysts with lower amounts of chromium seem to be the more active catalyst, 3% and 5% Fe-MCM-41 showed a promising activity towards 1-hexene oligomerisation even with an increased selectivity toward C_8 hydrocarbons. Looking at the ammonia-TPD result conversion of 1-hexene require catalyst with stronger acid sites than just aluminium. Therefore, we concluded that co-precipitated is the best synthesis method for metal doped MCM-41 catalyst.

CHAPTER 6: Mixed metal-modified mesoporous MCM-41

6. 1 Brief introduction

Modification of MCM-41 has become the most important study in petrochemical industries due to the catalytic properties it possesses. Al-MCM-41 is used as a support due to its higher hydrothermal stability than siliceous MCM-41. Aluminium introduction to framework of MCM-41 increases the acidity as well as capacity of ion-exchange [108]. Chromium incorporation is known to be effective on redox reactions due to its mechanical strength and good thermal stability on the silica-alumina support material. The acid-base properties of the support determine the nature of metal species as these metals can stabilize in various oxidation state [109].

In this chapter the mixed-metal doped MCM-41 is prepared under hydrothermally conditions at 150 °C and calcined at 560 °C to remove water and excess material that is not chemically bound to the framework structure. Iron and chromium are introduced to Al-MCM-41 through co-precipitation.

6. 2 Results and discussion

6.2. 1 Chromium-modified Al-MCM-41

Earlier it was stated that addition of aluminium creates acid sites for these silica materials. Chromium (Cr) has also been used in heterogeneous catalysts because of the improved life span as well as activity of the catalysts. But introduction of these two metals simultaneously to silica materials causes major effects on surface area as well as pore volume. Table 6.1 below shows changes in those variables due to amounts of metal added. These data were obtained using BET analysis technique.

Table 6. 1: Effect on Al-MCM-41 surface area as it is modified by chromium addition.

MCM-41 catalyst	BET surface (m^2/g)	Ext. surface area (m^2/g)	Pore volume (cm^3/g)	*d*-spacing (Å)[a]	Pore diameter (Å)	Wall thickness (Å)
MCM-41	955	1001	0.920	41.52	37.03	10.91
Al/Cr 30	399	476	0.697	41.28	20.61	27.06
Al/Cr 80	210	196	0.587	42.99	23.44	26.20
Al/Cr 110	175	159	0.520	31.29	23.72	12.41

[a] the *d*-spacing reported herein was determined from the XRD shown in Fig. 6.3 below

Pore volume as well as pore size distribution are the most crucial parameters for porous material and shape-selectivity catalyst. Nitrogen adsorption isotherms of these materials were measured at -196 °C after degassing at 400 °C for 4 hours. The isotherm plots in Figure 6.1 are due to the amount of nitrogen adsorbed at a fixed relative pressure. The BJH method was used to determine the pore size distribution shown in Figure 6.2. This shows the effect of aluminium incorporation on the pores of siliceous material.

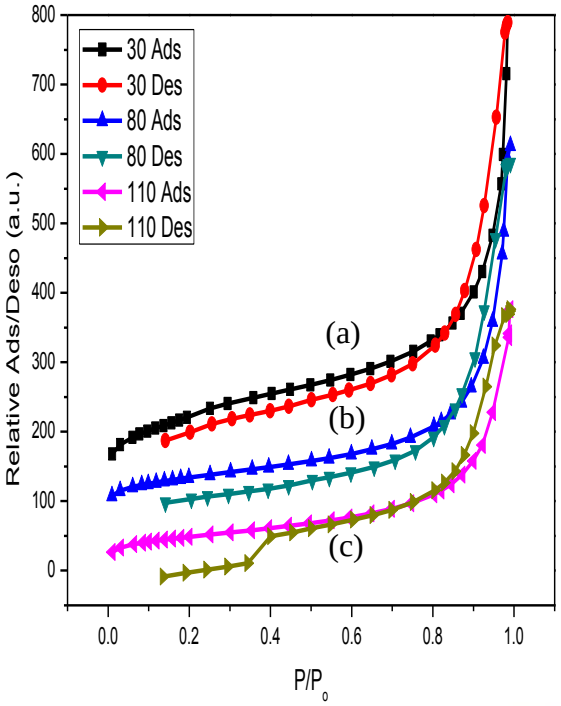

Figure 6. 1: N_2-absorbtion isotherms for synthesised Cr/Al-MCM-41 at a Cr/Al ratio of (a) 30, (b) 80 and (c) 110.

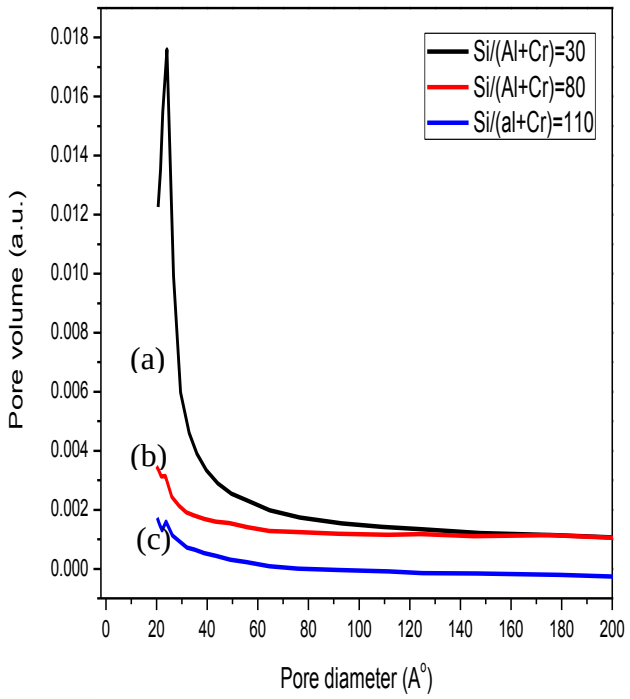

Figure 6. 2: Pore volume against pore diameter for synthesised Cr/Al-MCM-41 at a Cr/Al ratio of (a) 30, (b) 80 and (c) 110.

Upon calcination, these samples changed from green to yellow. Colour change is due to the transformation of trivalent chromium ions to hexa-valent Cr ions [90]. These materials were further analysed by BET analysis and Table 6.1 above shows the effects of chromium incorporation on the surface area, wall thickness as well as the pore volume of these silica materials. It is seen that higher metal content in a single doped metal resulted in thicker walls, than double-doped aluminium + chromium (Al + Cr) ratio. Nitrogen isotherm showed type III isotherms which indicate the presence of microporous material with pore diameter of 2.3 nm.

The X-ray diffraction patterns of powder material were characterised at a region of 1.0 to 10° displayed in Figure 6.3. This allows the determination of the material phase, purity and degree of crystalline.

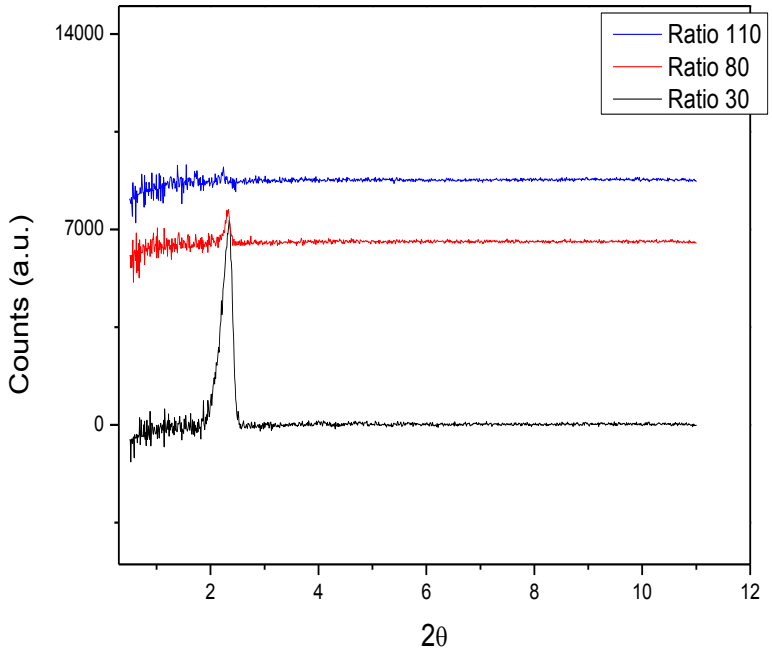

Figure 6. 3: XRD patterns for synthesised Cr/Al-MCM-41 at a Si/(Al + Cr) ratio (a) 30, (b) 80 and (c) 110.

XRD patterns show an intense peak for material of Si/ (Al + Cr) ratio of 30 than Si/ (Al + Cr) ratio 80 and 110 This behavior is different to what has been obtained before. Si/ (Al + Cr) ratio of 80 shows a small peak at reflection (100) while Si/ (Al + Cr) ratio of 110 is almost invisible. These findings need to be confirmed by repeating the synthesis to eliminate any experimental error during synthesis. The disappearance of the peaks were reported in reflection (200) and (210) with the reduction in the intensity corresponds to an increase in metal loading [108].

However, the FTIR spectra illustrated in Figure 6.4 showed all the bands seen in the synthesised MCM-41 with no new peak to indicate the introduction of the metal. Bands at 470 cm^{-1} correspond to bending of $Si\text{-}O^{-}$ groups on the surface. While the bands at 810 and 1090 cm^{-1} correspond to symmetric and asymmetric Si-O stretching vibrations. The shoulder peak at 960 cm^{-1} is associated with tetrahedral coordination of M-Si-O, (M-metal) [110]. The poor intensity of this peak shows that there is lower tetrahedral bounded metal in the synthesised material. The intensity of peaks decreases as more metal is incorporated which has been seen for all the metal-doped materials.

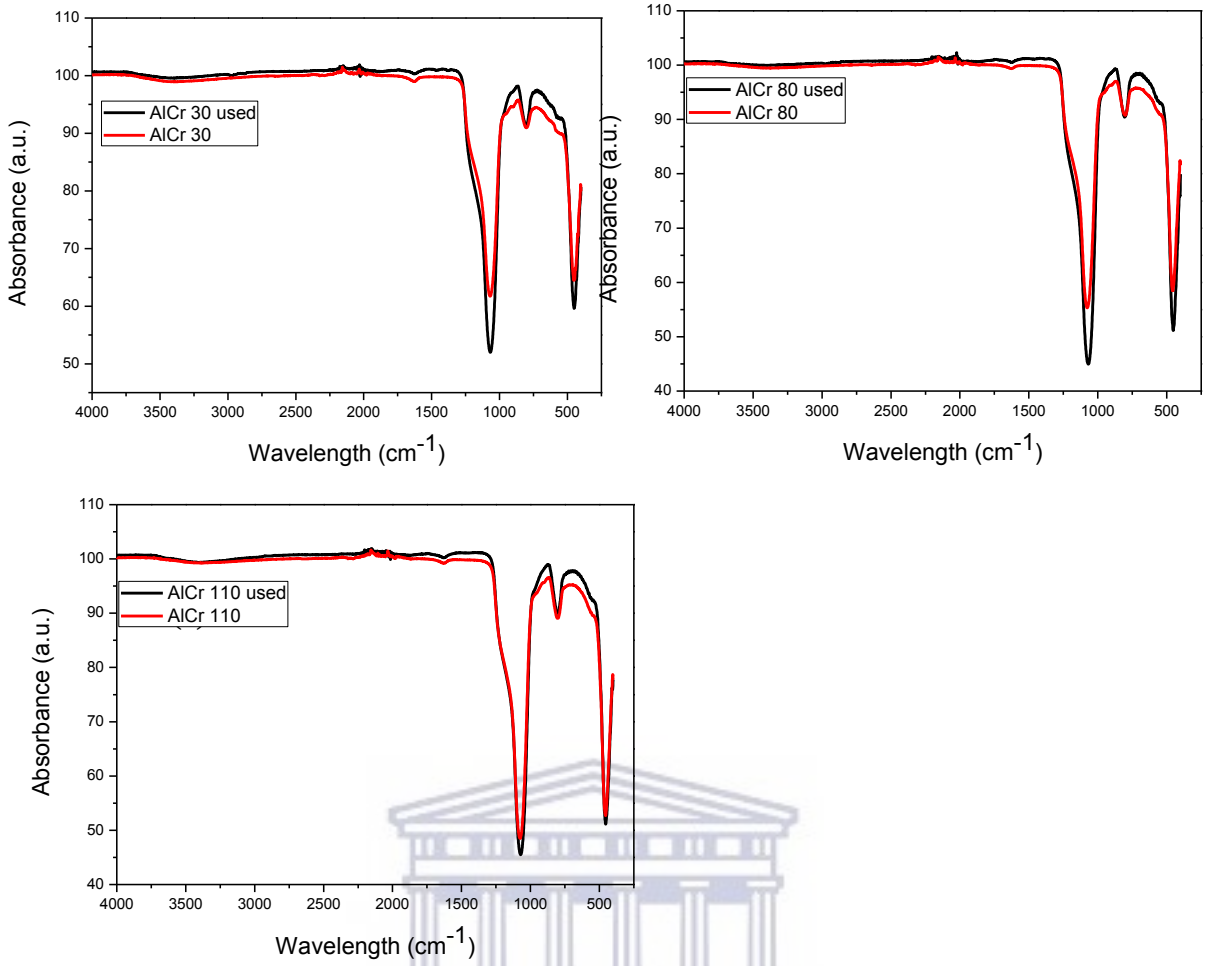

Figure 6. 4: FTIR spectra for synthesised Cr/Al-MCM-41 with Si/(Al + Cr) ratios of (a) 30, (b) 80 and (c) 110 before and after 1-hexene oligomerisation.

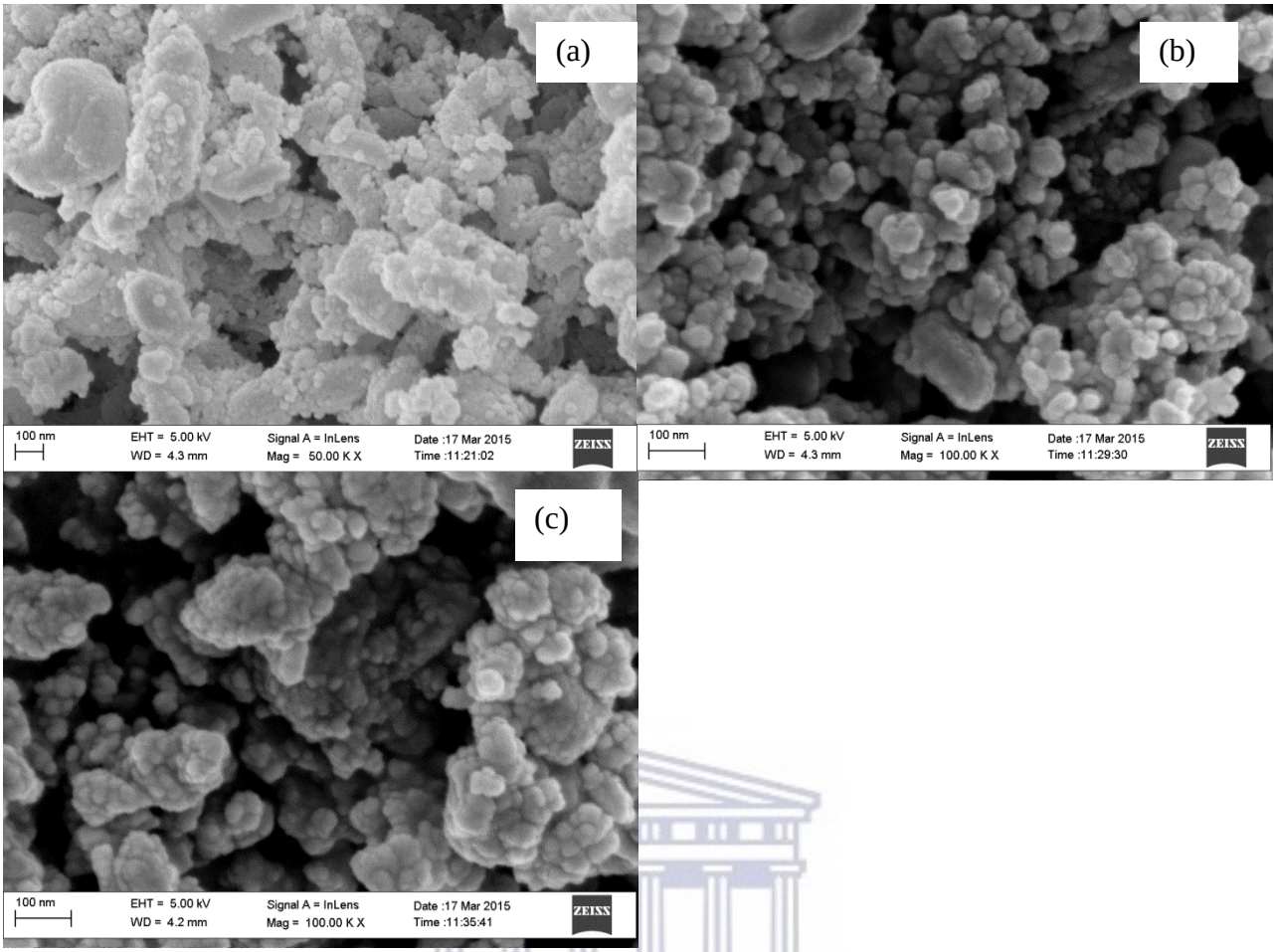

Figure 6. 5: SEM micrographs of synthesised Cr/Al-MCM-41 at a ratio (a) 30, (b) 80 and (c) 110.

Morphology of the materials was obtained using SEM micrograph and materials seem to form rod shapes as well as the spherical shapes. Image (a) in Figure 6.5 shows some flake on the surface of the form shape particles which may be the excess metal positioning itself on the surface [12]. The flakes where identified as chromium which is influenced by reaction conditions such as oxygen content, water content or hydrogen partial pressure [109].

Table 6.2 below shows the amount of the reagent precursor that forms part of the final material. Precise Si/Al ratio of the synthesised material were then calculated and displayed in the table.

Table 6. 2: Elemental compositions of synthesised samples detected by energy-dispersive spectroscopy (EDS).

Samples	Si atomic %	Al atomic %	Si/Al ratio	SiO_2/Al_2O_3 ratio
Si/(Al + Cr) = 30	17.96	1.35	13	26
Si/(Al + Cr) = 80	14.3	0.45	31	62
Si/(Al + Cr) = 110	12.62	0.23	55	110

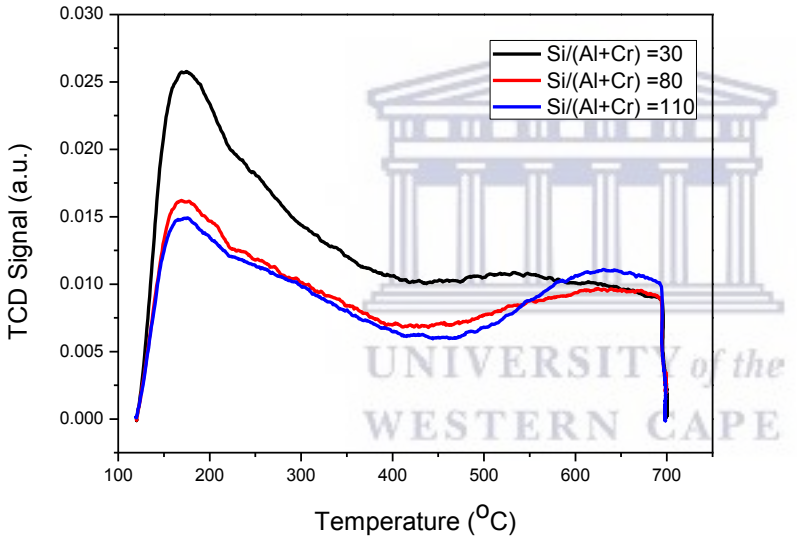

Figure 6. 6: Ammonia-TPD profiles of Cr/Al-MCM-41 at different Si/(Al + Cr) ratios.

Synthesised samples showed a higher intensity peak at 170 °C which is associated with Brönsted acid sites. These are considered as weak sites as they are dissociated at lower temperature. The second desorption peak around 680 °C is associated with Lewis acid sites. Si/ (Al + Cr) ratio of 80 and 110 show the same almost the same number of acid site as seen in the Table below. Even though Si/ (Al + Cr) ratio of 30 show a higher number of acid sites these site is mostly the Brönsted sites, hence higher intensity at 169 °C desorption temperature. The lower desorption temperature at 169 °C compared to Si/(Al + Cr) ratio of 30 at 177 °C is associated with the decrease in acid sites [79].

Table 6. 3: Acidity of Cr/Al-MCM-41 samples measured by ammonia-TPD

Samples	Brönsted acids sites (200-400˚C)	Lewis acid sites (400-700˚C)	Total acidity (mmol/g)
Si/(Al + Cr) =30	0.413 (169 °C)	0.090 (689 °C)	0.503
Si/(Al + Cr) = 80	0.257 (169 °C)	0.103 (686 °C)	0.360
Si/(Al + Cr) =110	0.237 (165 °C)	0.130 (645 °C)	0.367

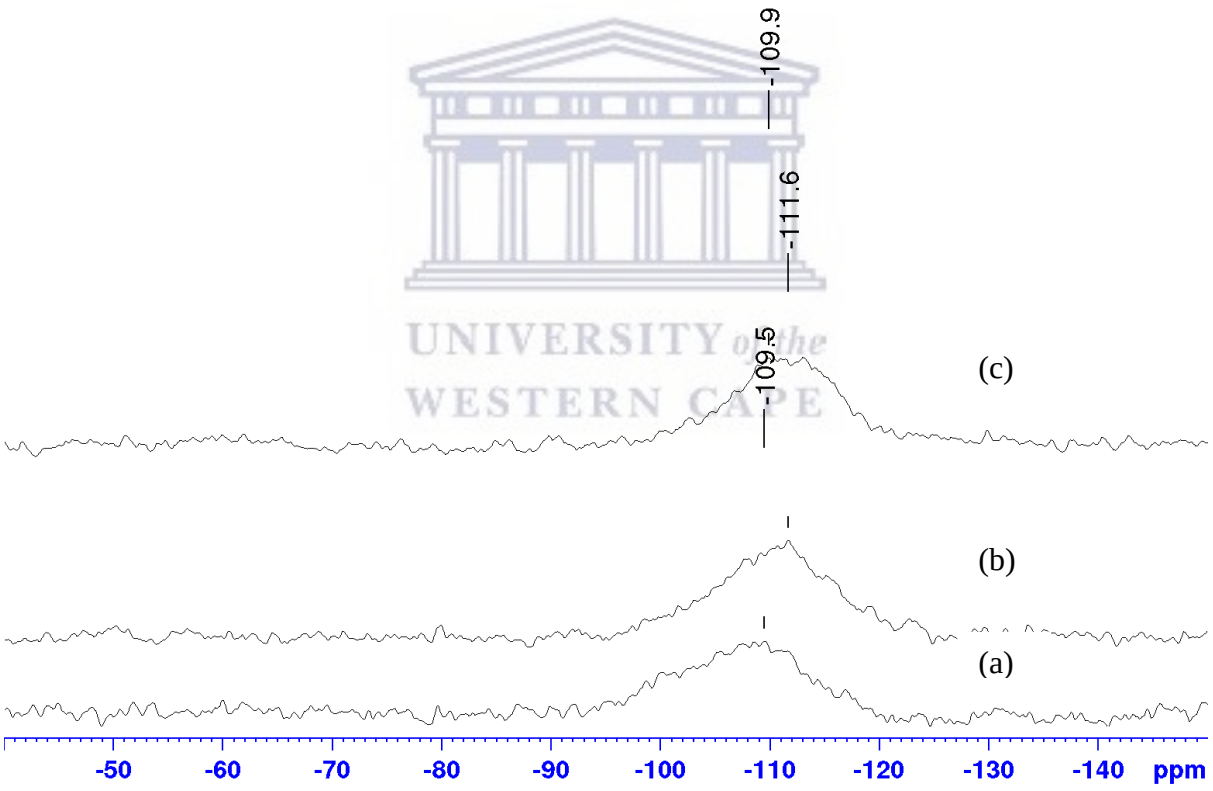

Figure 6. 7: ^{29}Si NMR spectra of Cr/Al-MCM-41 at Si/(Al + Cr) ratios (a) 30, (b) 80, (c) 110.

The ^{29}Si NMR spectra of Cr/Al modified MCM-41 with different ratios are shown in Figure 6.7 above. Synthesised materials show major broad peak around -95 to -120 ppm region. This

is the combination of different peaks with different state of silica species. At -110 ppm peak is assigned to silicon atoms with four siloxanes (Si $(OSi)_4$) while the shoulder at -102 ppm is assigned to silanol group (Si-$(OSi)_3$ OH). The broadening of the peaks is due to incorporation of chromium which also results in reduction of peak intensity. It is believed that during calcination silanol group reacts with extraskeletal chromium hence decrease in peak intensity as chromium content increases [109, 111].

The resonance peak with lower intensity at an average 54 ppm is observed for all synthesised materials. This is assigned to tetrahedral coordinated aluminium while the peak at -0.1 ppm is associated to octahedral coordinated aluminium arises during calcination. The synthesised samples have a higher amount of octahedral coordinated aluminium, hence higher the peak intensity at -0.1 ppm. The intensity of this peak increases with decrease in metal content [89].

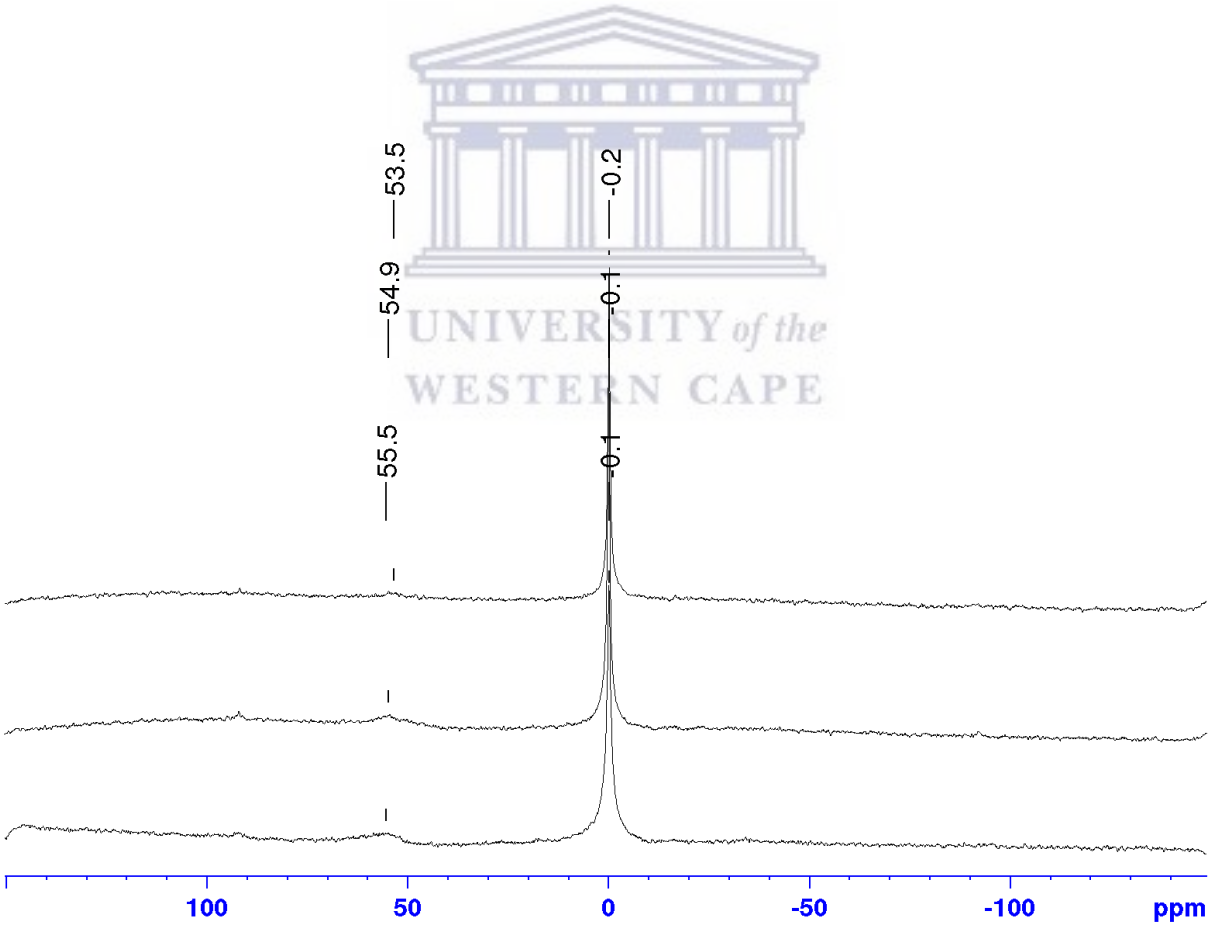

Figure 6. 8: ^{27}Al NMR spectra for Cr/Al-MCM-41 at Si/(Al + Cr) ratios (a) 30, (b) 80, (c) 110.

Synthesised materials were tested on the oligomerisation of 1-hexene on the fixed bed reactor made of quarts. Product obtained hourly from the oligomerisation of 1-hexene at 350 °C were analysed by gas chromatography. The effect of time on the conversion of product is shown on Figure 6.9 below.

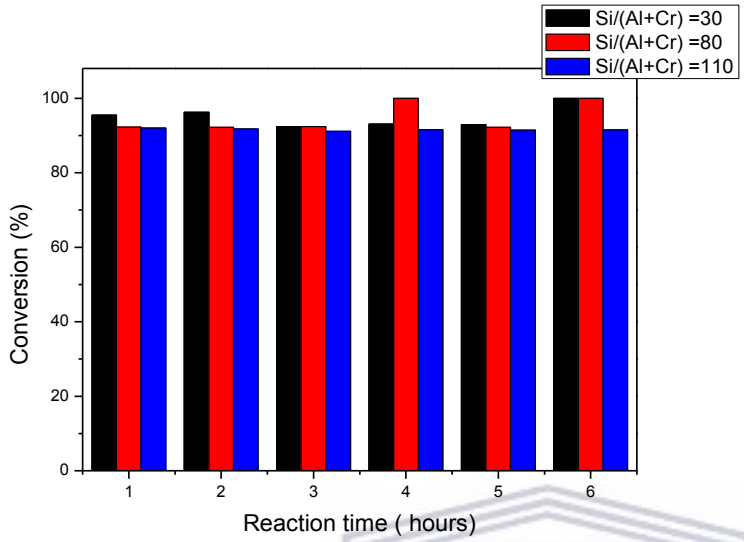

Figure 6. 9: Conversion of 1-hexene to liquid product over catalyst with various Si/(Al + Cr) ratio.

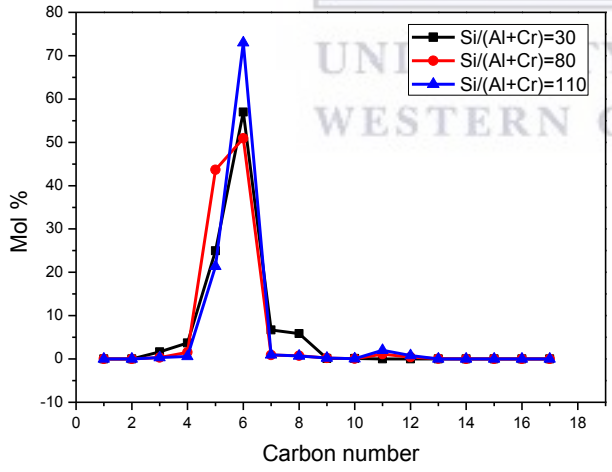

Figure 6. 10: Selectivity of Cr/Al-MCM-41 catalyst in the oligomerisation of 1-hexene to different hydrocarbons.

The synthesised materials showed a 1-hexene conversion that was above 90% with a slightly increase or decrease depending on the sampled hour. The amount of aluminium and

chromium added did not influence the reaction conversion. The calculated selectivity of the synthesised material was plotted and displayed in the figure above. These materials showed selectivity of 52%, 59% and 75% for Si/ (Al + Cr) ratio of 80, 30 and 110, respectively to C_6 hydrocarbons. The increase on metal content resulted in reduction in 1-hexene conversion as 110 conversions is higher. The Si/ (Al + Cr) ratio of 80 also showed higher selectivity of 45% to C_5 hydrocarbons compared to 20% of other catalysts. It is believed that the bump seen for C_{11} hydrocarbons can increase if the reaction should be carried out at higher pressure. Due to a short period which this reaction was carried the lifespan of the catalysts could not be stated.

The liquid product was analysed using DHA chromatogram which the variety carbon species were present as indicated in table 6.4 below

Table 6. 4: Liquid fragments of the oligomerisation product in mass % over Cr/Al-MCM-41

	Paraffins Cyclo	**i-Paraffin**	**n-Paraffins**	**Olefins**	**Aromatics**	**Others**	**Total**
	0.00	0.00	0.00	0.00	0.00	6.14	6.14
C4	0.00	4.40	0.08	0.35	0.00	0.00	4.83
C5	0.00	7.77	0.06	0.80	0.00	0.12	8.75
C6	0.09	0.00	3.42	30.94	0.00	15.02	49.47
C7	0.08	3.84	0.00	3.54	0.34	0.58	8.39
C8	1.37	1.25	0.34	1.62	0.16	0.00	4.74
C9	0.85	1.68	0.00	1.06	0.09	0.00	3.68
C10	0.29	2.08	0.00	0.16	2.28	0.00	4.82
C11	0.00	0.71	0.57	0.00	5.09	0.00	6.38
C12	0.63	0.56	0.09	0.00	0.80	0.00	2.09
Heavy	0.00	0.00	0.00	0.17	0.00	0.00	0.17
Total	**3.30**	**22.30**	**4.57**	**39.20**	**8.77**	**21.87**	**100.0**

Cr/Al-MCM-41 catalyst at Si/ (Al + Cr) ratio of 80 was used in 1-hexene conversion at an increased pressure of 40 bar and temperature of 250 ℃. These conditions were chosen to

mimic the industrial conditions. The sampling was done every 4 hours of the day then left to run overnight. We have concluded that the synthesised materials are active isomerisation catalysts. But with an application of pressure to the conversion reaction different structural paraffins were obtained which makes 30 mass % of the product. Most of these were iso-paraffins with mass % of 22.30 with most of it being C_5 then C_4. Olefins were the higher content of the liquid product with 39.2 mass %. Most of the olefins were C_6 hydrocarbons with 30.9 mass % which agreed with the theory that this catalyst is an active isomerise. The 8.77 mass % of aromatic were obtained with the main being C_6 and about 21.8 mass% of the un-identified species. More data collected on this reaction is shown in Appendix B. Conclusion is made that the catalyst selective to the isomerisation reaction but not limited to it.

6.2. 2 Iron-modified Al-MCM-41

Iron in silica-alumina supported heterogeneous catalysts improves the activity of the catalysts. It is believed that the activity is due to reduced efficient scavenging of hydroxyl radicals by silica next to iron oxide surface. Oxidants production due to dispersion of iron on the surface also counts for higher activity [112]. There surface analysis was done by BET and the data is shown in Table 6.5 below.

Table 6. 5: Surface analysis of Fe modified Al-MCM-41 catalyst with different Si/(Al + Fe) ratios.

MCM-41 catalyst	BET surface (m^2/g)	Ext. surface area (m^2/g)	Pore volume (cm^3/g)	*d*-spacing (Å)[a]	Pore diameter (Å)	Wall thickness (Å)
Al/Fe 30	800	1187	0.837	37.83	25.80	17.88
Al/Fe 80	254	278	0.439	51.57	22.92	36.63
Al/Fe 110	158	157	0.294	49.8	20.59	36.91

[a] the *d*-spacing reported herein was determined from the XRD shown in Fig. 6.14 below

Pore volume as well as pore size distribution are the most crucial parameters for porous materials and shape-selectivity catalysts. The plot in Figure 6.11 and Figure 6.12 gives an indication of what occurs to pores and surface area as metals binds to silica frame structure. Si/ (Al + Fe) ratio of 30 show a type IV isotherm which indicate mesopores while Si/ (Al + Fe) ratio of 80 and Si/ (Al + Fe) ratio of 110 display a type III isotherm indicating the presence of micropores. The BJH plot shows a pore diameter of 2.3 nm for all the synthesised materials.

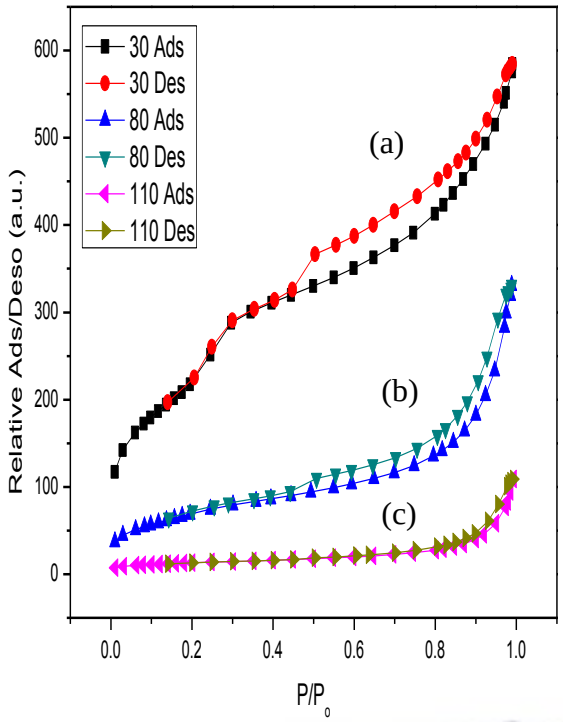

Figure 6. 11: N_2-adsorption isotherms for synthesised Fe/Al-MCM-41 catalysts at a Si/ (Al + Fe) ratios of (a) 30, (b) 80 and (c) 110.

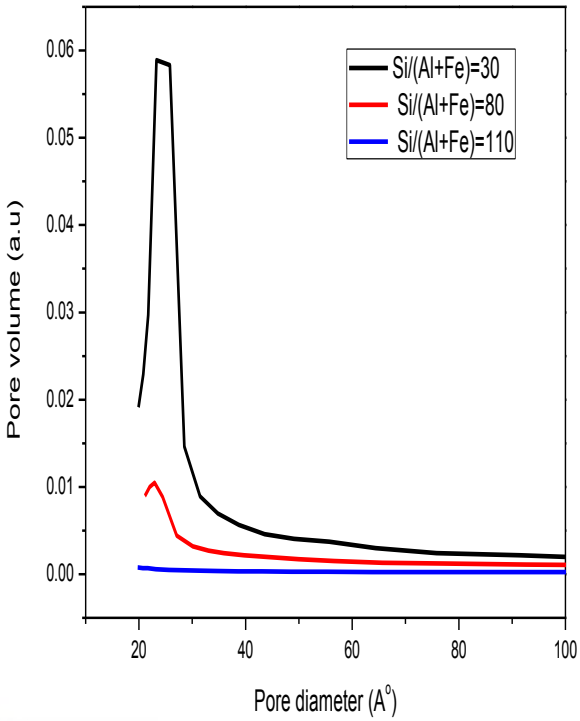

Figure 6. 12: BJH plot of MCM-41 catalysts with Si/(Al + Fe) ratios of (a) 30, (b) 80 and (c) 110.

X-ray diffraction patterns of powder material were recorded at a region of 1.0 to 10° shown in Figure 6.13. Synthesised and calcined samples of Fe/Al-MCM-41 form a reflection (100) at a lower angle than the one previously reported [115]. Catalyst with Si/ (Al + Fe) ratio of 30 has moved further down to an angle of 1.88° with 37.83 Å *d*-spacing. This is known to be the effects of high volume of metal deposited in the MCM-41 materials [113, 114]. Catalyst with Si/ (Al + Fe) ratio of 110 show reflection (100) peak at 2.2° angle with *d*-spacing of 49.8 Å while Si/ (Al + Fe) ratio of 80 has a reflection 100 at 2.4° angle and *d*-spacing 51.6 Å.

These values seems to be higher than the ones reported for Fe/Al-MCM-41 with (100) reflection *d*-spacing of 38Å [99]. Si/ (Al + Fe) ratio of 110 catalyst had higher intensity with the appearance of three more reflection (110), (200) and (210) which indicate a highly ordered hexagonal array of parallel silica tubes [113].

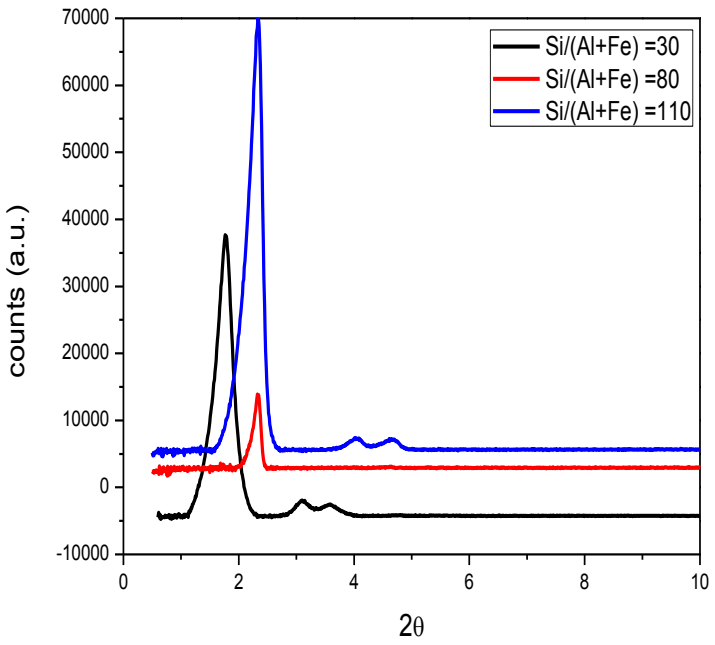

Figure 6. 13: XRD patterns of modified MCM-41 at a Si/ (Al + Fe) ratios of 30, 80, and 110.

Synthesised materials were characterised by FTIR before 1-hexene conversion to study the framework structure. This was done again after the conversion to study the changes and plotted in Figure 6.15 below. The FTIR bands at wavelength 490, 860, 1190 1510 cm^{-1}were obtained for the synthesised materials. Band at 490 cm^{-1} is associated with Si-O-Si bending while the rest are associated with Si-O-Si stretching. Adsorption bend for tetrahedral Fe-O bond is expected to appear at 595 to 630 cm^{-1} when modified with Fe_3O_4-B [115]. Bands at a wavenumber 960 cm^{-1} is associated with the lattice defect and presence of tetrahedral framework with M-O-Si Bridge. The band at 1545 cm^{-1} is associated with both Brönsted and Lewis acid sites while at 1445 cm^{-1} to Lewis acid sites [89].

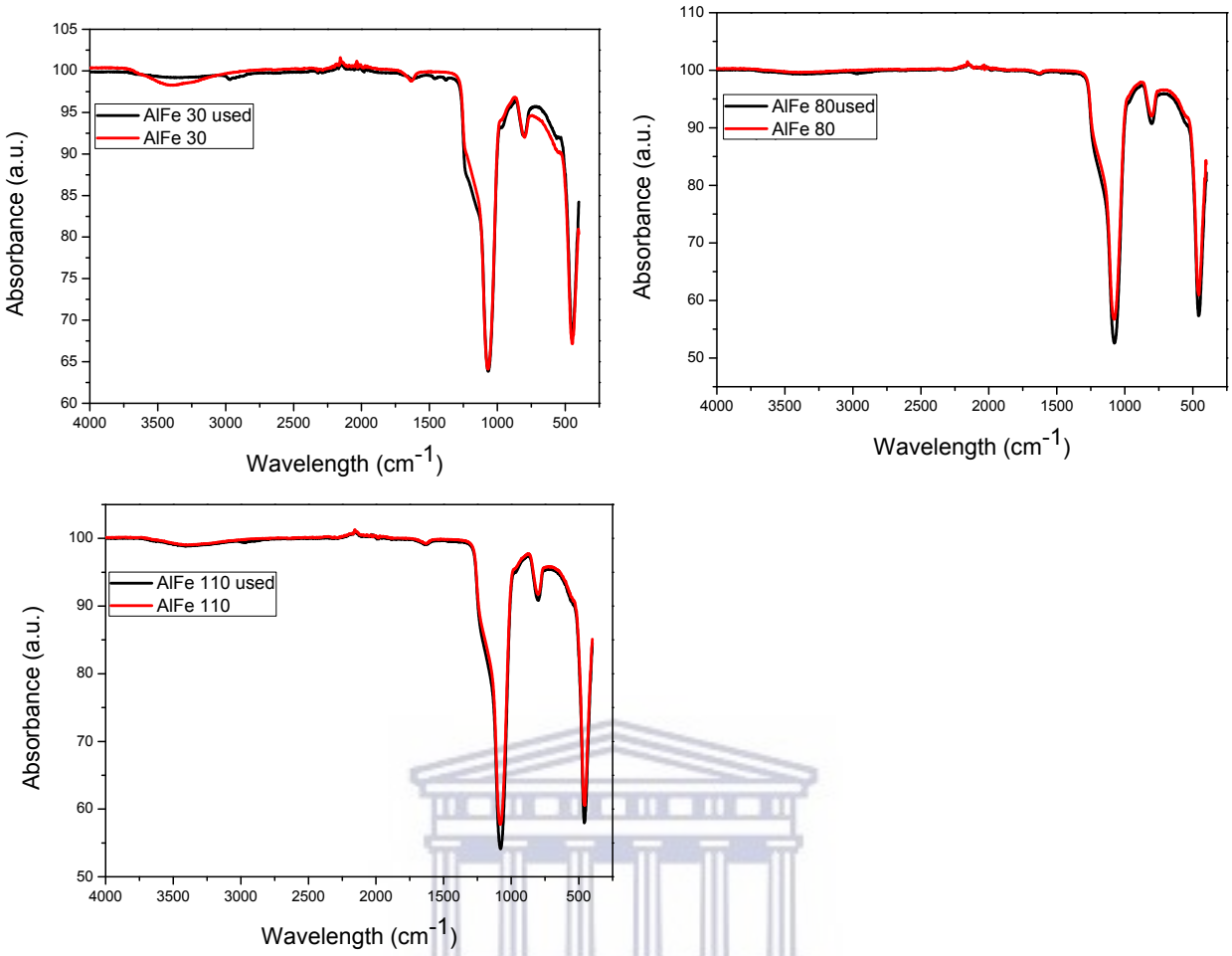

Figure 6. 14: FTIR spectra for MCM-41 catalysts with Si/ (Al + Fe) ratios of (a) 30, (b) 80 and (c) 110 before and after 1-hexene oligomerisation.

Morphology of the synthesised samples was investigated by Scanning electron microscopy and images are displayed in Figure 6.15. Image (a) and (c) showed a rod shape cluster together. Spherical shape molecules are observed in image (b) which was aggregated together to form a bigger molecule or attached to amorphous species. This behavior has been observed before for heteroatom incorporated mesoporous materials. Iron introduction affect the morphology of the MCM-41 and the spherical shape could be the grain salt on the MCM-41 surface [115].

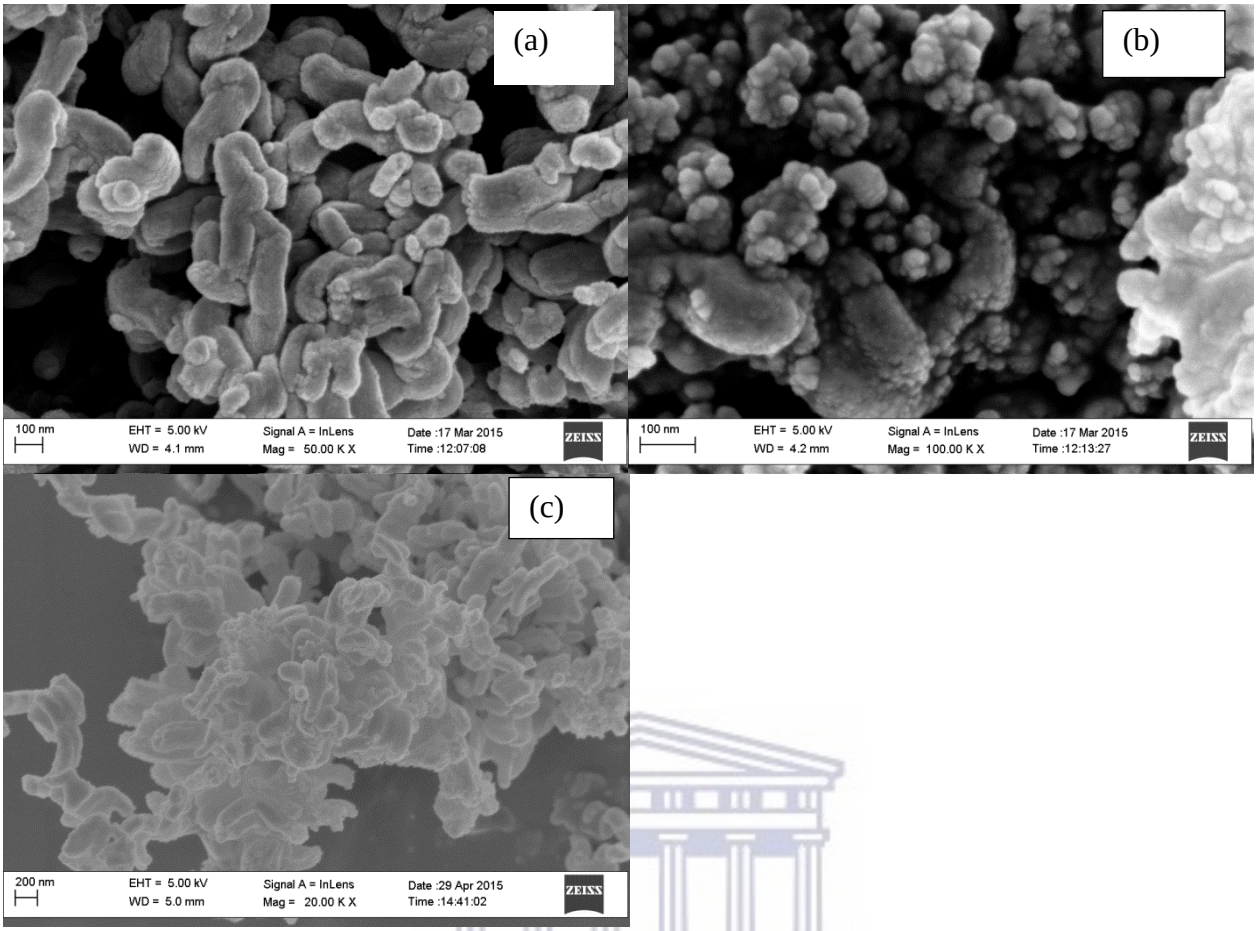

Figure 6. 15: SEM of iron-containing MCM-41 catalysts with Si/(Al + Fe) ratios of (a) 30, (b) 80 and (c) 110.

Chemical position of these materials were analysed by EDS and tabulated on Table 6.6 below. EDS showed the amount of the reagent precursors that forms part of the final material. The exact Si/Al ratio of the synthesised material were then calculated and displayed in the table.

Table 6. 6: Elemental compositions of synthesised samples were detected by energy-dispersive spectroscopy (EDS).

Sample code	Si atomic %	Al atomic %	Si/Al ratio	SiO_2/Al_2O_3 ratio
Si/(Al+Fe) = 30	5.79	0.13	45	90
Si/(Al+Fe) = 80	5.07	0.09	56	112
Si/(Al+Fe) =110	5.62	0.09	62	124

Ammonia-TPD was used to determine the acid sites in the synthesised materials after loading iron and aluminium to MCM-41. Desorption temperature and ammonium desorption amount are considered as indexes of acid strength and number of acid sites respectively. Synthesised materials show peaks at temperature range of 170 to 350 °C which is associated with Brönsted acid sites. At range of 530 to 695° a second peak was observed which is associated with the presence of Lewis acid sites. Acid sites for these materials were proportional to the amount of metal incorporated. In the synthesis of Cu/Al-MCM-41, the desorption temperature at 180 °C was associated with reduction of Cu^{2+} to Cu^{+} and that at 689 °C to reduction of Cu^{+} to Cu^{0}. This can also explain the desorption temperature due reduction of Cr in the synthesised material [90].

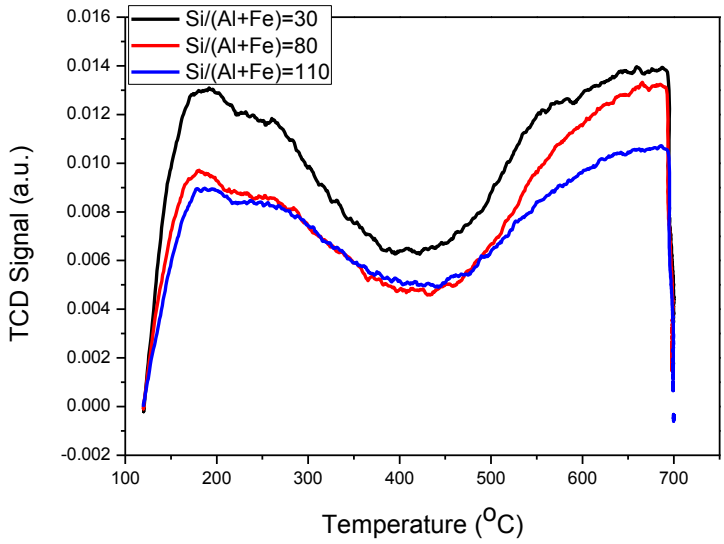

Figure 6. 16: Ammonia-TPD patterns of Fe/Al-MCM-41 at different ratios.

The total number of acid sites for each synthesised species is shown in table 6.7 below. These values are lower compared to 0.439 mmol/g of Fe/Al-MCM-41 catalysts of ratio 100 reported [71]. Desorption temperature also increases as the as the amount of metal added decreases. This implies that metal forms weaker bond to the framework structure than Si-O-Si bond.

Table 6. 7: Acidity of Fe/Al-MCM-41 samples measured by NH_3-TPD

Samples	Brönsted acid sites (200-400 °C)	Lewis acid sites (400-700 °C)	Total acidity (mmol/g)
Si/(Al + Fe) = 30	0.199 (172 °C)	0.171 (688 °C)	0.370
Si/(Al + Fe) = 80	0.149 (180 °C)	0.171 (686 °C)	0.320
Si/(Al + Fe) =110	0.134 (185 °C)	0.023 (690 °C)	0.157

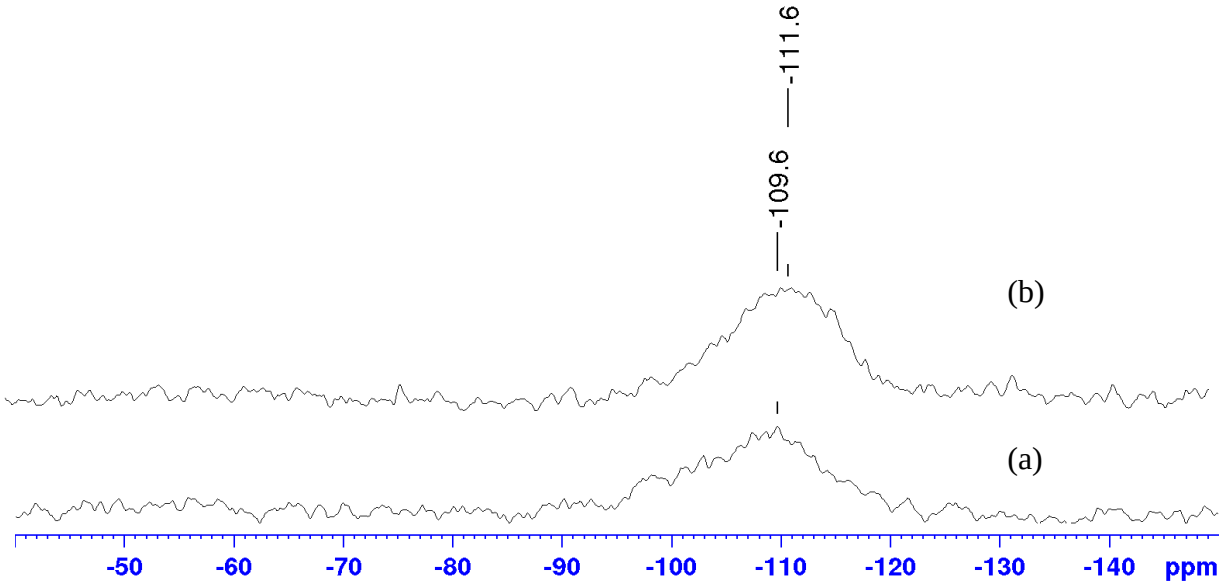

Figure 6. 17: ^{29}Si NMR spectra of Fe/Al-MCM-41 at Si/(Al + Fe) ratios (a) 30, (b) 80

Iron modified Al-MCM-41 show a broad resonance peak at -110 ppm for ratio 30 and -112 ppm for Si/ (Al + Fe) ratio of 180. The broadness of these peaks starts at -95 to -120 ppm. This peak is made up of different species such as silicon atoms of unbound silanols and bridged siloxane indicated by resonance peak at -100 and -110 ppm respectively [116]. Towards -111 ppm that resonance peak is assigned to silicon free of aluminium. Due to the irregularity on location arrangement of Si-O-Si bonds in the pore, this results in the broadening of the resonance peak [69].

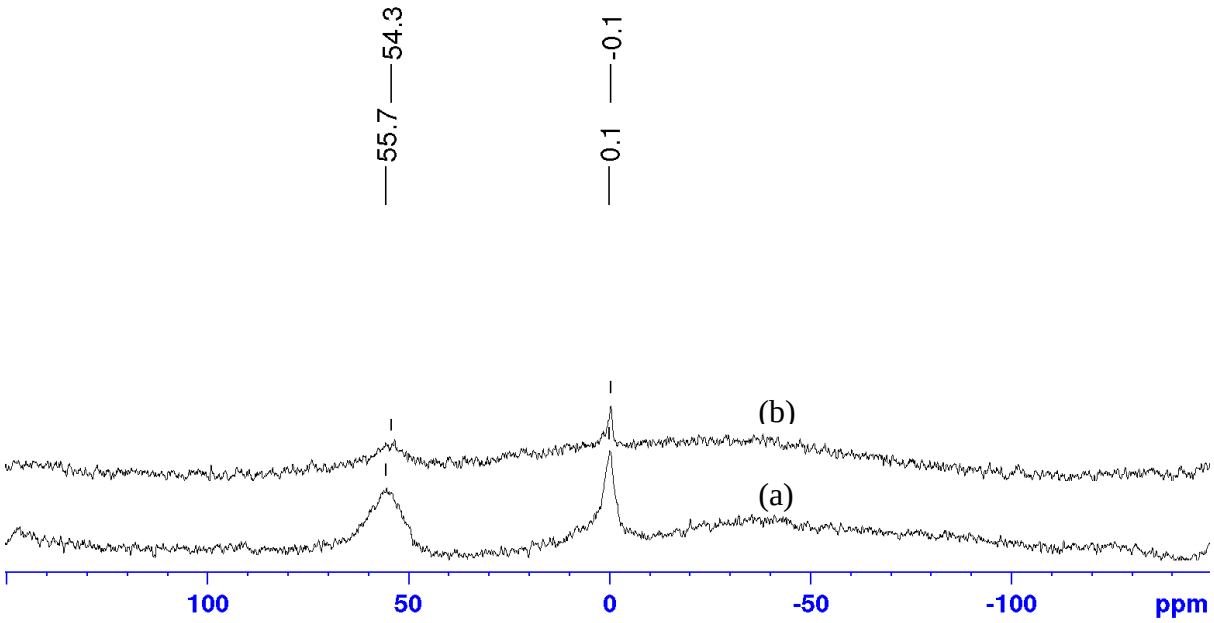

Figure 6. 18: ^{27}Al NMR spectra for Fe/Al-MCM-41 at Si/(Al + Fe) ratios (a) 30, (b) 80

Double introduction of aluminium and iron in MCM-41 framework was also analysed by ^{27}Al NMR spectroscopy after calcination. The spectra show a resonance peak at -56 ppm for ratio 30 and -54 ppm for Si/ (Al + Fe) ratio 80. This indicates the presence of tetrahedral co-ordinate aluminium. The peak at -0.1 ppm for both samples indicates the octahedral co-ordinate aluminium which seem to be dominant than the tetrahedral co-ordination. A higher content of these octahedral co-ordinations is due to removal of aluminium species from the framework during calcination.

The catalyst was packed in the fixed bed quartz reactor with 1-hexene passing at a rate of 0.980mL/min for catalytic testing as rests of synthesised material were. Samples were sampled hourly and analysed by GC. Conversion of the feed by these materials was reported as a function of time in Figure 6.20 below. The selectivity of the synthesised material in the conversion of 1-hexene to hydrocarbons is shown in Figure 6.21 below.

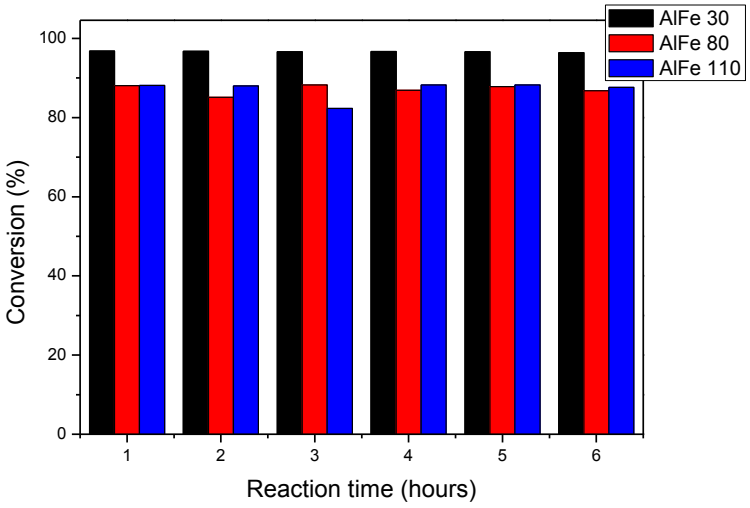

Figure 6. 19: Conversion of 1-hexene over Fe/Al-MCM-41 with different Si/(Al + Fe) ratio in a fixed bed quartz reactor at 350 °C.

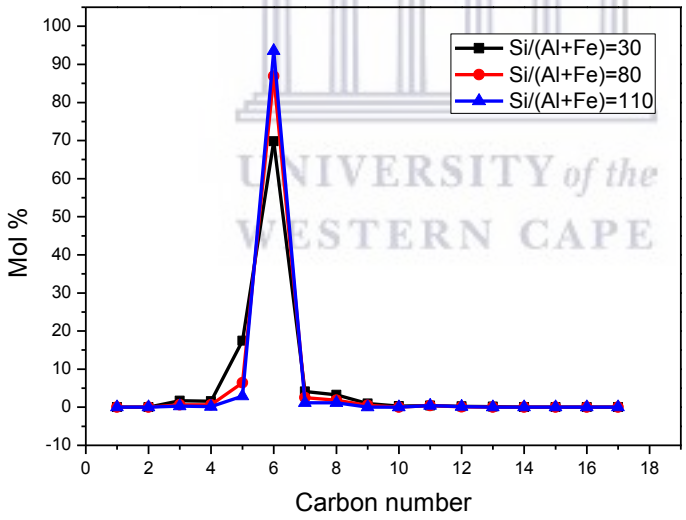

Figure 6. 20: Selectivity towards hydrocarbons of the Fe/Al-MCM-41 catalyst on liquid product with different Si/(Al + Fe) ratio in a fixed bed quartz reactor at 350 °C.

When the catalysts were tested in 1-hexene oligomerisation Al/Fe-MCM-41 with Si/ (Al + Fe) ratio of 30 showed higher conversions than Si (Al + Fe) ratio of 80 and 110. Figure 6.20 displays that Si/ (Al + Fe) ratio of 30 catalyst gave a range of 97% conversion while 80 and

110 had a range of 89%. It has been reported that increases with time till equilibrium conditions are reached, so increasing the catalyst loading increases conversion [110]. Therefore, the higher content of iron increased the catalyst activity. Upon testing of Fe/Al-MCM-41 catalyst for production of bio-fuel and chemicals in biomass pyrolysis it was discovered that the catalyst produces more coke due to dehydrogenation reaction which is favoured by the presence of iron [101]. This is seen in Figure 6.15 (a) as the new band appears at 3400 cm^{-1} wavelengths. Figure 6.21 shows that higher hydrocarbon cracking is observed with higher content of iron but again it's less selectivity towards C_6 hydrocarbons. These results show that these catalysts undergo other reactions than isomerisation. The use of Fe/Al-MCM-41 catalyst in production of bio-fuels from soybean oil showed selectivity to alkene and oxygenated compounds [117].

6. 3 Conclusion

It has been observed that metal loading results in the decrease of pore size as well as surface area, so double metal-doped MCM-41 showed the same effect. Due to atomic/ anionic radius of chromium, XRD patterns show the loss of MCM-41 framework structure while it was retained when iron was paired with aluminium. Morphology shows the extra chromium or aluminium species had positioned themselves f on the surface area while iron seems to disperse itself within the structural framework. The catalyst showed merely the same conversion of 1-hexene but selectivity increase for C_5 hydrocarbons compared to single doped catalyst. The catalysts are a good isomerisation reaction but with an increase in pressure formation of aromatic, paraffins and maybe naphtha can be obtained.

CHAPTER 7: General Conclusion

Synthesis parameters are the most important aspects for synthesising mesoporous silica MCM-41. Temperature, pH and reaction duration determines the pore size and the catalyst surface area. It has been observed that morphology of MCM-41 depends on the type of silica source used during synthesis of the catalysts. During this study tetraethylorthosilane, TEOS has shown a better morphology for the synthesis of MCM-41 than sodium silicate. Sodium silicate also affects the ratio of aluminium added to mesoporous MCM-41. It was observed that higher amounts of aluminium could not be deposited to the MCM-41 pores as much as the MCM-41 which was synthesised using TEOS as silica source. After carefully studying the MCM-41 synthesis parameter, the materials in this report were synthesised at 150˚C for the duration of 72 hours. Higher temperatures were employed to inhibit the crystallisation of the material.

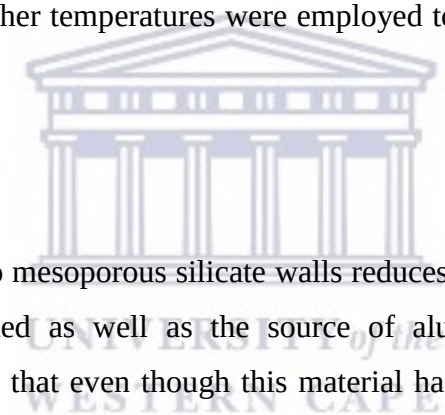

Deposition of aluminium into mesoporous silicate walls reduces the quality of pore structure, because of the amount added as well as the source of aluminium used and synthetic conditions. It has been noted that even though this material has highly ordered mesoporous structure their morphology is not well defined. Deposition of aluminium to mesoporous framework structure has increased the activity of the catalyst upon oligomerisation of 1-hexene when compared to the Si-MCM-41 mesoporous material. This supports the findings that aluminium increases the acid sites of the catalyst.

Hydrothermal incorporation of chromium and iron to mesoporous MCM-41 has been a successful synthesis. Incorporation of metals proved to reduce pore size as well as volume. Even though the analysis techniques used show that the material still resembles that of MCM-41, XRD pattern showed reduction of highly ordered mesoporous structure. The reduction of crystallinity was increased as the amount of metal incorporated increases. Higher amount of metal deposition showed higher conversion when tested for transformation of 1-hexene. This proved that the material synthesised has the properties of the catalyst.

Even though conversion above 80% were obtained for these materials, the catalysts were not suitable for the intended reaction. These catalysts were selective for C_6 hydrocarbons while the study was intended for the production of C_{10+} hydrocarbons that could be used in the production of diesel and other useful fuel. Therefore, it has been concluded that these catalysts are more active in isomerisation reaction.

Catalysts synthesis duration and steps taken are a major priority for the industries as the catalyst are synthesized in higher scales. Catalysis is considered as an art of work which determines the effective method for the synthesis and properties. The doping of metal to the mesoporous MCM-41 framework structure was also done by wet impregnation method. Materials showed the same effect as when the co-precipitation method was used. SEM morphology showed smooth surfaced spherical shape materials with no flakes on the surface, this emphasizes that the metal was dispersed within the framework structure.

Lower amounts of chromium metal had higher activity which suggested that higher amount lead to filled pore, therefore the active sites were not accessible to 1-hexene results in lower conversion. This was vice visa for iron which could be explained by their atomic radius. Due to the smaller size of iron, larger amounts of iron ions increase the activity of the catalyst. Selectivity for these materials remained the same as when the co-precipitation method was done except that conversion was reduced when the wet impregnation method was used for synthesis of metal doped MCM-41. Pores almost perish when Al/Cr were incorporated in mesoporous MCM-41. The crystallinity was extremely reduced such that reflections for highly ordered mesoporous structure were lost. The flakes on the surface area showed that metals were not dispersed within the framework structure of MCM-41. Different structural morphology was obtained for Si/ (Al + Fe) while highly ordered MCM-41 structure was maintained. SEM morphology showed that metals were well dispersed in the framework structure.

Higher conversion rates have been observed for these materials as about 90% conversion has been obtained. As it has been observed that pore size decreases due to metal incorporation, double metal loading also has the same effect. The reduction in pore size is also considered as a cause of cracking as the branched material cannot pass though the pores. The absence of carbon deposition peak after oligomerisation in FTIR suggests that transition-state selectivity was applied than product selectivity which would result in hydrocarbons within the pores. The conclusion was made that none of the synthesised catalyst were suitable for the oligomerisation of 1-hexene as cracking and isomerisation is a dominant reaction for these catalysts.

References

[1] Rossetto, E.; Nicola, B. P.; de Souza, R. F.; Bernardo-Gusmão, K.; Pergher, S. B. C., *Journal of Catalysis*, (2015) **323**, 45 - 54.

[2] Htay, M. M.; Oo, M. M.; World Academy of Science, Engineering and Technology, (2008) **48**, 114 - 120.

[3] Jihong, Y., State Key Laboratory of Inorganic Synthesis and Preparative Chemistry, Elservier B.V. : (2007), 41 - 102.

[4] Rabo, J. A.; Schoonover, M. W., *Applied Catalysis A: General*, (2001) **222**, 261 - 275.

[5] Weitkamp, J., *Solid State Ionics*, (2000) **131**, 175 - 188.

[6] Georgiev, D.; Bogdanov, B.; Angelova, K.; Markovska, I.; Hristov, Y., *International Science conference*, (2009), 1 - 5.

[7] McCusker, L. B.; Baerlocher, C., In *Elservier B.V.*, Elservier B.V.: (2007), 3, 13 - 37.

[8] Carvalho, K. T. G.; Urquieta-Gonzalez, E. A., *Catalysis Today*, (2015) **243**, 92 - 102.

[9] Basumatary, A. K.; Kumar, R. V.; Ghoshal, A. K.; Pugazhenthi, G., *Journal of Membrane Science*, (2015) **475**, 521 - 532.

[10] Martins, L.; Hölderich, W.; Hammer, P.; Cardoso, D., *Journal of Catalysis*, (2010) **271**, 220 - 227.

[11] Moliner, M.,Direct synthesis of functional zeolitic materials. *ISRN Materials Science*, (2012) **2012**, 1 - 24.

[12] Rodrigues, S.; Uma, S.; Martyanov, I. N.; Klabunde, K. J., *Journal of Catalysis*, (2005) **233**, 405 - 410.

[13] Mokhonoana, M. P., University of the Witwatersrand, Johannesburg (2006), 1- 365.

[14] Chen, L. Y.; Ping, Z.; Chuah, G. K.; Jaenicke, S.; Simon, S., *Microporous and Mesoporous Materials*, (1999), **27**, 231 - 242.

[15] Selvaraj, M.; Sinha, P. K.; Lee, K.; Ahn, I.; Pandurangan , A.; Lee, T. G., *Microporous and Mesoporous Materials*, (2005) **78**, 139 - 149.

[16] Laha, S. C., Kumar,R. , *Microporous and Mesoporous Materials* (2002) **53**, 163 - 177.

[17] Huang, Z.; Miao, H.; Li, J.; Wei, J.; Kawi, S.; Lai, M. W., *Separation and Purification Technology*, (2013) **118**, 170 - 178.

[18] Ciesla, U.; Schüth, F., *Microporous and Mesoporous Materials*, (1999) **27**, 131 - 149.

[19] Lobo, A. J. Modelling structure direction and morphology control in zeolite synthesis, University College London (2012).

[20] Boukoussa, B.; Zeghada, S.; Ababsa, G. B.; Hamacha, R.; Derdour, A.; Bengueddach, A.; Mongin, F., *Applied Catalysis A: General*, (2015) **489**, 131 - 139.

[21] Chen, L. F.; Noreña, L. E.; Wang, J. A.; Zhou, X. L.; Navarrete, J.; Hernández, I.; Montoya, A.; Romo, P. P.; Salas, P.; Pergher, S. C., *Catalysis Today*, (2008) **27**, 231 - 242.

[22] Dědeček, J.; Žilková, N.; Čejka, J., *Microporous and Mesoporous Materials*, (2001) **44–45**, 259 - 266.

[23] Atchudan, R.; Pandurangan, A., *Journal of Molecular Catalysis A: Chemical*, (2012) **355**, 75 - 84.

[24] Elías, V. R.; Sabre, E. V.; Winkler, E. L.; Andrini, L.; Requejo, F. G.; Casuscelli, S. G.; Eimer, G. A., *Journal of Solid State Chemistry*, (2014) **213**, 229 - 234.

[25] Jihong, Y., *State Key Labouratory of Inorganic Synthesis and Preparative Chemistry*, J. Cejka, H. v. B., A. Corma and F. Schuth Ed. Elservier B.V.: (2007).
[26] Donahoe, R. J.; Ltou, J. G., *Clays and Clay Minerals*, (1984) **32**, 433 - 443.
[27] Laha, S. C.; Kumar, R., *Microporous and Mesoporous Materials*, (2002) **53**, 163 - 177.
[28] Tshabalala, T. E., Aromatization of *n*-hexane over metal modified H-ZSM-5 zeolite catalysts, University of the Witwatersrand, Johannesburg (2009).
[29] Coma, A., *Chemical Reviews*, (1995) **95**, 414 - 559.
[30] Umemura, A.; Cubillas, P.; Anderson, M. W.; Agger, J. R., Modelling crystal growth in zeolite A, In *Studies in Surface Science and Catalysis*, Antoine Gédéon, P. M.; Florence, B. Eds.; Elsevier: (2008), **174 A**, 705 - 708.
[31] Cubillas, P.; Anderson, M. W., Zeolites and Catalysis, Synthesis, Reactions and Applications, In WILEY-VCH Verlag GmbH & Co. KGaA, Weinheim: (2010).
[32] Vetter, T.; Iggland, M.; Ochsenbein, D. R.; Hanseler, F. S.; Mazzotti, M., *Journal of the American Chemical Society*, (2013) **13**, 4890 − 4905.
[33] Cundy, S.; Cox, P. A., *Microporous and Mesoporous Materials*, (2005) **82**, 1 - 7.
[34] Csicsery, S. M., *Pure & Applied Chemistry*, (1986) **58**, 841- 856.
[35] Buchanan, J. S., *Catalysis Today*, (2000) **55**, 207 - 212.
[36] Coelho, A.; Caeiro, G.; Lemos, F.; Ribeiro, F. R., *Fuel*, (2013) **111**, 449 - 460.
[37] Oliveira, P.; Borges, P.; Pinto, R. R.; Lemos, M. A. N. D. A.; Lemos, F.; Védrine, J. C.; Ribeiro, F. R., *Applied Catalysis A: General*, (2010) **384**, 177 - 185.
[38] Subiranas, A. M., *Combining Fischer-Tropsch Sythesis (FTS) and hydrocarbon reaction in one reactor*, universitatsverlag karlsruhe, (2007) **2**, 170 - 280.
[39] Tirupati, R. K.; Basu, S., *Fuel Processing Technology*, (2007) **88**, 493 - 500.
[40] Bellussi, G.; Mizia, F.; Calemma, V.; Pollesel, P.; Millini, R., *Microporous and Mesoporous Materials*, (2012) **164**, 127 - 134.
[41] Van Grieken, R.; Escola, J. M.; Moreno, J.; Rodríguez, R., *Chemical Engineering Journal*, (2009) **155**, 442 - 450.
[42] Knottenbelt, C., *Catalysis Today*, (2002) **71**, 437 - 445.
[43] Perego, C.; Carati, A., *Zeolites: From Model Materials to Industrial Catalysts*, (2008), 357 - 389.
[44] Schwarzer, R., *Applied Catalysis A: General*, (2008) **340**, 119 - 124.
[45] Sekretaryova A.; Beni V.; Eriksson M.; Karyakin A.A.; Turner A.and Vagin M.; *Journal of Mexican Chemical Society.*, (2013) **57**, 47-72
[46] K.S. Hui, C. Y. H. C., *Journal of Hazardous Materials*, (2006) **B137**, 1135 - 1148.
[47] Lindlar, B.; Kogelbauer, A.; Prins, R., *Microporous and Mesoporous Materials*, (2000) **38**, 167 -176.
[48] Selvaraj, M.; Pandurangan, A.; Seshadri, K. S.; Sinha, P. K.; Lal, K. B., *Applied Catalysis A: General*, (2003) **242**, 347 - 364.
[49] Van Grieken R.; Escola J.M.; Rodrigues R.; *Applied Catalysis A: General 305*, (2006) **155**, 176 -188.
[50] Taralkar U.S.; Kalita P.; Kumar R.; Joshi P.N. Applied Catalysis A: General, (2009) **358**, 88 - 94.
[51] Eimer, G.; Pierella, L.; Monti, G.; Anunziata, O., *Catalysis Letters*, (2002) **78**, 65 - 75.
[52] Grün, M.; Unger, K. K.; Matsumoto, A.; Tsutsumi, K., *Microporous and Mesoporous Materials*, (1999) **27**, 207 - 216.
[53] Ko, A.; Hung, C.; Chen, C.; Ouyang, K., *Catalysis Letters*, (2001) **71**, 219 - 224.
[54] Liu, X. H. Sun, Y. Y., *Journal of Colloid and Interface Science*, (2008) **319**, 377 - 380.

[55] Abu-Zied, B. M.; Schwieger, W.; Asiri, A. M., *Microporous and Mesoporous Materials*, (2015) **218**, 153 - 159.
[56] Meléndez-Ortiz H. I., García-Cerda L. A., Castruita G., and Perera-Mercado Y. A.. , *Journal of Mexican Chemical Society*, (2013) **57(2)**, 73 - 79.
[57] Yang, G.; Deng, Y.; Wang, J., *Ceramics International*, (2014) **40**, 7401 - 7406.
[58] Matsumoto A., H. C., K. Tsutsumi , M. Gru¨n, K. Unger, *Microporous and Mesoporous Materials*, (1999) **32**, 55 - 62.
[59] Meléndez-Ortiz H.I; Garcia-Cerda L.A.; castruita G.; Yeraldin O.M.; Perera-Mercado Y.A., *Ceramics International* (2012) **38**, 6353 - 6358.
[60] Chaudhari, K.; Bal, R.; Chandwadkar, A. J.; Sivasanker, S., *Journal of Molecular Catalysis A: Chemical*, (2002) **177**, 247 - 253.
[61] Corma, A.; Fornes, V.; Navarro, M. T.; Perezpariente, J., *Journal of Catalysis*, (1994) **148**, 569 - 574.
[62] Yang, G.; Deng, Y.; Ding, H.; Lin, Z.; Shao, Y.; Wang, Y., *Applied Clay Science*, (2015) **111**, 61 - 66.
[63] Fu, P.; Yang, T.; Feng, J.; Yang, H., *Journal of Industrial and Engineering Chemistry*, (2015) **29**, 338 - .
[64] Nova, Q; Ziarani G.M.; Salavati-Niasari M., *Arabic Journal of chemistry*, (2006) **29**, 440-443.
[65] Zheng, L.; Wang, W.; Shi, Y., *Chemosphere*, (2010) **79**, 665 - 671.
[66] Gaydhankar T.R.; Samuel V.; Jha R.K.; Kumar R.; Josh P.N., (2007) **42**, 1473 - 1484.
[67] Gaydhankar, T. R., *Journal of Molecular Catalysis A: Chemical*, (2007) **265**, 306 - 315.
[68] Kang, F.; Wang, Q.; Xiang, S., *Materials Letters*, (2005) **59**, 1426 - 1429.
[69] Savidha, R.; Pandurangan, A., *Applied Catalysis A: General*, (2004) **276**, 39.
[70] Chen, X.; Huang, L.; Ding, G.; Li, Q., *Catalsis Letters*, (1997), 123 - 128.
[71] Araújo, R. S.; Costa, F. S.; Maia, D. A. S.; Sant'Ana, H. B.; Cavalcante Jr., C. L., *Brazilian Journal of Chemical Engineering*, (2007) **24**, 135 - 141.
[72] Jana, S. K.; Kugita, T.; Namba, S., *Applied Catalysis A: General*, (2004) **266**, 245 - 250.
[73] Mintova , S.; Cejka, J., Chevron Energy and Technology company, Richmond, Ca, USA, In Elsevier B.V.: (2007).
[74] Chen, H.; Wang, Y., *Ceramics International*, (2002) **28**, 541 - 547.
[75] Yang, H.; Deng, Y.; Du, C.; Jin, S., *Applied Clay Science*, (2010) **47**, 351 - 355.
[76] Wang, G.; Wang, Y.; Liu, Y.; Liu, Z.; Guo, Y.; Liu, G.; Yang, Z.; Xu, M.; Wang, L., *Applied Clay Science*, (2009) **44**, 185 - 188.
[77] Vaughan, J. S.; Oconnor, C. T.; Fletcher, J. C. Q., *Journal of Catalysis*, (1994) **147**, 441 - 454.
[78] Cesteros, Y.; Haller, G. L., *Microporous and Mesoporous Materials*, (2001) **43**, 171 - 179.
[79] Jing-Zhong, W.; He—Xuan, L., *Journal of Natural Gas Chemistry*, (1997) **6**, 3, 273 - 247.
[80] Matsumoto, A.; Chen, H.; Tsutsumi, K.; Grün, M.; Unger, K., *Microporous and Mesoporous Materials*, (1999) **32**, 55 - 62.
[81] Sakthivel, A.; Selvam, P., *Journal of Catalysis*, (2002) **211**, 134 - 143.
[82] Hui, K. S.; Chao, C. Y. H., *Journal of Hazardous Materials*, (2006) **137**, 1135 - 1148.
[83] Farook, A.; Kueh, C., *Applied Catalysis A: General*, (2015) **489**, 162 - 170.
[84] Wu, H.-Y.; Zhang, X.-L.; Yang, C.-Y.; Chen, X.; Zheng, X.-C., *Applied Surface Science*, (2013) **270**, 590 - 595.
[85] Jana, S. K.; Takahashi, H.; Nakamura, M.; Kaneko, M.; Nishida, R.; Shimizu, H.; Kugita, T.; Namba, S., *Applied Catalysis A: General*, (2003) **90**,3, 143 - 147.

[86] Samanta, S.; Mal, N. K.; Bhaumik, A., *Journal of Molecular Catalysis A: Chemical*, (2005) **236**, 7 - 11.
[87] Javadian, H.; Taghavi, M., *Applied Surface Science*, (2014) **289**, 487 - 494.
[88] Wang, Y., *Journal of Catalysis* (2003) **220**, 347 - 357.
[89] Udayakumar, S.; Ajaikumar, S.; Pandurangan, A., *Applied Catalysis A: General*, (2006) **307**, 245 - 256.
[90] Mahendiran C. Sangeetha P., Vijayan P., Basha S.J.S., Shanthi K., *Journal of Molecular Catalysis A: Chemical*, (2007) **275**, 84-90.
[91] Chen, W.; Li, X.; Pan, Z.; Bao, Y.; Ma, S.; Li, L., *Chemical Engineering Journal*, (2015) **281**, 397 - 403 .
[92] Elías, V. R.; Sabre, E. V.; Winkler, E. L.; Casuscelli, S. G.; Eimer, G. A., *Applied Catalysis A: General*, (2013) **467**, 363 - 370.
[93] Elías, V.; Sabre, E.; Sapag, K.; Casuscelli, S.; Eimer, G., *Applied Catalysis A: General*, (2012) **413–414**, 280 - 291.
[94] Nelmark, A. V.; Kheifez, L. I.; Fenelonov, V. B., *Industrial Engineering Chemical Product Research Development.*, (1981) **20**, 438 - 450.
[95] Munnik, P. E.; de Jongh, P. E.; de Jong, K. P., Recent developments in the synthesis of supported catalyst, C*hemical Reviews*, (2015) **115**, 6687 - 6718.
[96] Li, Q.; Brown, S. E.; Broadbelt, L. J.; Zheng, J.; Wu, N. Q., *Microporous and Mesoporous Materials* (2003) **59**, 105 - 111.
[97] Mahmoudi, J.; Lotfollahi, M. N.; Asl, A. H., *Journal of Industrial and Engineering Chemistry*, (2015) **24**, 113 - 120.
[98] Iliopoulou, E. F.; Antonakou, E. V.; Karakoulia, S. A.; Vasalos, I. A.; Lappas, A. A.; Triantafyllidis, K. S., *Chemical Engineering Journal*, (2007) **134**, 51 - 57.
[99] Antonakou, E.; Lappas, A.; Nilsen, M. H.; Bouzga, A.; Stöcker, M., *Fuel*, (2006) **85**, 2202 - 2212.
[100] Klaus, H., Theopold "Deprotonation of coordinated ethylene may start Phillips catalysis" Proceedings, In U.S. National Academy of Sciences, (2014) 111, 11578 - 11579.
[101] Zholobenko, V. L.; Holmes, S. M.; Cundy, C. S.; Dwyer, J., *Microporous Materials*, (1997) **11**, 83 - 86.
[102] Mahendiran, C.; Sangeetha, P.; Vijayan, P.; Sardhar Basha, S. J.; Shanthi, K., *Journal of Molecular Catalysis A: Chemical*, (2007) **275**, 84 - 90.
[103] Chao W., *Chemical Engineering Journal*, (2015) **281**, 397 - 403.
[104] Huang, R.; Lan, B.; Chen, Z.; Yan, H.; Zhang, Q.; Bing, j.; Li, L., *Chemical Engineering Journal*, (2012) **180**, 19 - 24.
[105] Anbia, M.; Neyzehdar, M.; Ghaffarinejad, A., *Sensors and Actuators B: Chemical*, (2014) **193**, 225 - 229.
[106] Li, B. W., K.; Yuan, T.; Han, C.; Xu, J.; Pang, X. , *Microporous and Mesoporous Materials*, (2012) **151**, 277 - 281.
[107] Yieng J., *Applied Catalysis A: General 305*, (2012) **305**, 172-179.
[108] Rodrigues, S.; Ranjit, K. T.; Uma, S.; Martyanov, I. N.; Klabunde, K. J., *Journal of Catalysis*, (2005) **230**, 158 - 165.
[109] Lezanska, M.; Szymanski, G. S.; Pietrzyk, P.; Sojka, Z.; Lercher, J. A., *The Journal of Physical Chemistry C*, (2007) **111**, 1830 - 1839.
[110] Chaliha, S.; Bhattacharyya, K. G., *Catalysis Today*, (2009) **141**, 225 - 233.
[111] Voegtlin, A. C.; Matijasic, A.; Patarin, J.; Sauerland, C.; Grillet, Y.; Huve, L., *Microporous Materials*, (1997) **10**, 137 - 147.

[112] Pham, A. L.; Lee, C.; Doyle, F. M.; Sedlak, D. L., *Environmental science & technology*, (2009) **43**, 8930 - 8935.
[113] Alves H.; Pastore H.O., *Microporous and Mesoporous Material*, 2001 **47**, 397-406
[114] Nilsen, M. H.; Antonakou, E.; Bouzga, A.; Lappas, A.; Mathisen, K.; Stöcker, M., *Microporous and Mesoporous Materials*, (2007) **105**, 189 - 208.
[115] Abdollahi-Alibeik, M.; Rezaeipoor-Anari, A., *Journal of Magnetism and Magnetic Materials*, (2016) **398**, 205 - 214.
[116] Li, X.; Yu, H.; He, Y.; Xue, X., *Journal of Analytical Methods in Chemistry*, (2012) **2012**, 1 - 5.
[117] Hammadi F. Y., Alghoul M.A., Asim N., *Journal of Analytical and Applied Pyrolysis*, (2013) **104**, 325 - 329.

Appendix A

DHA chromatogram for 1-hexene conversion over MCM-41 synthesised at 90˚C for 72 hours.

Physical Properties Report

Reid Vapor Pressure	5.9	psi at 100 °F
Liquid Density	0.6929	g/ml (15 °C)
Research Octane Number	124.3	
Motor Octane Number	115.2	
Gross Heating Value	43547.8	KJ / Kg
Nett Heating Value	40765.0	KJ / Kg
Bromine Number	211.2	

PIONA Report in Mass%

	Paraffins Cyclo	Paraffins Iso	Paraffins Normal	Olefins	Others	Total
	0,00	0,00	0,00	0,00	7,98	7,98
C3	0,00	0,00	0,00	0,07	0,00	0,07
C4	0,00	0,00	0,00	0,40	0,00	0,40
C5	0,02	0,00	0,00	3,32	0,08	3,42
C6	0,00	0,02	2,64	79,07	1,27	83,00
C7	0,00	4,63	0,04	0,20	0,00	4,87
C8	0,04	0,00	0,07	0,08	0,00	0,19
C9	0,00	0,04	0,00	0,00	0,00	0,04
C12	0,05	0,00	0,00	0,00	0,00	0,05
Total	**0,10**	**4,69**	**2,74**	**83,14**	**9,33**	**100,0**

PIONA Report in Volume%

	Paraffins Cyclo	Paraffins Iso	Paraffins Normal	Olefins	Others	Total
	0,00	0,00	0,00	0,00	6,91	6.91
C3	0,00	0,00	0,00	0,09	0,00	0.09
C4	0,00	0,00	0,00	0,45	0,00	0.45
C5	0,02	0,00	0,00	3,07	0,08	3.18
C6	0,00	0,02	2,75	80,10	1,26	84.14
C7	0,00	4,75	0,04	0,20	0,00	4.98
C8	0,03	0,00	0,07	0,08	0,00	0.18
C9	0,00	0,04	0,00	0,00	0,00	0.04
C12	0,04	0,00	0,00	0,00	0,00	0.04
Total	**0,09**	**4,80**	**2,86**	**84,00**	**8,25**	**100,0**

PIONA Report in Mol%

	Paraffins Cyclo	Paraffins Iso	Paraffins Normal	Olefins	Others	Total
C3	0,00	0,00	0,00	0,15	0,00	0,15
C4	0,00	0,00	0,00	0,64	0,00	0,64
C5	0,03	0,00	0,00	4,41	0,11	4,54
C6	0,00	0,02	2,79	85,80	1,41	90,02
C7	0,00	4,22	0,03	0,19	0,00	4,44
C8	0,03	0,00	0,05	0,07	0,00	0,15
C9	0,00	0,03	0,00	0,00	0,00	0,03
C12	0,03	0,00	0,00	0,00	0,00	0,03
Total	**0,08**	**4,26**	**2,88**	**91,26**	**1,52**	**100,00**

D 86 Boiling Point Distribution report

[ASTM D-86 (STP 577)] is invalid

Vol%	BP °C
IBP	45,4
5	57,7
10	61,7
20	67,0
30	68,4
50	66,8
70	63,1
80	60,5
90	61,6
FBP	84,3

True Boiling Point Distribution report

%Off	Mass% °C	Vol% °C	%Off	Mass% °C	Vol% °C	%Off	Mass% °C	Vol% °C	%Off	Mass% °C	Vol% °C
IBP	-6,2	-6,2	30	63,5	63,8	60	66,5	66,5	90	68,1	68,1
5	-2,6	-2,1	35	64,5	64,7	65	66,6	66,6	95	69,1	69,3
10	39,4	42,4	40	65,2	65,2	70	66,7	66,7	FBP	90,7	87,1
15	48,6	50,2	45	65,6	65,7	75	66,8	66,8			
20	55,6	56,6	50	66,1	66,1	80	66,9	66,9			
25	60,1	60,6	55	66,4	66,4	85	67,3	67,4			

Detailed Peak Report

#	Time	Index	Name	Grp	Area	Mass%	Vol%
1	7,455	279,4	propene	nO	3,964E+002	0,070	0,094
2	9,427	383,7	1-butene	nO	1,601E+003	0,284	0,328
3	10,258	407,5	t-2-butene	iO	3,637E+002	0,065	0,073
4	10,943	420,1	c-2-butene	iO	2,568E+002	0,046	0,050
5	16,182	488,2	ethylcyclopropane	cP	1,112E+002	0,020	0,020
6	16,898	495,2	2-methyl-1-butene	iO	7,294E+002	0,130	0,137

#	Time	Index	Name	Grp	Area	Mass%	Vol%
7	18,485	509,5	2-methyl-1,3-butadiene	dO	4,792E+002	0,083	0,083
8	18,960	513,5	t-2-pentene	iO	1,250E+003	0,222	0,236
9	19,497	517,9	c-2-pentene	iO	2,182E+002	0,039	0,041
10	19,983	521,8	2-methyl-2-butene	iO	1,991E+003	0,354	0,367
11	25,415	558,2	cyclopentene	cO	1,489E+004	2,570	2,291
12	26,988	567,1	2,3-dimethylbutane	iP	1,144E+002	0,021	0,022
13	27,105	567,7	c-4-methyl-2-pentene	iO	1,325E+004	2,356	2,422
14	27,590	570,3	c-1,5-hexadiene	dO	6,497E+003	1,126	1,120
15	27,897	571,9	t-4-methyl-2-pentene	iO	1,405E+002	0,025	0,026
16	28,163	573,3	2-methyl-1-pentene	iO	2,529E+004	4,496	4,551
17	30,428	584,5	t-1,5-hexadiene	dO	8,081E+002	0,140	0,139
18	31,330	588,7	C6 olefin	iO	4,083E+004	7,078	7,245
19	31,553	589,7	1-hexene	nO	9,096E+003	1,617	1,655
20	33,598	598,6	hexane	nP	1,449E+004	2,637	2,752
21	34,377	602,8	2,3-dimethyl-1-butene	iO	4,750E+004	8,446	8,570
22	34,870	605,9	t-3-hexene	iO	7,676E+004	13,648	13,865
23	35,367	608,9	c-3-hexene	iO	9,171E+004	16,305	16,497
24	35,697	610,9	t-2-hexene	iO	5,266E+004	9,363	9,505
25	36,515	615,8		Un	3,896E+004	7,918	6,858
26	37,828	623,3	c-2-hexene	iO	8,853E+004	15,740	15,766
27	39,737	633,8	2,4-dimethylpentane	iP	2,539E+004	4,604	4,716
28	47,570	671,6	2-methylhexane + C7-olefin	iP	1,606E+002	0,029	0,030
29	54,388	699,4	heptane	nP	2,062E+002	0,037	0,038
30	54,870	701,9	c-3-heptene	nO	2,520E+002	0,045	0,044
31	55,075	703,2	2-methyl-2-hexene	iO	4,641E+002	0,082	0,080
32	55,357	704,9		Un	2,867E+002	0,058	0,050
33	56,498	711,8	t-2-methyl-3-hexene	iO	4,177E+002	0,074	0,074
34	67,155	769,7	C8 Olefin	iO	2,390E+002	0,042	0,041
35	71,110	788,7	2,2,5-trimethylhexane	iP	2,078E+002	0,038	0,036
36	73,085	797,8	C8 Olefin	iO	2,273E+002	0,040	0,039
37	73,617	800,4	octane	nP	3,768E+002	0,068	0,067
38	74,198	805,2	c-1,4-dimethylcyclohexane	cP	2,111E+002	0,037	0,033
39	108,743	1149,6	t-1-m-2-(4methylpentyl)-cyclopentan	cP	2,595E+002	0,045	0,039
					5,576E+005	**100,00**	**100,00**

Appendix B

DHA chromatogram for1-hexene conversion over Cr/Al-MCM-41 ratio 80 at 1 bar, 250 ˚C and 0.1 ml/min, sampled in 21 hours after the reaction started.

PIONA Report in Mass%

	Paraffins Cyclo	Paraffins Iso	Paraffins Normal	Olefins	Aromatics	Others	Total
	0,00	0,00	0,00	0,00	0,00	13,01	13,01
C0	0,00	0,00	0,00	1,27	0,00	0,00	1,27
C4	0,00	0,62	0,00	0,11	0,00	13,81	14,54
C5	0,00	2,37	0,00	0,84	0,00	0,12	3,33
C6	0,00	1,09	2,94	21,88	0,00	8,59	34,50
C7	0,00	2,01	0,11	2,60	1,36	0,20	6,28
C8	0,67	0,79	0,35	0,92	0,10	0,00	2,82
C9	2,38	0,62	0,00	0,34	0,14	0,00	3,49
C10	0,00	1,96	0,00	0,00	2,61	0,00	4,57
C11	0,00	1,51	0,24	0,00	10,37	0,00	12,11
C12	0,22	1,43	0,10	0,00	1,64	0,00	3,38
C13	0,00	0,00	0,00	0,00	0,32	0,00	0,32
Heavy	0,00	0,00	0,00	0,38	0,00	0,00	0,38
Total	**3,27**	**12,40**	**3,73**	**28,33**	**16,55**	**35,73**	**100,0**

PIONA Report in Volume%

	Paraffins Cyclo	Paraffins Iso	Paraffins Normal	Olefins	Aromatics	Others	Total
	0,00	0,00	0,00	0,00	0,00	11,88	11.88
C0	0,00	0,00	0,00	0,93	0,00	0,00	0.93
C4	0,00	0,80	0,00	0,13	0,00	15,34	16.27
C5	0,00	2,78	0,00	0,89	0,00	0,12	3.79
C6	0,00	1,19	3,23	23,39	0,00	9,00	36.82
C7	0,00	2,15	0,12	2,70	1,14	0,18	6.29
C8	0,62	0,82	0,36	0,93	0,08	0,00	2.81
C9	2,18	0,63	0,00	0,34	0,12	0,00	3.27
C10	0,00	1,96	0,00	0,00	2,15	0,00	4.10
C11	0,00	1,48	0,23	0,00	8,67	0,00	10.38
C12	0,20	1,39	0,09	0,00	1,22	0,00	2.90
C13	0,00	0,00	0,00	0,00	0,31	0,00	0.31
Heavy	0,00	0,00	0,00	0,28	0,00	0,00	0.28
Total	**3,00**	**13,19**	**4,03**	**29,58**	**13,68**	**36,52**	**100,0**

PIONA Report in Mol%

	Paraffins Cyclo	Paraffins Iso	Paraffins Normal	Olefins	Aromatics	Others	Total
C0	0,00	0,00	0,00	48,30	0,00	0,00	48,30
C4	0,00	0,41	0,00	0,08	0,00	9,72	10,20
C5	0,00	1,25	0,00	0,46	0,00	0,07	1,78
C6	0,00	0,48	1,30	9,90	0,00	3,98	15,67
C7	0,00	0,76	0,04	1,01	0,56	0,08	2,46
C8	0,23	0,26	0,12	0,31	0,04	0,00	0,95
C9	0,72	0,18	0,00	0,10	0,05	0,00	1,05
C10	0,00	0,53	0,00	0,00	0,74	0,00	1,27
C11	0,00	0,37	0,06	0,00	2,66	0,00	3,09
C12	0,05	0,33	0,02	0,00	0,40	0,00	0,80
C13	0,00	0,00	0,00	0,00	0,07	0,00	0,07
Heavy	0,00	0,00	0,00	14,37	0,00	0,00	14,37
Total	**1,00**	**4,57**	**1,54**	**74,53**	**4,51**	**13,85**	**100,00**

D 86 Boiling Point Distribution report

[ASTM D-86 (STP 577)] is invalid

Vol%	BP °C
IBP	19,2
5	16,1
10	18,0
20	20,9
30	31,6
50	66,2
70	113,1
80	153,7
90	177,9
FBP	204,9

True Boiling Point Distribution report

%Off	Mass% °C	Vol% °C	%Off	Mass% °C	Vol% °C	%Off	Mass% °C	Vol% °C	%Off	Mass% °C	Vol% °C
IBP	-11,7	-11,7	30	16,6	14,9	60	66,9	66,7	90	188,5	188,5
5	-4,4	-4,3	35	49,8	48,1	65	68,5	67,0	95	201,7	196,8
10	-2,3	-1,9	40	58,2	58,0	70	91,1	70,3	FBP	216,3	216,3
15	-0,1	1,6	45	59,1	58,9	75	116,8	98,1			
20	4,3	4,9	50	65,5	63,7	80	156,7	147,0			
25	7,9	8,1	55	66,6	66,5	85	188,4	174,2			

Detailed Peak Report

#	Time	Index	Name	Grp	Area	Mass%	Vol%
1	8,673	353,3	isoButane	iP	1,301E+003	0,620	0,804
2	9,445	384,4	1-butene	nO	1,292E+002	0,059	0,072

#	Time	Index	Name	Grp	Area	Mass%	Vol%
3	10,265	407,7	t-2-butene	iO	1,106E+002	0,051	0,061
4	14,382	468,8	isoPentane	iP	5,019E+003	2,374	2,775
5	16,957	495,7	2-methyl-1-butene	iO	2,606E+002	0,120	0,133
6	18,515	509,8	2-methyl-1,3-butadiene	dO	2,613E+002	0,117	0,124
7	19,517	518,1	c-2-pentene	iO	1,129E+002	0,052	0,057
8	20,027	522,1	2-methyl-2-butene	iO	1,092E+003	0,502	0,548
9	25,805	560,5	cyclopentene	cO	3,647E+002	0,163	0,153
10	26,765	565,9	2,3-dimethylbutane	iP	2,317E+003	1,091	1,194
11	27,473	569,7	3,3-dimethyl-1-butene	iO	1,705E+002	0,078	0,087
12	27,698	570,9	1,2-butadiene	dO	3,115E+004	13,812	15,336
13	28,435	574,7	2-methyl-1-pentene	iO	9,960E+002	0,458	0,489
14	30,150	583,1	t-1,5-hexadiene	dO	1,915E+004	8,589	8,997
15	31,493	589,4	1-hexene	nO	1,186E+003	0,546	0,589
16	31,657	590,1	C6 olefin	iO	1,938E+003	0,870	0,938
17	33,712	599,1	hexane	nP	6,242E+003	2,939	3,233
18	34,343	602,6	2,3-dimethyl-1-butene	iO	1,100E+004	5,061	5,412
19	34,768	605,3	t-3-hexene	iO	2,030E+004	9,340	10,000
20	35,327	608,7	c-3-hexene	iO	4,535E+003	2,086	2,225
21	35,742	611,2	t-2-hexene	iO	2,678E+003	1,232	1,318
22	36,483	615,6		Un	9,366E+003	4,926	4,496
23	37,800	623,2	c-2-hexene	iO	4,809E+003	2,212	2,335
24	39,935	634,9	2,4-dimethylpentane	iP	9,388E+002	0,441	0,476
25	46,670	667,6	4-methyl-1-hexene	iO	1,742E+002	0,080	0,083
26	47,405	670,9	4-methyl-2-hexene	iO	2,794E+002	0,129	0,132
27	47,565	671,6	2-methylhexane + C7-olefin	iP	3,332E+003	1,564	1,673
28	48,108	674,0	2-methyl-1,5-hexadiene	dO	1,427E+002	0,064	0,065
29	49,272	678,9	C7-Olefin	iO	2,137E+003	0,983	1,023
30	51,760	689,1	C7 olefin	iO	2,303E+002	0,106	0,110
31	53,523	696,0	C7 Olefin	iO	3,209E+002	0,148	0,154
32	54,352	699,2	heptane	nP	2,365E+002	0,111	0,118
33	54,798	701,5	C7 Olefin	iO	4,146E+002	0,191	0,198
34	55,015	702,8	2-methyl-2-hexene	iO	8,279E+002	0,381	0,390
35	55,300	704,6		Un	5,042E+002	0,265	0,242
36	56,430	711,4	t-2-methyl-3-hexene	iO	8,444E+002	0,388	0,409
37	57,175	715,8	2,3-dimethyl-2-pentene	iO	4,190E+002	0,193	0,198
38	61,057	737,9	methylcyclohexadiene	dO	3,068E+002	0,135	0,118
39	61,390	739,7	ctc-1,2,4-trimethylcyclopentane	cP	2,245E+002	0,103	0,100
40	63,945	753,3	C8 Olefin	iO	3,252E+002	0,150	0,152
41	64,662	757,1	toluene	Ar	3,165E+003	1,364	1,139
42	67,133	769,6	C8 Olefin	iO	3,014E+002	0,139	0,141
43	67,752	772,6	C8 Olefin	iO	1,100E+003	0,506	0,513
44	68,072	774,2	4-methylheptane	iP	2,204E+002	0,103	0,104
45	68,842	777,9	C8 diolefin + C8 paraffin	iP	2,309E+002	0,108	0,111
46	69,048	778,9	3-methylheptane	iP	9,691E+002	0,454	0,467
47	71,088	788,6	2,2,5-trimethylhexane	iP	2,520E+002	0,118	0,120
48	72,177	793,7	C8 Olefin	iO	2,640E+002	0,121	0,123
49	73,055	797,7	t-1,3-dimethylcyclohexane	cP	4,860E+002	0,223	0,206
50	73,593	800,2	octane	nP	7,374E+002	0,345	0,356

#	Time	Index	Name	Grp	Area	Mass%	Vol%
51	74,565	808,3	C9 olefin	iO	4,153E+002	0,191	0,190
52	78,705	841,4	2,5-dimethylheptane	iP	3,125E+002	0,146	0,150
53	81,350	861,7	m-xylene	Ar	2,274E+002	0,099	0,083
54	81,682	864,2	2-methyloctane	iP	2,240E+002	0,105	0,106
55	82,470	870,1	C9 olefin	iO	3,177E+002	0,146	0,145
56	83,270	876,0	3-ethylheptane	iP	2,901E+002	0,136	0,135
57	85,837	894,5	C9 paraffin	iP	2,555E+002	0,119	0,121
58	86,990	904,0	2,4-dimethylhexane	iP	2,743E+002	0,128	0,134
59	88,378	918,2		Un	2,825E+002	0,149	0,136
60	88,603	920,5	2,2-dimethyloctane	iP	2,008E+002	0,094	0,094
61	88,835	922,9	2,4-dimethyloctane	iP	3,359E+002	0,157	0,157
62	89,353	928,1	sec-butylcyclopentane	cP	3,822E+002	0,175	0,163
63	90,292	937,6	3,6-dimethyloctane	iP	2,427E+002	0,113	0,113
64	91,302	947,6	3-methyl-5-ethylheptane	iP	3,366E+002	0,157	0,156
65	92,325	957,6	Naphthene	cP	7,483E+002	0,343	0,317
66	92,820	962,4	5-methylnonane	iP	3,639E+002	0,170	0,168
67	95,948	992,2	C10 paraffin	iP	2,856E+002	0,133	0,132
68	96,935	1001,9	sec-butylbenzene	Ar	3,042E+002	0,134	0,113
69	99,850	1036,5	3,3,5-trimethylheptane	iP	3,677E+002	0,172	0,167
70	100,252	1041,2	1-methyl-4-isopropylbenzene	Ar	5,036E+002	0,221	0,188
71	101,125	1051,3	1-methyl-4-n-propylbenzene	Ar	3,963E+002	0,174	0,147
72	101,570	1056,5	C10 Aromatic	Ar	5,849E+002	0,257	0,206
73	101,875	1060,0	1,2-diethylbenzene	Ar	2,946E+002	0,129	0,107
74	102,085	1062,4	5-methyldecane	iP	6,754E+002	0,314	0,308
75	102,280	1064,6	4-methyldecane	iP	7,014E+002	0,326	0,320
76	102,507	1067,2	1-methyl-2-n-propylbenzene	Ar	4,297E+002	0,189	0,157
77	102,772	1070,2	C11 iso-paraffin	iP	4,825E+002	0,225	0,220
78	103,128	1074,2	1,4-dimethyl-2-ethylbenzene	Ar	8,719E+002	0,383	0,317
79	103,313	1076,3	1,3-dimethyl-4-ethylbenzene	Ar	3,323E+002	0,146	0,121
80	103,437	1077,7		Un	2,937E+002	0,154	0,141
81	103,627	1079,9	C11 Paraffin	iP	4,689E+002	0,218	0,214
82	103,752	1081,3		Un	2,139E+002	0,113	0,103
83	104,225	1086,6		Un	2,722E+003	1,431	1,307
84	104,392	1088,5	C11 Paraffin	iP	9,080E+002	0,422	0,414
85	104,703	1091,9	C11	nO	2,017E+003	1,061	0,775
86	104,830	1093,3	2,6-dimethyloctane	iP	8,461E+002	0,395	0,396
87	105,075	1096,1	1-methyl-4-tert-butylbenzene	Ar	7,095E+002	0,313	0,265
88	105,358	1099,2	1-ethyl-2-isopropylbenzene	Ar	3,510E+003	1,548	1,310
89	105,503	1101,1	undecane	nP	5,099E+002	0,237	0,232
90	105,707	1104,2	C12-paraffin	iP	2,417E+003	1,096	1,063
91	105,868	1106,7	1,2,3,5-tetramethylbenzene	Ar	7,424E+002	0,326	0,266
92	106,098	1110,1	1,2,4,5-tetramethylbenzene	Ar	1,236E+003	0,543	0,445
93	106,267	1112,7	iso-propylcyclohexane	cP	1,079E+003	0,495	0,449
94	106,378	1114,4	2-methylbutylbenzene	Ar	4,574E+002	0,202	0,171
95	106,492	1116,1	C11 Aromatic	Ar	4,030E+002	0,195	0,165
96	106,675	1118,8	C12-paraffin	iP	3,112E+002	0,141	0,137
97	106,770	1120,3	C11 Aromatic	Ar	5,531E+002	0,244	0,206
98	106,922	1122,5	C11 Aromatic	Ar	1,033E+003	0,499	0,422

#	Time	Index	Name	Grp	Area	Mass%	Vol%
99	107,115	1125,4	n-propylcyclohexane	cP	3,735E+003	1,714	1,568
100	107,295	1128,1	tert-1-butyl-2-methylbenzene	Ar	2,379E+003	1,049	0,888
101	107,530	1131,6	1-ethyl-2-propylbenzene	Ar	3,371E+003	1,487	1,258
102	107,662	1133,6	1-ethyl-2-methylbenzene	Ar	3,270E+002	0,143	0,118
103	107,752	1134,9	C11 Aromatic	Ar	7,980E+002	0,352	0,298
104	107,990	1138,5	C11 Aromatic	Ar	2,117E+003	0,934	0,790
105	108,178	1141,3	C11 Aromatic	Ar	2,182E+003	0,962	0,814
106	108,342	1143,7	C11 Aromatic	Ar	1,191E+003	0,525	0,445
107	108,472	1145,6		Un	9,937E+002	0,523	0,477
108	108,780	1150,1		Un	3,545E+003	1,864	1,701
109	108,883	1151,7	t-1-m-2-(4methylpentyl)-cyclopentan	cP	4,828E+002	0,219	0,199
110	109,037	1153,9	n-pentylbenzene	Ar	3,560E+002	0,142	0,120
111	109,208	1156,4		Un	2,736E+002	0,144	0,131
112	109,340	1158,4	C12-paraffin	iP	4,213E+002	0,191	0,185
113	109,443	1159,9	C11 Aromatic	Ar	6,805E+002	0,300	0,254
114	109,647	1162,9	C11 Aromatic	Ar	1,437E+003	0,634	0,536
115	109,972	1167,6		Un	1,450E+003	0,762	0,696
116	110,268	1171,9	t-1-butyl-3,5-dimethylbenzene	Ar	8,402E+002	0,308	0,248
117	110,415	1174,0	2,3-dimethyloctane	iP	1,223E+003	0,570	0,572
118	110,612	1176,9	1,1-dimethylindan	Ar	4,855E+002	0,212	0,154
119	110,767	1179,1		Un	4,477E+002	0,235	0,215
120	110,947	1181,7	1,2-dimethylindan	Ar	4,162E+002	0,181	0,136
121	111,417	1188,5	1-ethylindan	Ar	3,661E+002	0,159	0,119
122	111,555	1190,5	2-ethylindan	Ar	9,971E+002	0,434	0,316
123	111,770	1193,6	C12	nO	3,950E+002	0,208	0,152
124	112,258	1200,8	dodecane	nP	2,075E+002	0,096	0,093
125	114,853	1251,3	1-methyl-4-pentylbenzene	Ar	3,994E+002	0,177	0,129
126	115,495	1263,6	C6 benzene	Ar	1,108E+003	0,491	0,358
127	115,640	1266,4	C6 benzene	Ar	4,724E+002	0,209	0,153
128	116,025	1273,8		Un	6,533E+002	0,344	0,314
129	116,165	1276,4	C6 benzene	Ar	8,045E+002	0,356	0,260
130	116,682	1286,2		Un	2,169E+003	1,141	1,041
131	116,908	1290,5	C13-unidentified	Ar	6,462E+002	0,323	0,309
132	118,975	1337,2	C6 benzene	Ar	2,234E+002	0,099	0,072
133	119,585	1351,5	methylindan	Ar	2,452E+002	0,106	0,079
134	128,317	1549,0	C16	nO	2,285E+002	0,120	0,088
135	130,392	1593,9		Un	2,380E+002	0,125	0,114
136	131,198	1611,2	C17	nO	4,894E+002	0,257	0,188
137	132,097	1630,3		Un	5,905E+002	0,311	0,283
138	132,950	1648,3		Un	5,675E+002	0,298	0,272
139	139,993	1792,5		Un	4,281E+002	0,225	0,206
					2,161E+005	**100,01**	**100,00**